Mechanisms of metal penetration in solid electrolytes

by

Joon Young Richard Park

B.E.(Hons), University of Auckland (2016)

Submitted to the Department of Materials Science and Engineering
in partial fulfillment of the requirements for the degree of

Doctor of Philisophy in Materials Science and Engineering

at the

MASSACHUSETTS INSTITUTE OF TECHNOLOGY

June 2021

Author .....
Department of Materials Science and Engineering
May 5, 2021

Certified by .....
Yet-Ming Chiang
Kyocera Professor of Ceramics
Thesis Supervisor

Certified by .....
W. Craig Carter
Professor of Materials Science
Thesis Supervisor

Accepted by .....
Frances M. Ross
Chair, Departmental Committee on Graduate Studies

Mechanisms of metal penetration in solid electrolytes

by

Joon Young Richard Park

Submitted to the Department of Materials Science and Engineering
on May 5, 2021, in partial fulfillment of the
requirements for the degree of
Doctor of Philisophy in Materials Science and Engineering

Abstract

An important unresolved topic in materials science is the mechanism by which metals infiltrate solid electrolytes during electrodeposition. A deep understanding of this phenomenon in Li^+-conducting solid electrolytes could determine whether these materials can enable fast-charging (> 3 mA cm^{-2}) solid state batteries that are safer and more energy-dense than the state of the art. At present, it is thought that intensified stresses are generated at the largest surface flaws on the electrolyte during electrodeposition, and at the critical current density these stresses drive brittle fracture within the bulk to create paths for metal advancement.

This thesis demonstrates that metal penetration depends on two additional factors. The first is whether electric field focusing is present between the stripping and plating electrodes. We show that amplified electric fields, which correlate with increased local current densities, cause Li filled cracks to initiate and grow to penetration, overriding the presence of larger surface defects elsewhere. The second factor is the yield stress of the electrodeposited metal. We show that in Li^+-, Na^+-, and K^+-conducting solid state systems, the critical current density scales inversely with the mechanical deformation resistance of the electrodeposited metal.

We then present two novel electrode architectures in which a liquid phase enables higher critical current densities via interfacial stress relief and current homogenization. First, biphasic (liquid-solid) Na-K alloys are shown to exhibit K^+ critical current densities over 15 mA cm^{-2}, in contrast to 2.5 mA cm^{-2} for pure K metal. Second, an interfacial film of Na-K liquid between Li metal and $Li_{6.75}La_3Zr_{1.75}Ta_{0.25}O_{12}$ solid electrolyte doubles the critical current density compared to cells without the Na-K interlayer. These design approaches hold promise for overcoming mechanical stability issues that have heretofore limited the performance of solid state batteries.

Thesis Supervisor: Yet-Ming Chiang
Title: Kyocera Professor of Ceramics

Thesis Supervisor: W. Craig Carter
Title: Professor of Materials Science

Acknowledgments

I express my deepest gratitude to my thesis advisors, Professor Yet-Ming Chiang and Professor W. Craig Carter. I am especially indebted to Professor Chiang for accepting me as his student before I had any experience in electrochemistry. I have learnt an immeasurable amount during my 5 years at MIT, and this has only been possible because of the environment both of you have provided for me.

I am thankful to my thesis committee, Professor Ju Li and Professor C. Cem Tasan for their thoughtful feedback and advice on my work. I am also grateful to Professor Brian Sheldon, Professor Venkat Viswanathan, and Professor Matt Pharr for their invaluable contributions to this thesis.

I thank my colleagues in the Chiang-Carter group for creating a wonderful place to work. I acknowledge Frank Fan, Tushar Swamy, Menghsuan Sam Pan, Andres Badel, Yiliang Li, Charles Wan, Kevin Tenny, Sonia Zhang, Kai Xiang, David Young, Karen Sugano, Sunil Mair, Cole Fincher, Chris Eschler, Kevin Santillan, Omar Laris, Isaac Metcalf, Michael Wang, Liang Su, Daniel Rettenwander, Ariel Jackson, Jesse Benck, Seoung-Bum Son, Lisheng Gao, Leah Ellis, Ping-Chun Tsai, and Bohua Wen.

I am grateful for the people I am lucky to call my closest friends. Thank you to Ben Cameron, Ray Liao and Leilani Gilpin for being nothing short of family. Thank you to compatriot Kiwis Francis Hwang, Nicole Logan, Michael Kapteyn, Sam Gilmour, Jeffrey Mei and Richard Zhang for the irreverent banter and reminding me of home. Thank you to fellow materials scientists Brian Traynor and Eddie Pang for being perfect housemates over 4 years. Thank you to Alex Mijailovic for our jam sessions. Thank you to KellyAnn Tsai, Beth Pearce, Benedikt Markus, Colm O'Rourke and others from the MIT Rowing Club for helping me wake up early. Last but not least, thank you to Kerrin Steensen for the many special memories we shared together.

Finally, I would like to thank my family. You have all provided me with unconditional love and support throughout my whole life. My highest acknowledgement is for my mother, Jiyoun Kwon. From you I have learnt the value of ambition and hard work, and everything I have achieved is in part because of you.

THIS PAGE INTENTIONALLY LEFT BLANK

Contents

THIS PAGE INTENTIONALLY LEFT BLANK

List of Figures

List of Tables

Chapter 1

Introduction

Rechargeable batteries have enabled multiple advances in portable electronics, transportation, and renewable energy storage over the past two decades. For example, today's electric vehicle (EV) grade lithium-ion batteries possess an industry leading combination of high specific energy (~150 Wh kg^{-1} at pack-level) and a high energy density (~250 Wh L^{-1} at pack–level) [18], with a cycle life that is on track to reach 5,000 cycles [19]. However, to meet future energy and cost targets that require at least double the energy density, radical improvements are necessary [20]. This thesis outlines work that contributes to the development of all-solid-state batteries incorporating lithium metal, which may result in safer, more energy-dense batteries.

1.1 Overview of lithium battery development

Batteries store energy by separating two electronically conducting electrodes with an electronically insulating electrolyte to create an open circuit [21]. The electrolyte may be liquid, polymer, or inorganic solid. At the negative electrode, electrons are held at a high chemical potential, while the opposite is true in the positive electrode. Once a load connects the electrodes to close the circuit, electrons are free to flow from one electrode to the other, generating current. An external bias can subsequently be applied to reverse this process and charge the battery [22].

In a typical Li-ion battery, the negative electrode is Li^+ intercalated graphite and

the positive electrode is partially delithiated lithium cobalt oxide ($LiCoO_2$, LCO). During discharge, a redox reaction occurs at each electrode, transporting the electron, while the Li^+ ions move through a liquid electrolyte in the same direction [21]. This preserves charge neutrality. Although lithium is an ideal working ion due to its small size and high diffusivity which enables high power batteries, the graphite at the negative electrode is as an effective "dead weight" that limits the specific energy.

An obvious solution is to replace the graphite with metallic lithium. Lithium is both the most electro-positive (-3.04 V w.r.t the standard hydrogen electrode), and lightest metal (density of 0.534 g cm^{-3}), resulting in an exceptionally high capacity (3869 mAh g^{-1}, 2066 Ah L^{-1} theoretical capacities). This makes metallic lithium an ideal anode material [1].

Although using lithium metal anodes with conventional liquid electrolytes would also achieve greater energy densities, there are several fundamental problems in doing so. These include the formation of an unstable solid-electrolyte interphase (SEI) between the anode and liquid electrolyte which depletes the electrolyte during cycling, which leads to poor cycling performance, and a susceptibility to short circuits due to dendrite formation at practical current densities (1-3 mA cm^{-2}) [23–25]. These short circuits represent a significant safety risk as they may cause the liquid electrolyte, usually composed of a lithium salt ($LiPF_6$) dissolved in flammable organic solvents, to ignite spontaneously [24].

An alternative approach to enabling lithium metal anodes is to pair them with inflammable inorganic solid state electrolytes (SSEs), which could potentially result in safer, more energy-dense batteries (~250 Wh kg^{-1} and ~750 Wh L^{-1}, pack-level) compared to state-of-the-art lithium ion batteries (~150 Wh kg^{-1} and ~250 Wh L^{-1}, pack-level) [1, 26–30]. Solid state electrolytes are crystals in which ion transport occurs via solid state diffusion [31]. The ease of ion transport through electrochemical systems incorporating solid electrolytes thus depend on the energy landscape of the crystal and the ease of ion transport accross grain boundaries or macroscopic electrode-electrolyte interfaces [30]. At such electrode-electrolyte interfaces, a passivating electron insulating, but ionically conducting layer may be present.

Solid state electrolytes such as Li sulfides (for example, Li_3PS_4 (LPS), $Li_{10}GeP_2S_{12}$ (LGPS)) and garnet-structure oxides (for example, $Li_7La_3Zr_2O_{12}$ (LLZO)) have received much attention due to their high ionic conductivity and progress towards achieving an electrochemically stable electrode-electrolyte interface [27]. In particular, the garnet-structure oxide materials have been reported to possess either higher electrochemical stability windows compared to liquid electrolytes [27, 30, 32, 33]. A schematic comparing a typical Li-ion battery with a Li-metal battery is shown in Figure 1-1.

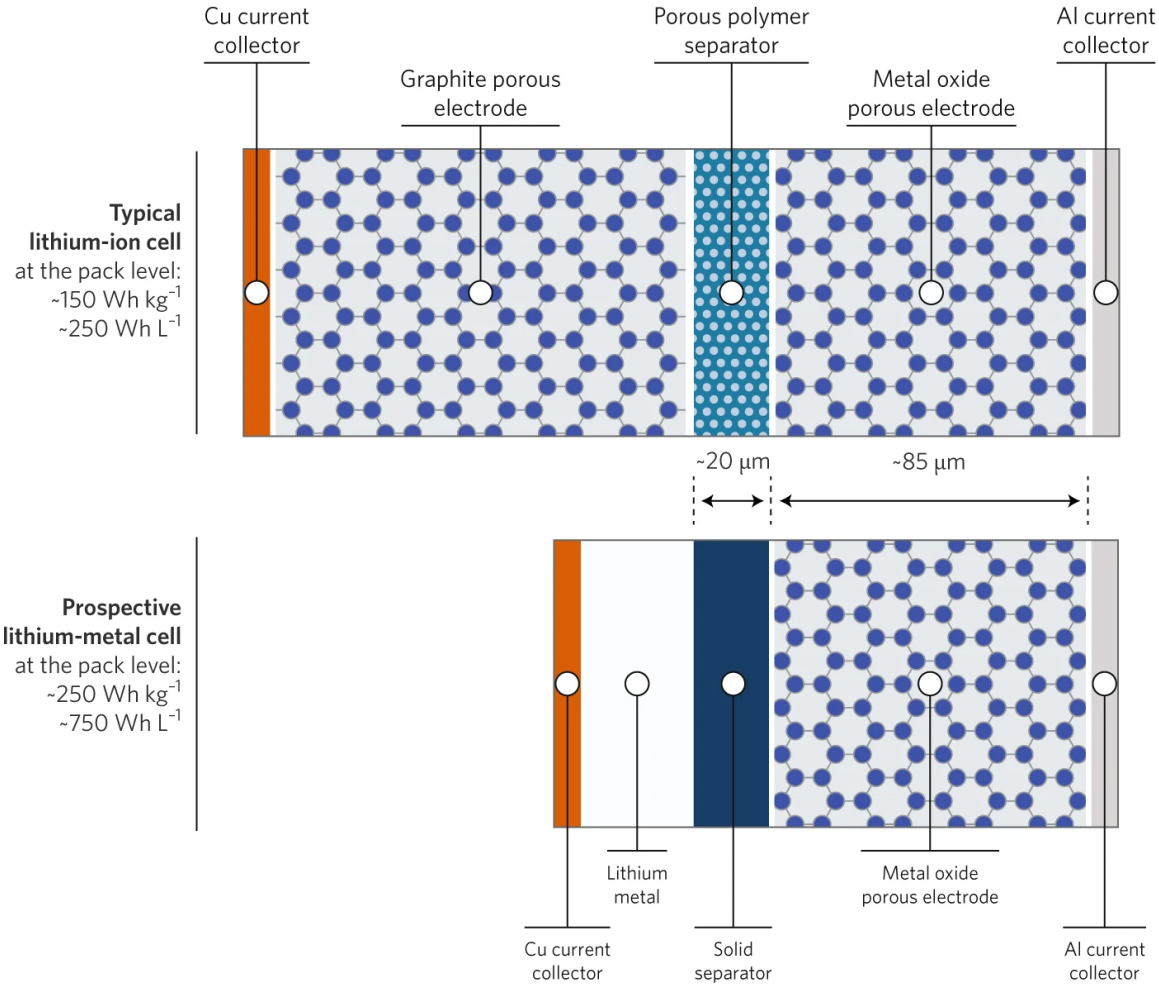

Figure 1-1: Schematic of a lithium battery with a graphite and metallic anode. From ref. [1]

Inorganic solid electrolytes further possess high shear moduli (~20 GPa for sulfides [34] and 100 –200 GPa for oxides [6]) far beyond twice that of Li metal (~5 GPa),

which has been identified as one criterion necessary for suppression of lithium metal dendrites via an interfacial stability analysis [35]. Nonetheless, a hallmark of both single crystalline and polycrystalline Li solid electrolytes is penetration by metal filaments on deposition at a critical current density (CCD) in the range 0.1–1 mA cm^{-2} (at room temperature), too low for most practical applications [3, 11, 12, 36–38].

Porz et al. performed experiments which suggested that Li metal electrodeposition induces brittle fracture of the electrolyte, in contrast to the interfacial perturbation model put forth by Monroe and Newman [3, 35]. In particular, it is proposed that the electrodeposition of Li metal onto pre-existing surface flaws on the solid electrolyte leads to stress intensification and subsequent fracture in a manner analogous to Griffith's classical theory [39]. Shorting behavior did not depend on the electrolyte's shear modulus, suggesting that the shear moduli criterion suggested by Monroe and Newman may not apply for ceramic electrolytes.

It is therefore evident that the exact mechanism of metal penetration in inorganic solid electrolytes during metal electrodeposition is not yet well understood. This thesis thus aims to expand our quantitative and predictive understanding of this general process and present a revised set of criteria for solid electrolyte failure.

1.2 Classical theory of brittle fracture

1.2.1 Stress intensification at surface flaws

The governing equation in elasticity theory is the biharmonic equation for the Airy stress function [40]:

$$\nabla^2 \left(\nabla^2 \phi \right) = \nabla^4 \phi \tag{1.1}$$

Where ϕ is the Airy stress function and ∇^2 is the Laplacian. The Airy stress function relates to 2-D stress fields in rectangular co-ordinates according to the following relations:

$$\sigma_{xx} = \frac{\partial \phi}{\partial y} \tag{1.2}$$

$$\sigma_{yy} = \frac{\partial \phi}{\partial x} \tag{1.3}$$

$$\sigma_{xy} = \frac{\partial^2 \phi}{\partial x \, \partial y} \tag{1.4}$$

Where σ denotes the stress, and x and y denote the rectagular co-ordinates in 2-D. Kirsch solved this equation for stress fields around a 2-D circular hole in a plane under uniaxial tension, and found that the stress around the hole was 3 times the applied stress, but decreased to the far field value within a hole diameter [41]. This localized stress intensification at the "defect" is a consequence of the elastic equations. Inglis subsequently derived the stress fields for an elliptical hole under uniaxial tension in 1913, and showed that the maximum stress at an elliptical hole is described by [42]:

$$\sigma_{max} = \sigma_{\infty} \left(1 + 2\sqrt{\frac{a}{r}} \right) \tag{1.5}$$

Where σ_{max} is the maximum stress in the elliptical hole, σ_{∞} is the far-field stress, a is the distance to the tip from the ellipse center, and r is the local radius of curvature at the tip. This stress field is displayed using force lines in Figure 1-2.

As the radius of curvature at the tip goes to zero (equivalent to a crack tip), the maximum local stress is infinite for any remote load. Although unphysical, the solution is correct for a linear elastic problem in which the material has no limiting yield/failure stress. This is a key result in fracture mechanics.

1.2.2 Driving force for crack propagation

In 1920, Griffith compared the work required to break atomic bonds to the strain energy released as a crack grows [39]. The key result is that the product of the critical tensile stress, and the square root of the flaw size, is a constant defined by two materials properties - the elastic modulus and surface energy:

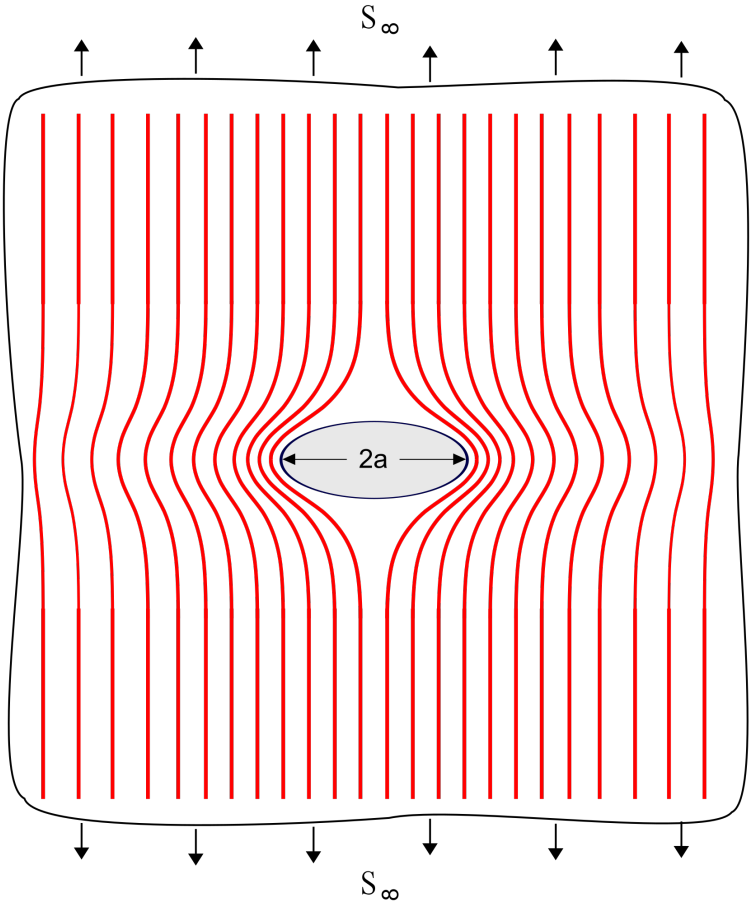

Figure 1-2: Force line representation of stress fields surrounding an elliptical hole under uniaxial tension. From ref. [2]

$$\sigma_c\sqrt{\pi a} = \sqrt{2\gamma_s E} \equiv K_c \tag{1.6}$$

Where σ_c is the critical remote stress required to propagate a crack of length a, γ_s is the surface energy, E is the elastic modulus, and K_c is the *critical stress intensity factor*. In 1939, Westergaard solved for the stress function around a direct crack under equi-biaxial tension, instead of an ellipse under uniaxial tension, to obtain the following stress function [43]:

$$\phi = \frac{\sigma_\infty}{1 - \left(\frac{a}{r}\right)^2} \tag{1.7}$$

With the symbols defined as per Equation 1.5. In 1957, Irwin approximated the Westergaard solution within the region close to the crack tip, and showed that the stresses at the crack tip can be expressed as a separable function [44]:

$$\sigma_{ij} = \frac{K}{\sqrt{2\pi r}} F_{ij}\left(\theta\right) \tag{1.8}$$

where:

$$K = \sigma_\infty\sqrt{\pi a} \tag{1.9}$$

The indices i,j represent the surface and direction of interest, θ is the angle from the crack tip, F is a geometric function of θ of order unity, a is the crack length, and r is the distance from the crack tip.

This shows that the severity of the stress state at the crack tip is proportional to K, analogous to K_c derived by Griffith. He defined this term the stress intensity factor. This parameter measures the driving force for crack propagation, and establishes a criterion for fracture —when K *reaches its critical value,* K_c [44].

K reduces to the form above only for a specific loading geometry. In general, K can be evaluated for an arbitrary geometry by knowing the stress and strain fields adjacent to the crack. It can be shown that K is directly related to a contour integral that involves the stress and strain tensors (the J-integral) [44].

1.3 Review of prior work

1.3.1 Poiseulle model of metal penetration

The first rigorous studies of short circuits induced by metal electrodeposition on ceramic electrolytes occurred during the development of Na–β"–alumina polycrystalline electrolytes for Na-S batteries. [45] These batteries utilised molten Na and S as the electroactive material, and operated at elevated temperatures on the order of 300°C [46]. It was observed that when these cells are charged (Na is electrodeposited onto the β"–alumina) at a rate above a "critical current density" via Na deposition, the batteries short circuit and fail irreversibly [47]. This failure was often traced back to electrolyte fracture, accompanied by observations of sodium metal plating into cracks within the alumina bulk.

Several models have been proposed to explain this behavior in a manner consistent with experimental observations. The key observations of interest are that that β"–alumina electrolytes do not degrade at operating conditions without the passage of current, deterioration occurs only during Na electrodeposition (cell charging), and that the "critical current density" decreases with decreasing temperature [45, 48, 49]. A unifying feature of the proposed models is the concept of ion flux focusing at the crack tip where Na primarily electroplates due to a lower local potential, and the resultant development of a Poiseulle pressure that drives molten Na flow through the crack [50]. The general form of a Poiseulle pressure is given by:

$$\Delta P = \frac{8\eta L Q}{\pi R^4} \tag{1.10}$$

Where ΔP is the pressure difference required to drive the flow, L is the pipe length, η is the fluid viscosity, Q is the flowrate, and R is the pipe radius, or in this context, a "crack width".

The simplest, and most widely accepted model consistent with experiment was proposed by Armstrong [45]. The Armstrong model argues that a sufficiently high Poiseulle pressure drives crack growth of surface cracks on the alumina [45] Indeed,

Armstrong showed that membrane longevity during electrolysis improves as surface flaws are removed.

This naturally leads to the concept of a "critical current density" related to a "critical Poiseulle pressure" that is reached when the inlet sodium flux at the crack tip becomes sufficiently high, provided that the crack geometry and Na viscosity remain constant. A further corollary of this model is that that critical current densities decrease at lower temperatures as the viscosity of Na would increase. [48, 51].

1.3.2 Metal penetration in Li^+ solid electrolytes

Short circuiting studies on Li^+-conducting solids have focused primarily on the polycrystalline oxide garnet $Li_7La_3Zr_2O_{12}$ (LLZO) [12, 13]. LLZO is a suitable model system due to its relative stability against air and Li, and a high conductivity (0.1-1 mS cm^{-1}) achieved via Al, Nb, Ti, or Ta doping to form Li vacancies and stabilize the cubic phase [30, 52]. Few studies have examined sulfides such as polycrystalline β- Li_3PS_4 or amorphous Li_3PS_4 due to its severe moisture sensitivity and resultant difficulty in handling [3].

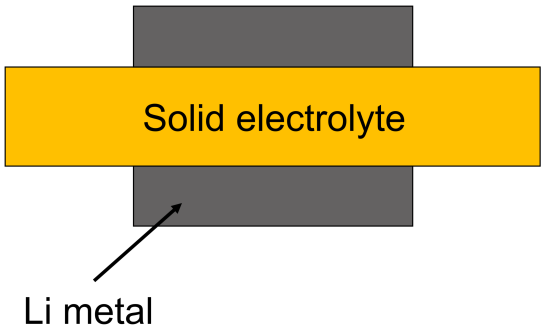

Figure 1-3: Schematic of a Li/LLZO/Li symmetric cell.

Observations of short circuits in this body of literature are again reported at a critical current density, although the experimental context is now slightly different in comparison to unidirectional Na deposition on β-alumina electrolytes due to the experiments occuring at room temperature. Primarily, galvanostatic (constant current)

cycling experiments are performed in which lithium is electrodeposited bidirectionally in cells where lithium is both the positive and negative electrode (symmetric cell). The current is then typically increased between cycles of fixed length until a short circuit is observed [3, 11, 12]. A schematic of a symmetric cell is shown in Figure 1-3.

Although experimental conditions differ between the Na deposition work on β"-alumina and modern Li deposition work on garnets (i.e., the use of liquid Na at 300°C in contrast to solid Li at ambient temperature, or differing magnitudes of the current densities involved), similar qualitative trends have been observed in both systems. The "critical current density" rises with increasing temperature [11], improved electrolyte longevity is reported during symmetric cell cycling at elevated temperatures, and traces of plated metal are found within the electrolyte after cell failure [36].

The first body of work adopting a fracture mechanics (i.e. Griffith flaw) interpretation to the metal penetration problem was performed by Porz et. al [3]. Porz et. al. performed cyclic electrodeposition experiments using symmetric Li/SSE/Li cells in which the SSE is amorphous, single crystalline, or polycrystalline. Lithium metal penetration leading to electrical shorting was observed in all three classes of SSEs, including for a garnet oxide having a shear modulus far above the criterion suggested by Monroe and Newman [35] (e.g., at least twice that of lithium metal).

In the polycrystalline SSEs, lithium propagation appeared to preferentially follow grain boundaries, which others have also observed [12]. However, even in amorphous LPS and single crystalline LLZTO garnet, propagation of lithium metal-filled cracks was observed. These results point to a mechanism for lithium penetration whereby the lithium "dendrites" initiate at surface flaws. Results suggested that when lithium metal electroplates onto the SSE, pre-existing surface flaws (e.g., grain boundary grooves or multigrain junctions if the SSE is polycrystalline), are first filled with electroplated metal. These become preferred sites for subsequent electrodeposition, thereby driving fracture of the bulk electrolyte via stress amplification at crack tips in a manner analogous to established models for brittle fracture [39, 41, 42, 44].

In the remainder of this thesis, we study the metal electrodeposition problem for room-temperature alkali metals from the perspective proposed by Porz et al [3].

We note that this interpretation is analogous to the Poiseulle model of electrolyte fracture, proposed by Armstrong in earlier work on the electrodeposition of liquid Na metal [45].

1.4 Overview of the thesis

The thesis investigates the process by which metals infiltrate solid state electrolytes during electrodeposition and presents solutions towards mitigating this failure mode. The first half of this presents mechanistic studies of this phenomena, designed under the hypothesis that short circuits in solid electrolytes occur above a critical current density due to the accumulation of stresses at surface flaws during plating. In particular, we investigate two predictions of the Poiseulle-Armstrong-Porz model of plating-driven solid electrolyte fracture:

1. All else being equal, metal dendrites should grow preferentially at the regions of highest local current on the solid electrolyte surface.

2. All else being equal, softer electrodeposited metals should exhibit higher critical current densities for solid electrolyte fracture.

The second half of this thesis presents approaches towards alleviating mechanical instabilities at the metal-solid interface by incorporating a liquid metallic phase. We show that such liquids can raise the critical current density of such interfaces through the relief of interfacial stresses or the homogenization of plating currents. We further show that such liquids can also raise the accessible areal capacity of metal anodes through the suppression of interfacial voids that form during metal stripping. The remainder of the thesis is organised as follows:

Chapter 2 investigates Li penetration into a single crystal SSE during Li electrodeposition. We show that conventional choices for electrode geometry and SSE thickness result in a non-uniform current density distribution, where current is focused at the perimeter of the electrodeposition electrode. Li infiltration is seen to

occur predominantly at these edges at which the current is amplified, overriding the presence of larger surface defects elsewhere.

Chapter 3 is a systematic study of the dependence of the critical current density on the yield stress of the electroplated alkali metal. We first characterize the electrical, mechanical, and surface properties of three polycrystalline solid electrolytes: $Li_{6.75}La_3Zr_{1.75}Ta_{0.25}O_{12}$, Na-β"-$Al_2O_3$, and K-β"-$Al_2O_3$. These materials conduct Li^+, Na^+, and K^+ ions, respectively. These solid electrolytes possessed similar ionic conductivities (1–2 mS cm^{-1}), fracture toughness (2–3 MPa $m^{0.5}$) and could be processed to a similar surface finish. These solid state electrolytes therefore allow a direct comparison of behavior between the three pure metal electrodes accross all three working ions. We subsequently show that for pure metals in the Li–Na–K system, the critical current densities scale inversely to mechanical deformation resistance.

Chapter 4 demonstrates two novel electrode architectures in which the presence of a liquid phase enables high current densities while preserving the shape retention and packaging advantages of solid electrodes. First, biphasic Na–K alloys show K^+ critical current densities (with the K-β"–Al_2O_3 electrolyte) that exceed 15 mA cm^{-2}. Second, introducing a wetting interfacial film of Na–K liquid between Li metal and the LLZTO solid electrolyte doubles the average critical current density from 0.5 to 1.21 mA cm^{-2}. This improvement in critical current density is attributed to the Na-K inhibiting the growth of interfacial voids that form during Li stripping, thereby homogenizing subsequent plating currents.

Chapter 5 further explores the functionality of a thin layer of liquid Na-K alloy at the interface between Li metal and LLZTO SSE. We show that this interlayer permits the stripping of Li metal at much higher current densities and areal capacities than is possible without the Na-K film. We further show that the Na-K interlayer eliminates the traditional need for large applied stack pressures and heat treatments to enable the stable stripping of Li metal. These improvements in interface quality and accessible areal capacity are additionally ascribed to the Na-K film suppressing void formation at the interface from which Li is being stripped.

The mechanistic detail of the metal penetration problem has hitherto been largely

unexplored, and this thesis provides new insights into this process. This thesis further presents two original solutions that alleviate this problem at the metal electrode-solid electrolyte interface. This information enables the rational design of solid state battery systems with high energy density and rate performance.

THIS PAGE INTENTIONALLY LEFT BLANK

Chapter 2

Effects of macroscopic current focusing on metal penetration

In this chapter, Li electrodeposition was performed on single-crystal $Li_6La_3ZrTaO_{12}$ garnets. In single crystals, grain boundaries are excluded as paths for Li metal propagation. Vickers microindentation was used to introduce surface flaws of known size. However, operando optical microscopy revealed that Li metal penetration propagates preferentially from a different, second class of flaws. At the perimeter of surface current collectors smaller in size than the Li source electrode, an enhanced electrodeposition current density due to electric field focusing causes Li filled cracks to initiate and grow to penetration. This current focusing is observed to be the dominant factor determining the initiation sites for Li propagation, even when large Vickers defects are in proximity.

The contents of this chapter were first published in Ref. [53]. Richard Park and Tushar Swamy performed and interpreted the electrochemical measurements. Daniel Rettenwander, Stefan Berendts and Reinhard Uecker synthesized the single crystal $Li_6La_3ZrTaO_{12}$ (LLZTO) sample.

2.1 Introduction

Short circuits in single crystal electrolytes occur as a result of stress generation sufficient to fracture the electrolyte during metal electrodeposition [3]. Two mutually compatible processes that dictate stress generation are considered in this work. First, a surface (or internal) flaw leads to current focusing that locally enhances the Li flux. Li accumulation inside of this flaw can generate internal stress, which is thermodynamically limited by the electrical overpotential (i.e., if the stress is sufficiently high it will counteract the electrochemical driving force). This internal stress causes extension of the Li-filled surface flaw if the elastic energy release rate exceeds the fracture resistance of the electrolyte [3].

The second process that must be considered is that removal of Li from the flaw will mitigate the internal stress build-up. For example, prior work with liquid sodium electrodes considers analogous models based on Poiseuille flow, which is valid for laminar flow of liquids. In our case Li "extrusion" out of filled flaws may occur due to creep and/or plastic deformation of the metal. In Li, these mechanisms are currently not well understood, particularly at the small length scales that are relevant inside of solid electrolytes [54]. However, the balance between the Li insertion and removal mechanisms that are outlined above produces a unique relationship between the electrodeposition current density and the stress required to extend metal filled cracks [48–51, 55–57].

It should be noted that the equilibrium hydrostatic stresses which correspond to the applied overpotential are a thermodynamic upper bound on the electrochemically generated stress inside of the flaw. Stress relaxation due to extrusion (or possibly other processes) can then lead to a lower, kinetically limited stresses inside of the actual flaw.

Based on this interplay between Li insertion and removal, the threshold for the extension of a Li filled filament through a solid electrolyte can be described in terms of either a critical overpotential or current density. That is, at any given overpotential (or current density), there is a critical flaw size above which extension is energetically

favorable. The relationship between this critical size and overpotential (or current density) is in principle amenable to experimental evaluation. While the overall electrical potential or current density is easily controlled in typical electrochemical cells, it is difficult to know the distribution of defects in the system, and especially at the SSE surface. The basic energetic argument that we have put forth is analogous to Griffith theory, wherein the largest defect is expected to propagate most readily (i.e., at the lowest critical overpotential or critical current density). Thus, we conducted the converse experiment to test our hypothesis: Sharp defects of such large size that they assuredly lie at the high end of the flaw size distribution were introduced through microindentation (here with a Vickers square pyramid). These were then used to investigate Li metal propagation as a function of overpotential and current density. However, in the course of investigating the effects of large controlled flaws, we discovered that variations in current density due to the geometric configuration of surface current collectors can have a larger, dominant effect on Li penetration.

2.2 Methods

2.2.1 Synthesis and characterization of single crystal LLZTO

Single crystal LLZTO was grown by the Czochralski method directly from the melt. The starting materials, Li_2CO_3 (99%, Merck), La_2O_3 (99.99%, Aldrich), ZrO_2 (99.0%, Aldrich), Ta_2O_5 (99.99%, Aldrich) were dried, mixed in a stoichiometric ratio with 10 wt% excess of Li_2CO_3, then pressed as a pellet and sintered at 850°C for 4 h. The pellet was melted in an iridium crucible under nitrogen atmosphere by RF–induction heating using a 25 kW microwave generator, and an iridium rod was used as a seed to pull the single crystal at a rate of 1.5 m h^{-1} with 10 rpm rotation.

Slices of the sc-LLZTO having typical dimensions of 5 × 5 × 2 mm were embedded in epoxy for ease of handling. The two largest parallel surfaces were polished using an EcoMet 250 Pro Grinder Polisher (Buehler, Lake Bluff, Illinois, USA). The samples were first polished using 600 grit size SiC abrasive paper to reveal two faces.

To obtain finely polished faces, the samples were then sequentially polished using aqueous diamond suspensions of 9 µm and 1 µm particle size, for 25 min and 10 min, respectively, resulting in a mirror finish. The relatively large thicknesses were used to facilitate observations of flaw propagation at optical microscopy resolution. AFM surface scans of the sample were taken with an Asylum Research Cypher AFM (Asylum Research, Santa Barbara, California, USA). SEM imaging of the samples was conducted using a Merlin GEMINI II SEM (Carl Zeiss Microscopy, Jena, Germany) operating at 15 kV accelerating potential and 215 pA current. All samples were prepared in an argon-filled glovebox (oxygen and water levels below 0.1 ppm) and transported to the SEM using an anaerobic transfer box, the design and operation of which is described elsewhere [58].

A Vickers micro-indenter (LECO LM248AT) was used to place several (typically four) indents on the sc-LLZTO surface. The applied load was sufficient to produce cracks that emanate from the corners. These cracks have a semicircular crack front that extends normal to the surface into the crystal. By varying the applied load, a range of crack lengths is produced.

The crystallographic orientation of the polished sc-LLZTO facet parallel to the working and counter electrodes, the crystal facet representing the cross-sectional surface, and the direction of the Li filaments internal to the LLZO crystal was performed with a Bruker D8 Discover X-ray diffractometer using a Cu Kα X-ray source and a Vantec 2000 area detector.

2.2.2 Electrochemical cell assembly and testing

Following indentation, gold electrodes of 2 × 2 mm square or 3 mm diameter circular shape were sputtered onto the sc–LLZTO, being sure to cover the area containing the indents. This gold electrode is the surface onto which Li metal is subsequently electrodeposited. Because gold readily alloys with Li metal, the nucleation overpotential required to plate Li metal at the inception of the experiment is low [59], ensuring that the applied overpotential is largely transmitted to the electrodeposited Li metal. A piece of Li foil (0.75 mm thickness, 155 mAh cm^{-2}) was then placed between the solid

electrolyte and a stainless-steel current collector to complete the cell assembly. The shape and area of the Li counter electrode is therefore equal to that of the sc-LLZTO solid electrolyte, which is 20–30 mm^2 for the samples used. In this configuration, the Li flux from the metal counterelectrode is focused on the smaller area of the gold working electrode (4 or 7 mm^2).

Before electrochemical cycling, the cell was heated to 170°C for 1h and slowly cooled to room temperature. We found that this procedure greatly reduced the interfacial impedance of the cell, allowing the application of high current densities (up to 10 mA cm^{-2}), while maintaining WE potentials well below 5.0 V. This may be important for avoid SSE oxidation at the positive electrode during the experiment [60].

Galvanostatic experiments were conducted using a Solartron 1400/1470E cell test system. *In-situ* Li plating activity unto the working Au electrode was recorded using an optical microscope (Firefly Global GT825, Belmont, Massachusetts, USA). *Ex-situ* microscopy was conducted using the Olympus BH (Olympus, Shinjuku-ku, Tokyo, Japan) and Stereomaster II SPT-ITH (Fisher Scientific, Hampton, New Hampshire, USA) microscopes.

2.2.3 Finite element modelling of electrochemical cells

Gold WE, Li CE, and SSE diameters were initially set to 2, 4, and 12 mm, respectively (WE/CE diameter ratio = 0.5). The SSE thickness was set to 2 mm, and the voltage across the SSE was set to 4 V. These parameters closely matched experimental conditions. To our knowledge, the dielectric constant of LLZO garnets have not been measured; here the value was set to 3.8, the dielectric constant of quartz (a representative ceramic material). The assumed value of the dielectric constant does not affect the current and electric field intensification factors of interest here. The spatial distribution of the electric field and hence the current density (being linearly proportional to electric field) was computed using the electrostatics module of the COMSOL Multiphysics finite element software.

2.3 Results and discussion

Our experimental configuration creates a Li flux from a Li metal counterelectrode (CE) through a highly polished single crystal of $Li_6La_3ZrTaO_{12}$ (sc-LLZTO) garnet to a gold working electrode (WE), at which the Li metal electrodeposits. Operando observations were made (Figure 2-1) of the morphology of the deposited Li metal, and the initiation and growth of Li metal filled cracks (if present) at the WE/SSE interface. Single crystal LLZTO was used to create a "best case" situation where the grain boundaries and residual porosity present in polycrystals are excluded as possible initiation sites. A tungsten needle was used to make electrical contact to the surface of the gold working electrode. Galvanostatic experiments were conducted, at current densities producing a cell voltage of 3.5–4V, which based on a previous failure model, should be sufficient to propagate even nm-scale surface flaws [3]. Optical microscopy was used to observe the Li plating behavior in real time, during which the entire apparatus was housed in an argon-filled glove box with oxygen and water content below 0.1 ppm and 0.1 ppm, respectively. The ionic conductivity of the sc-LLZTO SSE was previously measured via electrochemical impedance spectroscopy (EIS) to be 0.2 mS cm^{-1} [3]. The crystal structure, single crystallinity, and phase purity of the sc-LLZTO have previously been confirmed via X-ray diffraction (XRD) [61].

2.3.1 Surface and mechanical property characterization

Typical scanning electron microscopy (SEM) and atomic force microscopy (AFM) images of the polished surface are shown in Figures 2-2 (a) and (b), respectively. The SEM image is nearly featureless, whereas the AFM scan reveals linear features of sub-micrometer width resulting from polishing. Still, the polished surfaces have a rms roughness of only 0.2 nm (measured over a 10 µm × 10 µm scan area). As previously noted [3], even highly polished surfaces will have a distribution of defect sizes, amongst which the largest, controlling flaws can be exceedingly difficult to find. Therefore, we elected to introduce surface flaws of controlled and reproducible size that are much larger than any resulting from polishing, to establish the largest, and

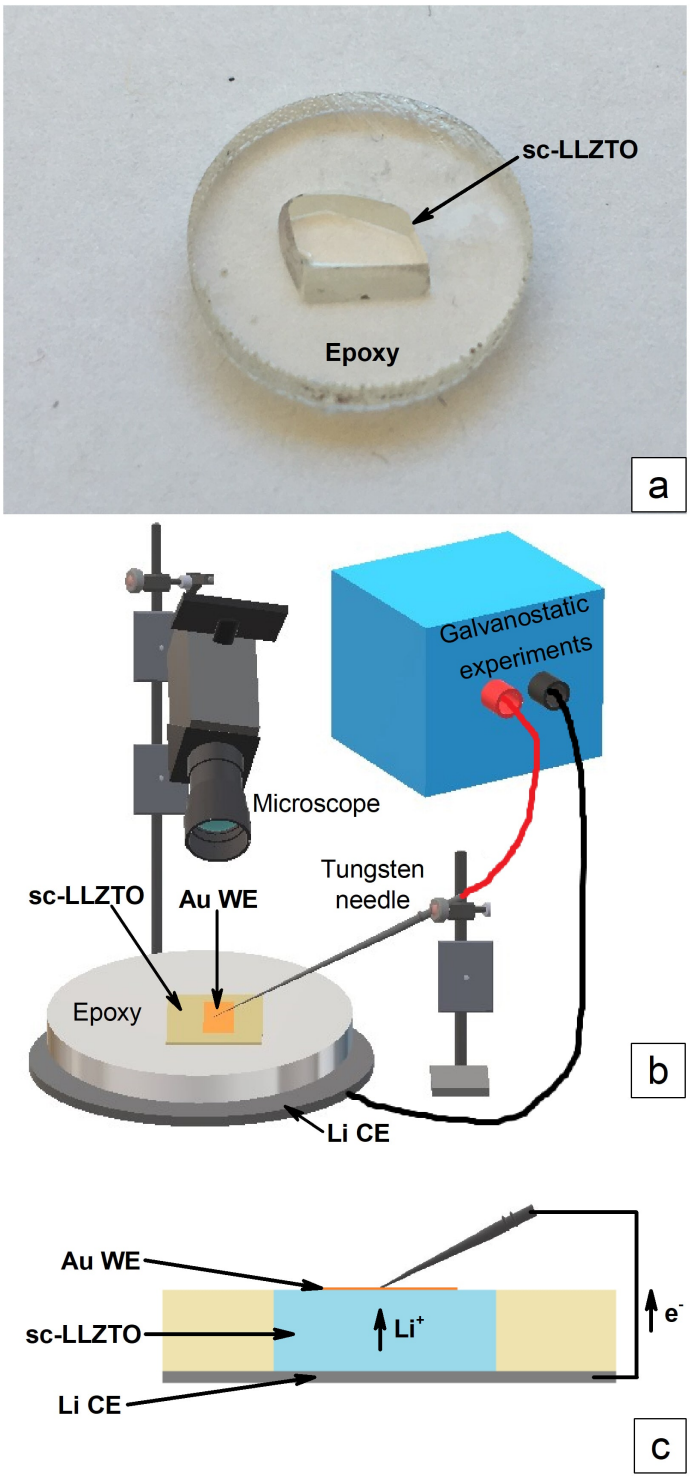

Figure 2-1: (a) Example of single-crystal electrolyte samples used in this study, polished and embedded in epoxy for handling. (b) Schematic of the apparatus used for galvanostatic Li plating from a Li metal counterelectrode (CE) through the sc-LLZTO onto a gold working electrode (WE). (c) Cross sectional schematic of the experiment.

theoretically the controlling, flaw size.

An optical microscopy image of a typical indent array and an SEM image of an indent showing the characteristic corner cracks appear in Figures 2-2 (c) and 2-2 (d), respectively. For indentation loads of 2N, 5N, 10N, and 20N, the crack lengths were measured via optical microscopy to be about 50, 140, 270, and 400 µm, respectively. The corresponding hardness (determined from the square-pyramid indent size) and fracture toughness (determined from the crack length) of the LLZTO were calculated to be 7.5 GPa and 0.6 MPa $m^{0.5}$, respectively, [4] assuming a Young's modulus of 150 GPa as measured previously [6]. These values are reasonably close to Wolfenstine et al.'s results for 97% dense polycrystalline $Li_{6.28}La_3ZrAl_{0.24}O_{12}$ (LLZAO) garnet, 6.3 GPa and 1.14 MPa $m^{0.5}$, respectively [6]. Our slightly higher hardness and slightly lower fracture toughness are reasonable for a single crystal compared to a polycrystal of the same basic composition, as a polycrystal can be somewhat softer due to residual porosity, but also somewhat tougher as the microstructure can deflect cracks. These values also indicate that LLZO-based garnets, as a family, are both softer and less tough than most oxide ceramics. Polycrystalline ceramics typically have fracture toughnesses in the 2–4.5 MPa $m^{0.5}$ range. LLZTO has a low single crystal fracture toughness close to that of ordinary soda-lime-silicate glass (~0.7 MPa $m^{0.5}$) [62], although the Li_2S-P_2S_5 solid electrolytes have even lower values [34].

2.3.2 Operando chronoamperometric experiments

A total of five electrodeposition cells prepared in the manner described in *Methods* were studied, at two different current densities, 10 mA cm^{-2} (3 samples) and 5 mA cm^{-2} (2 samples) the current density being defined with respect to the area of the gold electrode. We choose these current densities assuming that a practical Li metal battery will require an electrode areal capacity of ~5 mAh cm^{-2} and will need to be charged at rates of 1C–2C. The current densities used correspond to these conditions. A summary of the results is presented in Table 2.1.

Four out of the five samples tested exhibited a short circuit. In each case, Li metal penetration through the transparent sc-LLZTO was clearly observed. Of these four, 3

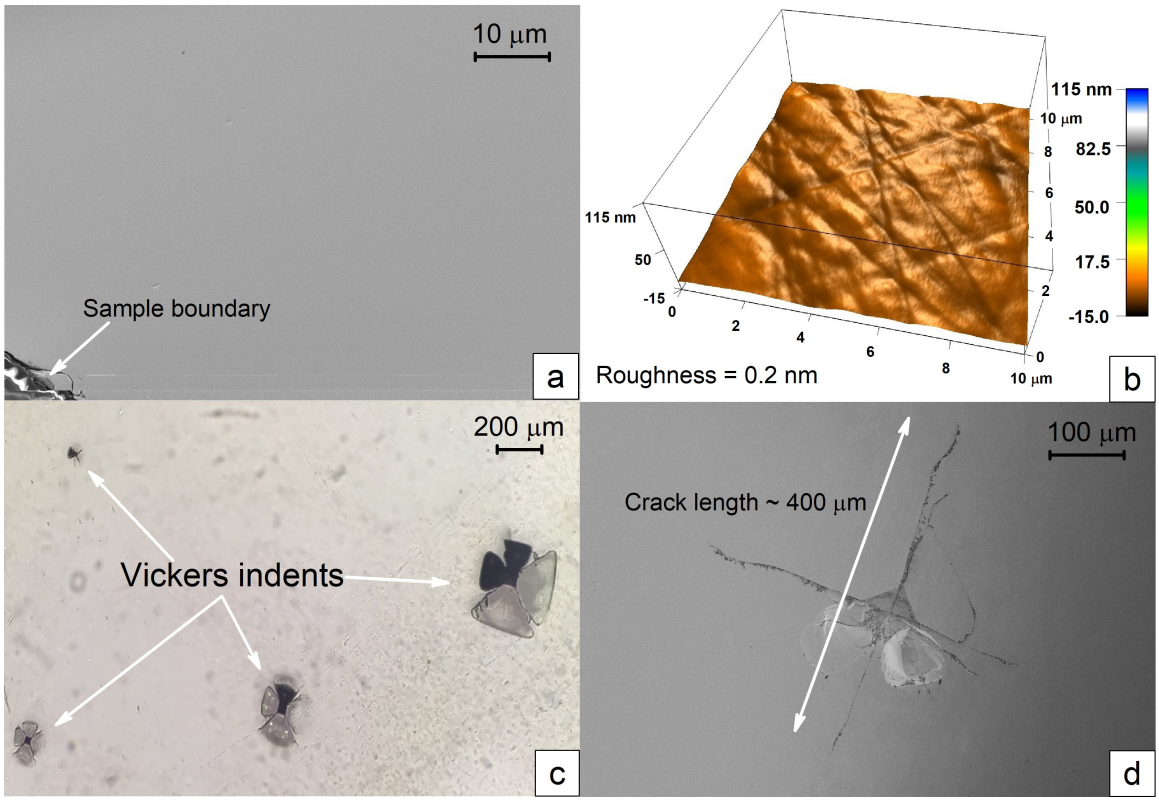

Figure 2-2: (a) SEM image of sc-LLZTO surface polished to a final grit size of 1µm. (b) AFM scan of the sc-LLZTO surface showing linear features from polishing. The rms roughness is 0.2 nm when measured with a scan size of 10 µm × 10 µm and a tip radius of 7 nm. (c) Optical microscopy image of four Vickers indents produced under loads of 2N, 5N, 10N, and 20N. (d) A representative SEM image of the largest indent, for which the crack length is ˜400 µm.

Sample	Current Density (mA cm^{-2})	Electrode Shape	Indent location	Short circuit?	Duration (s)	Shorting location	Li deposited (10^{-5} cm^{-3})
1	10	0.2cm x 0.2cm	4, at center	Yes	37	2, electrode edge	2.2
2	10	0.2cm x 0.2cm	4, at center	Yes	68	Multiple	3.7
3	10	0.3cm diameter (round)	4, at center	Yes	50	3, electrode edge	2.2
4	5	0.2cm x 0.2cm	None	No	240	No shorting	6.5
5	5	0.2cm x 0.2cm	None	Yes	300	1, electrode corner	8.1

Table 2.1: Summary of results for galvanostatic electrodeposition experiments performed on five Au/sc-LLZTO/Li cells in this study.

were tested at 10 mA cm^{-2} and one at 5 mA cm^{-2}. However, all short-circuited samples exhibited Li penetration originating at the perimeter of the gold working electrode, away from the introduced defects. One sample exhibited penetration originating from both the edge, the largest introduced indent, and a location in the middle of the electrolyte free of introduced defects.

At 10 mA cm^{-2} current density, a short circuit was observed in less than 1.5 min; the specific experiments correspond to 2.2–3.7 $\times$ 10^{-5} cm^3 of electrodeposited Li metal. The sample that short-circuited at 5 mA cm^{-2} did so in 5 min, after which a larger Li metal volume of 8.1 $\times$ 10^{-5} cm^3 had been deposited. This indicates that at the lower current density of 5 mA cm^{-2}, more of the deposited Li is not contributing to the filament but being deposited elsewhere. Below, we discuss the data from two of the cells tested at 10 mA cm^{-2}.

In-situ optical microscopy images of Sample 1 before and after short-circuiting are shown in Figures 2-3 (a) and 2-3 (b), respectively. (A portion of the sputtered gold electrode is missing at the left side, having been scraped off by the tungsten current collector during setup.) Li metal filaments were observed to initiate and propagate within the first 5 seconds after the application of current. Figure 2-3 (c) shows the voltage-time trace for this experiment, where the sudden drop to zero voltage at 37s corresponds to the growth of a metal filled crack completely through the 2 mm thickness of the single crystal. One filament in particular grows most rapidly in 2-3 (b) to penetration. The elapsed time to short-circuit for this filament corresponds to a plated Li volume of ~2.2 $\times$ 10^{-5} cm^3 (~4.5 µAh of charge passed). Notice in Figure 2-3 (b) that both instances of Li filament formation occur at the perimeter of the gold electrode, and that Li penetration did not ensue from the large Vickers indents towards the center of the gold electrode.

These observations were consistent amongst the three electrodeposition cells exhibiting a short circuit at 10 mA cm^{-2}: Li metal penetration initiated at the perimeter of the gold current collector and grew through the single crystal to penetration. *In-situ* optical microscope images of the second electrodeposition cell, Sample 2, prior to the experiment and post short-circuit are shown in Figure 2-4 (a) and 2-4 (b), re-

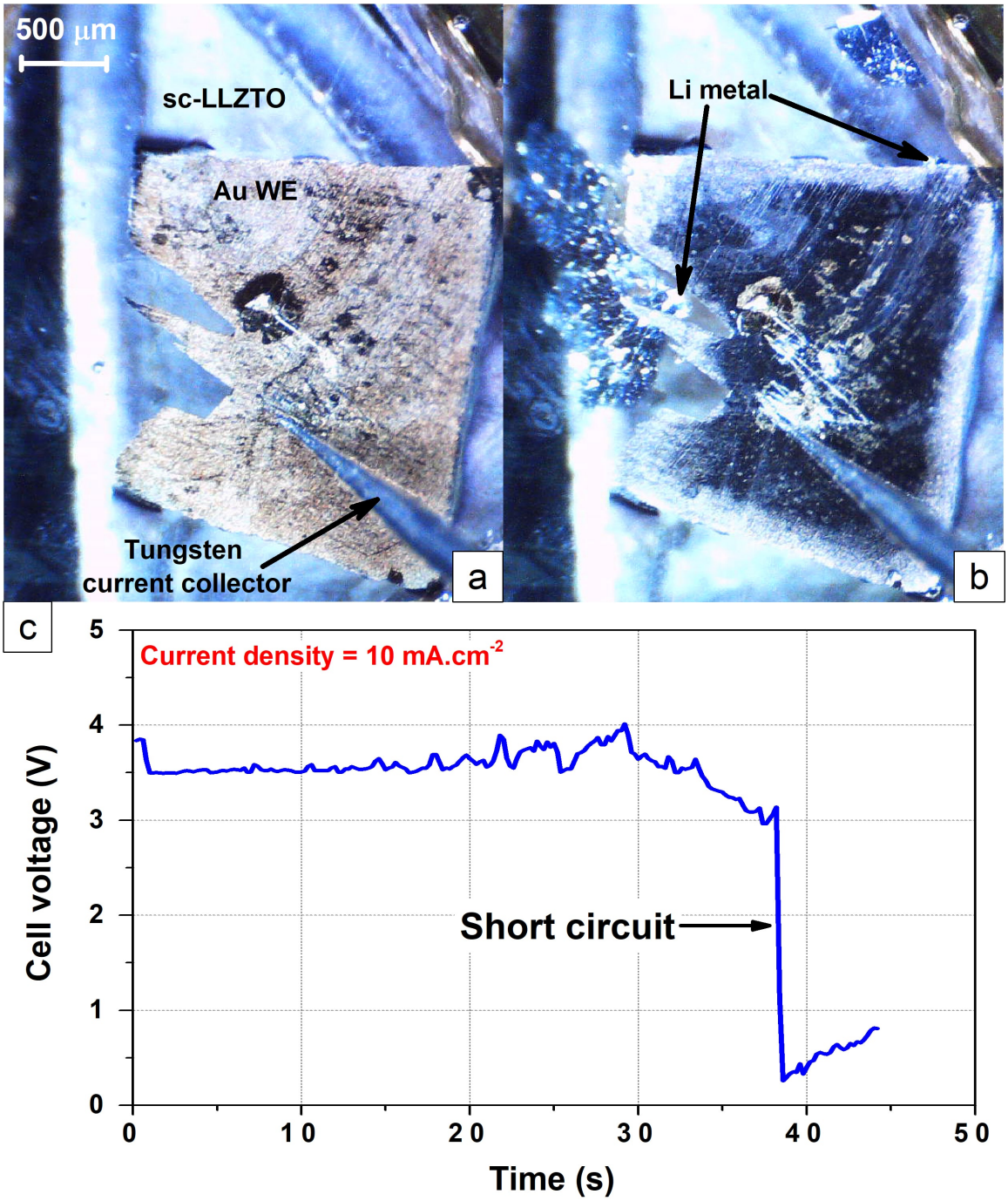

Figure 2-3: Plan-view *in-situ* optical microscopy images (a) prior to the experiment, and (b) post short-circuit, of a sc-LLZTO during galvanostatic deposition of Li metal beneath the gold WE at 10 mA cm^{-2} current density. The camera viewing direction is normal to the plane the gold electrode, as shown in Figure 2-1. (c) The corresponding voltage-time trace, showing a sudden drop upon short-circuiting.

spectively. In this second cell, the cell voltage remained relatively steady at 3 V until a short circuit occurred 68 seconds into the experiment, corresponding to a plated Li volume of ~3.7 × 10^{-5} cm^3 (charge passed was ~7.6 µAh). In the third cell that underwent a short circuit, metal penetration into the bulk initiated 5 seconds into the experiment, and lasted for approximately 50 seconds, corresponding to a plated Li volume of ~2.2 × 10^{-5} cm^3 (4.5 µAh of charge passed).

In one of the samples tested at 5 mA cm^{-2}, a short circuit did not initiate within the experimental time of ~240 seconds, which corresponds to a plated Li volume of ~6.5 × 10^{-5} cm^3 (~13.3 µAh charge passed). The experiment was terminated when the cell voltage rose sharply. We believe that this impedance rise corresponds to the formation of a gap at the counter electrode, as the interface between the counter electrode and the sc-LLZTO could be observed to discolor *in-situ*. The sample tested at 5 mA cm^{-2} that did short-circuit did so at ~300 seconds, corresponding to a plated Li volume ~8.1 × 106 $µm^3$ (~16.6 µAh charge passed).

The repeated observation that Li metal penetration initiates at the working electrode edge suggests that current focusing at current collector discontinuities is important. We address this topic in detail in a subsequent section.

2.3.3 Subsurface observations

Ex-situ optical microscopy was performed on the sc-LLZTO samples that exhibited a short circuit to examine the initiation sites at which Li penetrated the single crystal, and the morphology of the Li filaments within the solid electrolyte. Three key observations are noted. Firstly, crack growth ahead of the Li filament that did not lead to catastrophic fracture was observed within the electrolyte. That is, cracks that are not filled with Li metal, as well as those that are, appear to have propagated stably under the electrochemically-created load. Second, plan view observations of the sc-LLZTO after polishing off the gold electrode revealed metal deposition at the introduced Vickers indent in only one instance out of a total of 16 indents. Clearly, the Vickers indents did not dominate the shorting behavior. Thirdly, transverse views of polished single crystals that exhibited a short circuit showed conclusively that the

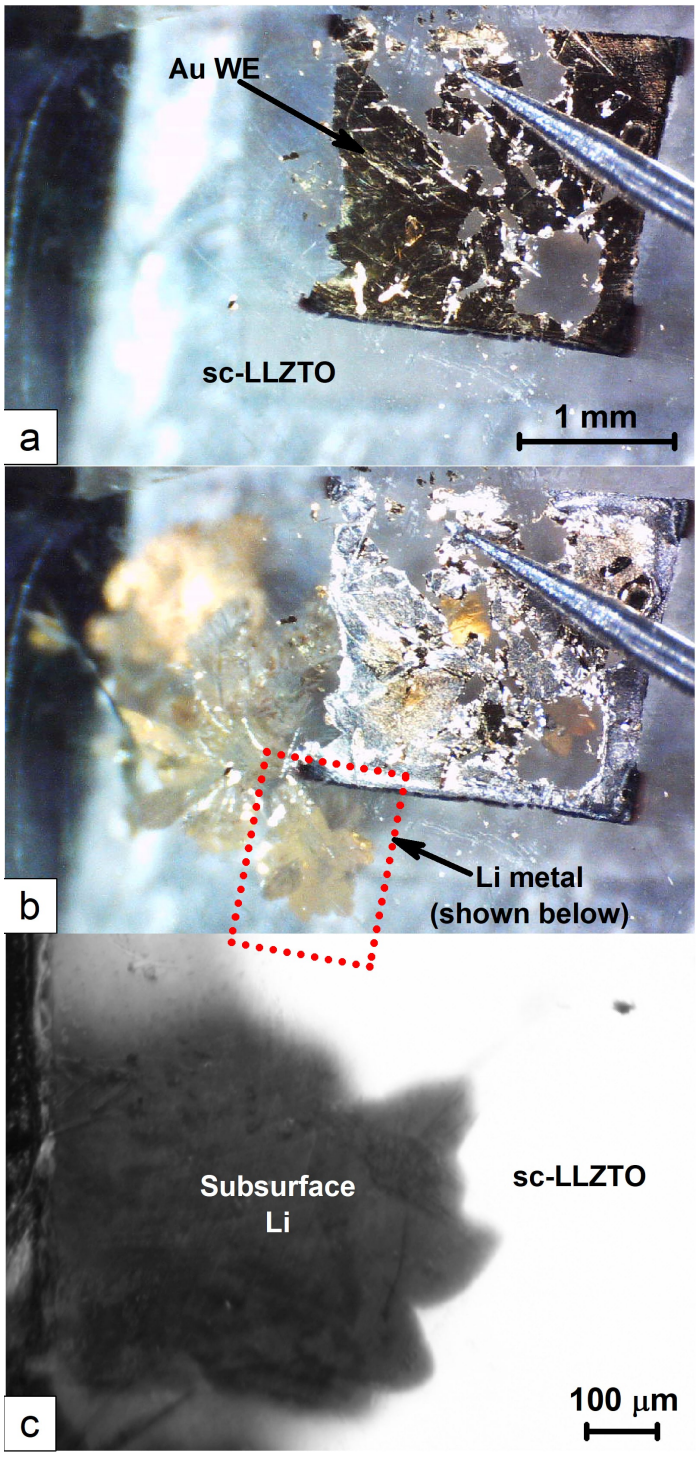

Figure 2-4: *In-situ* optical microscopy images (a) prior to the experiment, and (b) post short-circuit, of a sc-LLZTO with sputtered gold WE during galvanostatic deposition of Li metal beneath the gold WE at 10 mA cm^{-2} current density. (c) *ex-situ* optical microscopy image of the region marked in Figure 2-4 (b), focused on the surface of the gold working electrode.

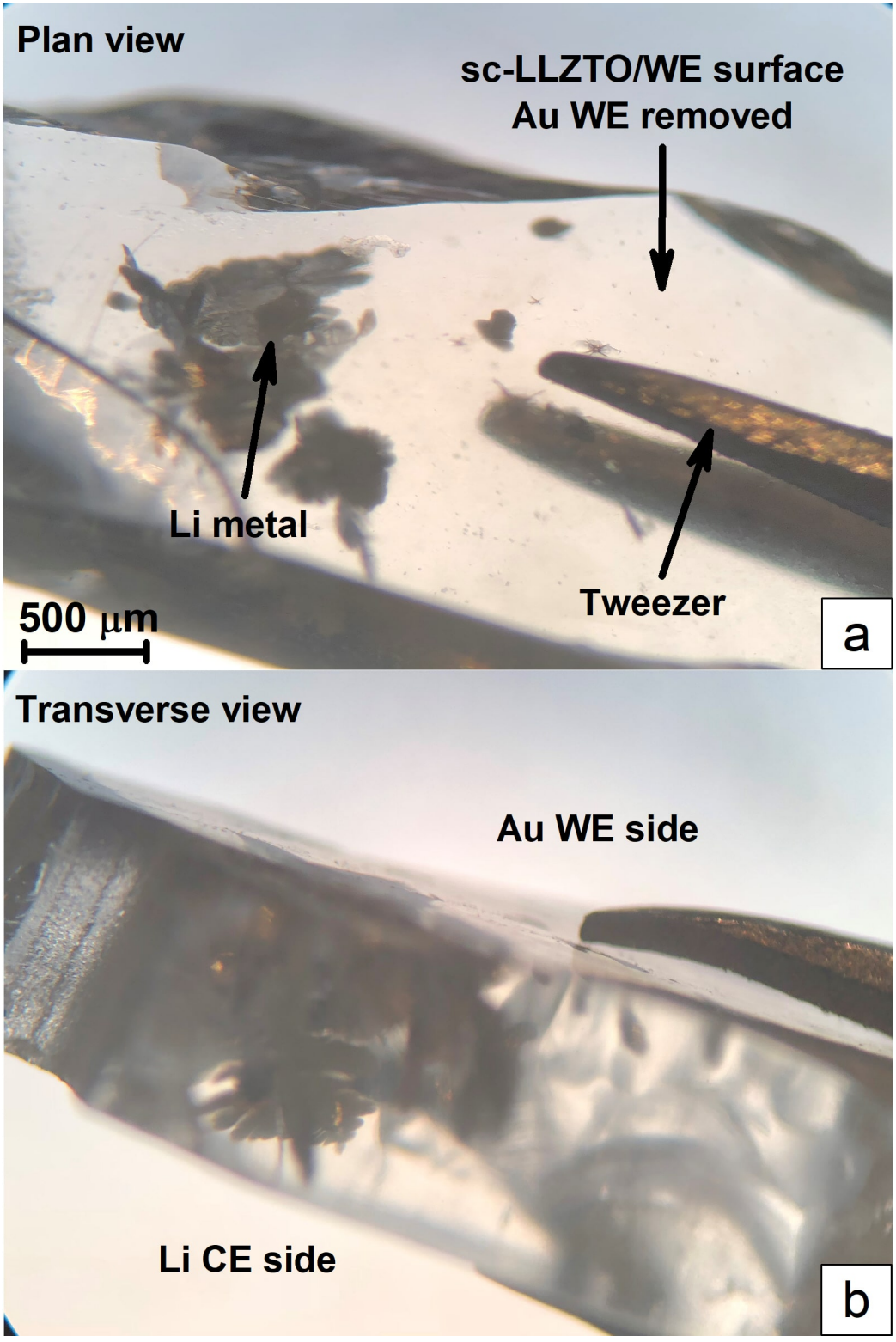

Figure 2-5: (a) Plan and (b) transverse views of the solid electrolyte showing the leaf-like morphology of the Li metal filaments that have penetrated into, or completely through, the sc-LLZTO.

Li metal penetrated through the entirety of the solid electrolyte.

An optical microscopy image of a Li filament in Sample 2, taken before the gold electrode was polished away, is shown in Figure 2-6. Here, we focus on a subsurface crack that has formed ahead of a Li filament. A second image of this site is shown in Figure 2-4 (c) in which the aforementioned crack is invisible at a different focal depth. These images correspond to the site labelled "Li penetration" in Figure 2-4 (b). Upon imaging through-focus, it was clear that Li filled cracks are always opaque, and that the crack ahead of the Li is not filled. This observation shows that crack-opening stresses produced by Li metal deposition inside of a flaw can produce stable crack extension without catastrophic fracture of the electrolyte. Based on the mechanism proposed in our previous publication, the extension of a Li filled filament will instantaneously decrease the mechanical driving force (i.e., the strain energy release rate), such that stable crack growth is expected to occur. This is consistent with the observed behavior. However, our original explanation (Figure 9 in Porz et al.) [3] considers the extension of Li filled filaments. The new images showing cracks ahead of the filament that do not initially contain Li indicate that another related phenomenon is possible. Here, it appears that the fracture resistance for the extension of an unfilled crack is lower than that for one filled with Li. This, for example, is expected to occur if the Li/LLZTO interfacial energy is larger than the LLZTO surface energy. In these cases, the continuing flux of Li should fill the empty crack tip, ultimately increasing the internal pressure and inducing additional crack extension.

An optical microscopy image of Sample 2 taken after polishing the gold working electrode from the short-circuited sample is shown in Figure 2-6 (b). This image reveals the initiation sites for Li penetration at the sc-LLZTO surface beneath the gold WE, the perimeter of which is outlined in white. Here we see three Li filament nucleation regions, labeled 1–3. By far, the greatest amount of Li metal penetration has occurred from location 1 at the edge of the gold working electrode. This condition was observed in all four of the electrodeposition cells that exhibited a short circuit.

Closer examination of location 2, Figure 2-6 (c), revealed that a Li-metal filled

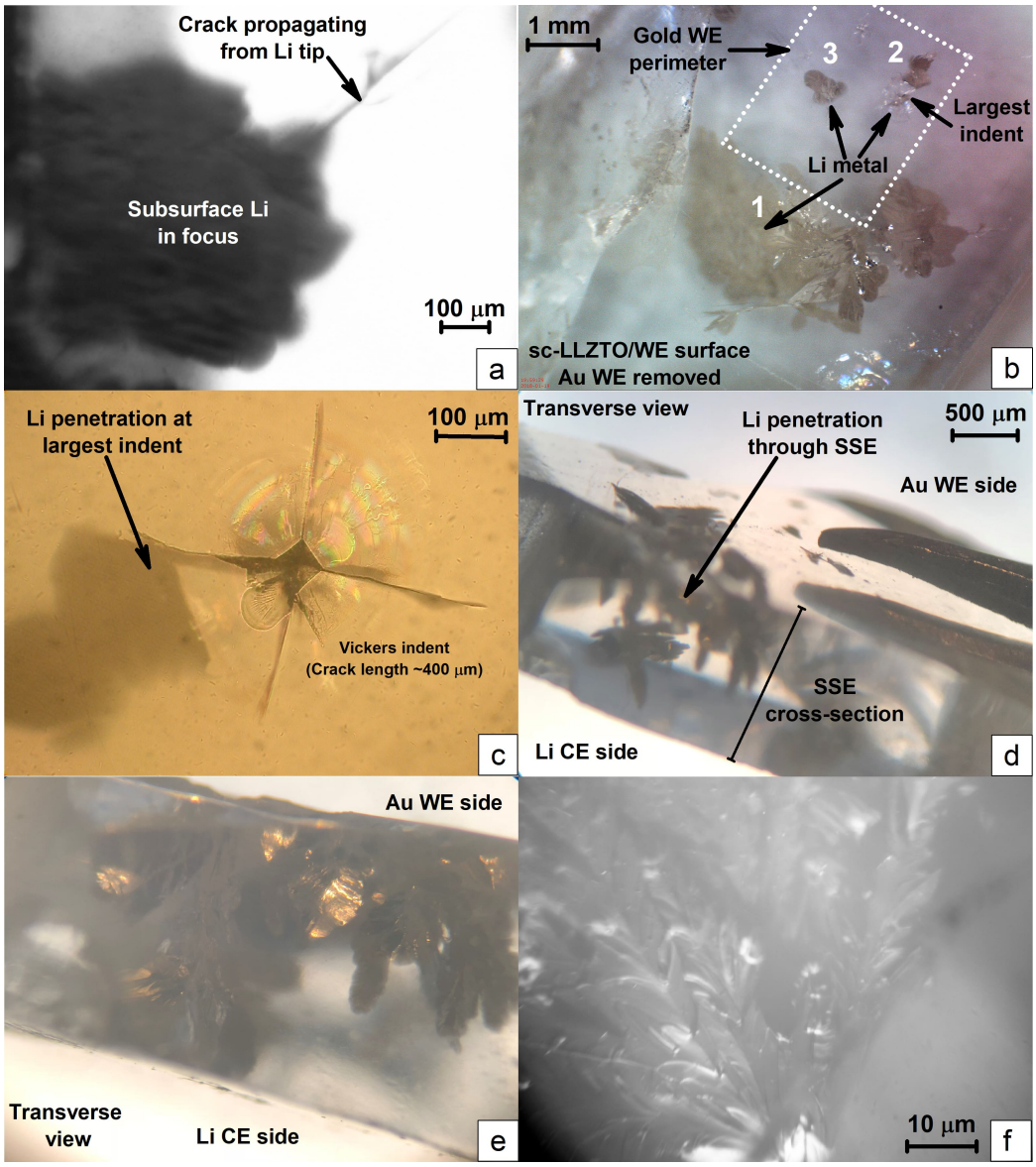

Figure 2-6: (a) Post short-circuit transverse view *ex-situ* optical microscopy image of sample 2, focused on a subsurface Li filament within the single crystal LLZTO. A crack that is apparently free of Li metal emanates from the Li filament tip. (b) Plan view optical microscopy image of sample 2 after the gold WE has been removed. The original WE perimeter is outlined in white. Li nucleation and growth has occurred at three locations, labeled 1–3. (c) Magnified plan view of location 2, showing a Vickers indent and associated corner-cracks, from one of which a Li metal filament has grown. This is the largest indent in this sample. (d) and (e) Transverse views of the solid electrolyte showing the leaf-like morphology of the Li metal filaments that have penetrated into, or completely through, the sc-LLZTO. (f) Magnified optical microscopy image of the leaf-like growth morphology of a Li metal-filled crack, taken in transverse view.

crack had in fact initiated from one of the corner-cracks produced by the largest of the four Vickers indents. (Recall that in the Vickers indentation method, the most severe flaws produced are not the indentation, but rather the atomically-sharp cracks extending outwards from the corners of the indent and into the body of the sample). Although this one example conforms to our initial expectations that a large intentional defect would seed the growth of Li metal, none of the other of the 12 Vickers indents in samples 1–3 showed this behavior. Even more surprising was the observation at location 3 in Sample 2 (2-6 (b)) of a Li metal filament initiating from a region with no apparent surface defect, yet in close proximity to the intentional Vickers indents. Clearly, other factors such as local electric field intensification are dominating the cell shorting behavior.

Transverse views of Sample 2 taken after short-circuiting are shown in Figures 2-6 (d) and (e). Additional plan and transverse views appear in Figure 2-5 (a) and (b). The transverse views show the extent of penetration of various Li filaments from the gold WE. It is firstly clear that some of Li filaments have penetrated completely through the sc-LLZTO and connect the WE to the CE. The single crystal has not, however, fractured completely despite the internal deposition of Li metal (occupying a volume of ~2.6×10^{-5} cm^3). Note that what we have described as Li "filaments" each consists of multiple, planar, metal-filled cracks. The orientation of these crack planes does not appear to follow any particular low-index orientation of the crystal. Single crystal XRD showed that the surface on which the WE is deposited is a {211} plane, and that the polished facet through which the transverse views were taken is {231}. However, LLZTO does not exhibit easy cleavage along a favored plane; this is evident in observations of the single crystal fracture surfaces. Thus, the orientation of the metal-filled crack planes appears to be randomly selected from a crystallographic perspective. Nonetheless, the filaments do not appear to traverse a straight-line path from the WE to the CE, but "fan out" in lateral directions. This is consistent with growth following the electric field distribution, discussed later.

Figure 2-6 (f) shows the morphology of the Li grown through the solid electrolyte. We note the similarities in morphology between the structure of this filament grown

within a single crystal solid electrolyte and the structure of Li "dendrites" grown through liquid electrolytes [63, 64]. A careful investigation into the physical reasons behind this similarity is a focus of ongoing investigations.

2.3.4 Current intensification at electrode discontinuities

Based on the experimental observations, we propose that the preferential initiation of Li filaments at the working electrode perimeter, followed by penetration through the single crystal electrolyte, is due to electric field intensification at the periphery of the gold working electrode. Finite element modeling was performed to quantify the spatial distribution of this intensification. In high temperature sodium-sulfur batteries where the metal is molten, Virkar et al. [48] have previously proposed that electric field intensification can produce short-circuits through ceramic electrolytes.

We model the system as a set of stacked concentric disks representing the gold working electrode, sc-LLZTO SSE, and Li counter electrode, with a potential difference between the two electrodes. The diameter of the electrolyte disk is significantly larger than both the gold and Li electrodes, to allow electrode edge effects to manifest. In this configuration the two metal electrodes possess electric field lines that extend into the dielectric layer (the SSE), beyond the perimeter of the metal electrodes. The electric field distribution is the solution to the Laplace equation under Dirichlet (fixed potential) boundary conditions. The solid electrolyte was treated as an ohmic conductor, and numerical solutions giving the electric field distribution between the Li and gold electrodes were calculated as a function of two dimensionless geometric parameters. **A** is the WE/CE diameter ratio, and **B** is the SSE thickness/CE radius ratio. The results in terms of the current density distributions for four values of **A** (with $\mathbf{B} = 1$ throughout) are plotted in Figures 2-7 (a)–(d). For each value of **A**, the transverse view of the cell is shown at the top, and the plan view at the bottom. Figure 2-7 (a), in which $\mathbf{A} = 0.5$, resembles the experimental conditions for the cells in this study, in the sense that the gold working electrode is smaller than the Li counter-electrode. It can be seen that the Li electrodeposition current density is non-uniform and concentrates at the perimeter when the collector surface area is less than that of

the separator and the Li source. In general, such concentrations are always present at the perimeter of the smaller electrode, independent of the size of the larger electrode relative to the electrolyte area. This can be seen in Figure 2-7 (d), in which current density concentrations can be seen at the perimeter of the smaller Li counterelectrode instead. At a position that is 10 microns from the edge, the electric field is a factor of ~5 times higher, as shown in Figure 2-8 (a). In a single-ion conductor such as LLZO (i.e., unit transference number), the amount of Li metal deposited is exactly proportional to the charge passed. Thus, the repeated appearance of the penetrating Li filaments at the edges of the current collectors (Figures 2-7 (a), (b) and 2-6 (b), is consistent with a higher current density along the perimeter. Furthermore, the observation that metal-filled cracks propagate from isolated locations, rather than uniformly along the perimeter, is consistent with initiation at metal-filled flaws where the electric field is highest.

The operando observations clearly show that the cracks initiate at the interface between the gold electrode and the solid electrolyte, where Li metal is electrodeposited, as was the case in the previous study using a point probe [3]. It is possible that even an atomically smooth, defect-free interface will succumb to local non-uniformities in Li plating, leading to the propagation of metal-filled cracks at sufficiently high driving force. However, in the present case the direct observations of the sample surface (Figures 2-2 (a), (b)) show that polishing leaves behind features of tens to hundreds of nanometer scale. Pre-existing defects of this size should require local overpotentials of a fraction of a volt to propagate, [3] and given that the present galvanostatic tests produce cell voltages of 3.5–4V, it is highly likely that the population of surface defects contains ones of supercritical size. We believe that the intersection of the intensified electric field with such defects leads to the growth of the Li metal filaments, to the exclusion of the larger, intentionally introduced Vickers defects.

We can further use the simulations to understand the results for the current experimental geometry, to extrapolate from those effects to large-area planar battery cells, and to model the effects of a different kind of defect - namely, discontinuities in electrodes and current collectors that may cause local field amplification. Consider-

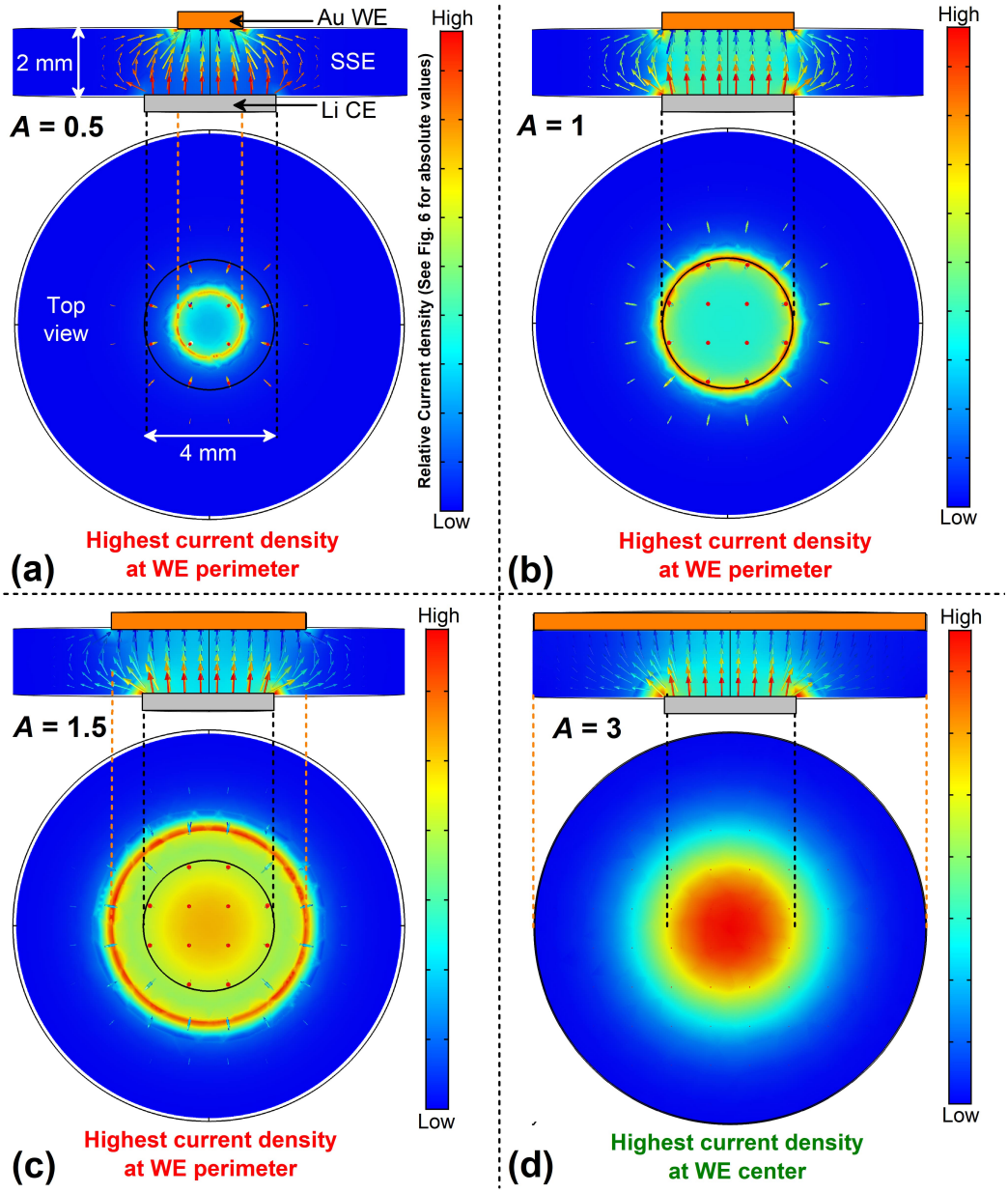

Figure 2-7: Current density contour plots for an Au/SSE/Li cell with a WE/CE diameter ratio (**A**) of (a) 0.5, (b) 1, (c) 1.5, and (d) 3. Corresponding values for electric field are shown in Figure 2-6. The SSE and Li CE diameters are fixed at 4 and 12 mm respectively, and the SSE thickness is fixed at 2 mm. (Accordingly, **B**, the SSE thickness/CE radius ratio, is one). **A** = 0.5 resembles the experimental conditions in this study. For **A** = 0.5, 1, and 1.5, the highest current densities are observed at the WE perimeter, whereas between **A** values of 1.5 to 3, the current density intensification transitions the center of the electrode.

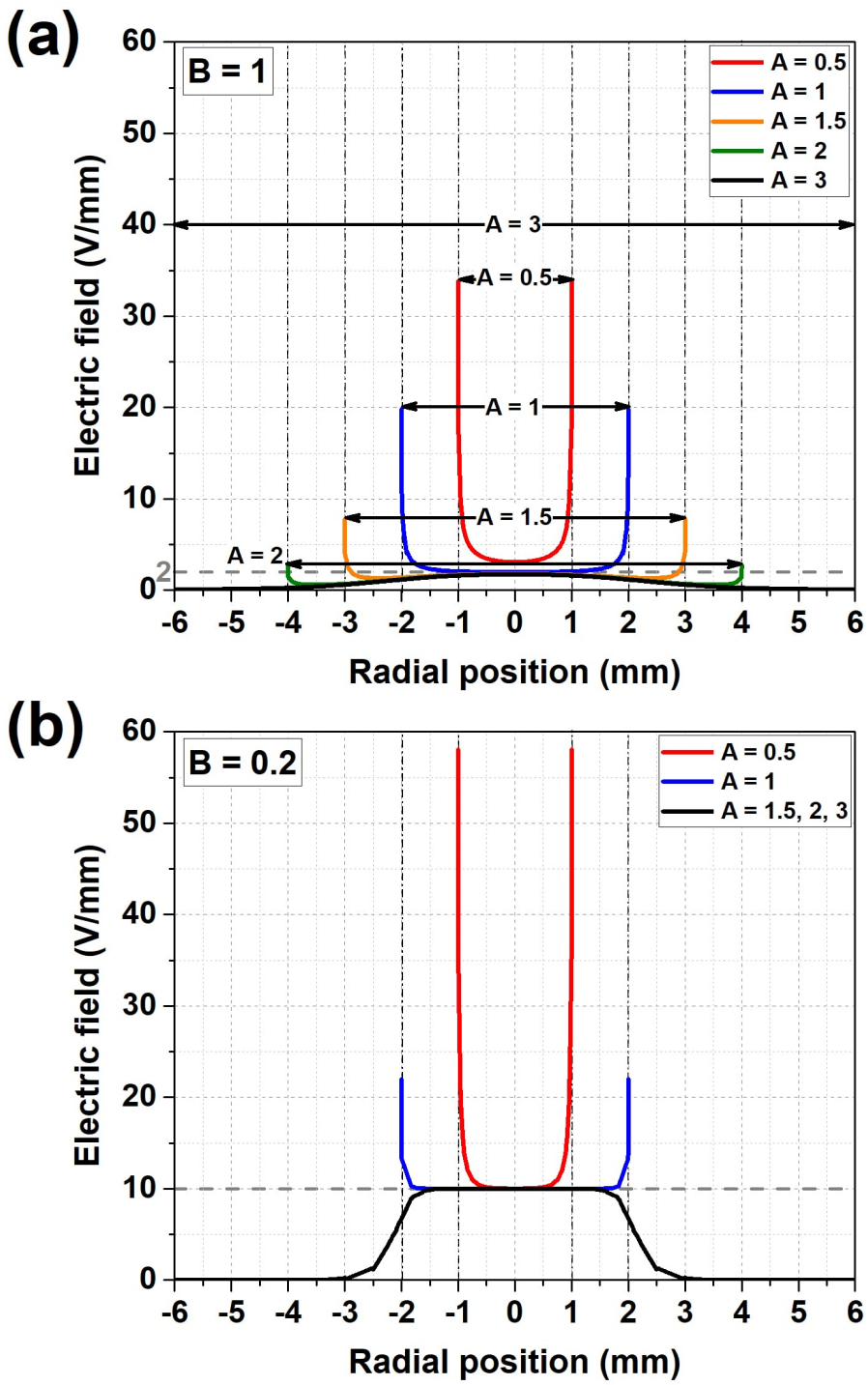

Figure 2-8: Spatial distribution of electric field for WE/CE diameter ratios (**A**) of 0.5, 1.0, 1.5, 2.0, and 3.0 for electrolyte thickness/CE radius ratio (a) (**B**) = 2 and (b) **B** = 0.2. The light grey line represents the macroscopic value of the electric field, defined as the potential difference divided by the electrolyte thickness. SSE and Li CE diameters are 4 and 12 mm respectively, and SSE thickness is 2 mm. **B** = 1 approximates the experimental conditions in this study.

ing first the geometric variable A, which represents the ratio of positive electrode to negative electrode area, the simulations show that the current density amplification factor (i.e., obtained 10 micrometers away from the WE perimeter) decreases as **A** increases; for **A** = 0.5, 1.0 1.5 and 2, the amplification is respectively ~5, ~4.5, ~2 and ~1 (Figure 2-8 (a)). We view these as lower bound estimates of the amplification near the edge, since the solution for the electric field diverges exactly at the edge of the electrodeposition electrode when **A** = 0.5, 1.0 1.5 and 2. This lack of convergence is associated with a mathematical singularity in the electric field at the electrode boundary. We somewhat arbitrarily cite the value 10 micrometers away, based on the premise that this region will contain a large number of sub-micrometer defects like those observed in Figure 2-2.

While in Li-ion batteries the negative current collector usually slightly overlaps the positive current collector, the area ratio **A** is nonetheless close to one. Our results show that it may be advantageous to design such that **A** $>$ 1 to diminish the field amplification. Notice that in Figure 2-8, field enhancement at the edges is completely avoided when **A** = 3. While the critical value of **A** at which edge field enhancement vanishes will vary with geometry, in general, one of our key findings is that a larger positive electrode will help to mitigate electrode edge failures during the charging process of interest to Li metal batteries.

The second geometric variable **B** represents the thickness-to-width aspect ratio of the battery, and for a typical thin-plate design will be less than ~0.1. Upon holding **A** constant and decreasing **B**, the field amplification 10 microns from the current collector edge decreases, but the singularity at the edge is not removed, if **A** $\leq$ 1 and the electrolyte has greater width than the electrodes. Only in the limiting case where the electrolyte width is exactly equal to the width of the negative electrode (and A $\leq$ 1) does the singularity vanish. Furthermore, as **B** decreases, the oversizing of the positive electrode at which the edge field enhancement vanishes also decreases. (This occurs between **A** = 1 and 1.5 for **B** = 0.2, and between **A** = 2 and 3 for **B** = 1). These trends are shown in Figures 2-8 (a) and (b), respectively. Although the ratio **B** for a practical battery is likely to be far below 0.2, examination of smaller

values of **B** did not significantly affect the dependence of field amplification on **A** and electrolyte width as stated above. Therefore, in general, battery designs utilizing a smaller value of **B** will minimize the positive electrode oversizing required to mitigate electrode edge failures.

2.4 Conclusions

Li electrodeposition experiments were performed using single-crystal $Li_6La_3ZrTaO_{12}$ garnet as a model brittle solid electrolyte to investigate the factors that determine Li metal penetration. *In-situ* and *ex-situ* microscopy was performed on cells undergoing galvanostatic electrodeposition at realistically high current densities for practical applications. Li infiltration resulting in short circuits occurred on the minute time scale at current density of 10 mA cm^{-2}. The initiation of Li metal filled cracks occurred predominantly at the perimeter of the working electrode, even when much larger (up to 0.4 mm), intentionally produced surface defects are present nearby. After crack initiation, subsurface crack extension is observed that is consistent with stable crack growth, i.e., without catastrophic fracture.

The crack initiation sites coincide with the locations of maximum electric field at current collector edges. It is concluded that electric field amplification drives Li penetration from sites on the solid electrolyte surface with supercritical surface flaws. Finite element modeling was used to investigate the magnitude of field enhancement as a function of the relative sizes of the positive and negative electrodes, and the thickness-to-width aspect ratio of the cell. It is concluded that the risk of edge effects resulting in Li metal penetration (i.e., during charging of a Li metal battery) is reduced by designing cells to have a larger positive electrode than negative electrode, and a smaller thickness/width ratio.

Chapter 3

Effects of electroplated metal yield stress on critical current density

In this chapter, we show that the pure alkali metals, Li, Na and potassium (K), when mated with solid electrolytes that conduct each respective alkali ion, have CCDs that scale inversely to their mechanical deformation resistance. This trend is observed across solid electrolytes of nearly identical ionic conductivity (~1 mS cm^{-1}) and fracture toughness (~2–3 MPa $m^{0.5}$), and in experiments at a similar plated areal capacity (1.5–3 mAh cm^{-2}).

The contents of this chapter were first published in Ref. [65]. Cole Fincher measured the alkali metal mechanical properties. Andres Badel performed the image analysis of disassembled cells.

3.1 Introduction

The threshold conditions for the extension of a metal filament through a solid electrolyte can be described in terms of either a critical overpotential or current density. Conceptually, both are correlated with the presence of flaws in the solid electrolyte, which are filled with electrodeposited metal when the applied potential produces a flux of metal ions through the solid electrolyte (Figure 3-1). As elaborated by Porz et al. [3], metal-filled defects will propagate through solid electrolytes as a result

of crack-opening stresses generated by the electrodeposition of metal that are high enough to fracture the electrolyte. Li accumulation inside a flaw has an associated increase in volume that produces tensile loading of the flaw, which results in crack propagation when the elastic energy release rate exceeds the fracture resistance of the electrolyte [3]. The electrical overpotential that produces this stress is the critical overpotential, and represents a thermodynamic limit dependant on properties such as the solid electrolyte fracture toughness [3, 34, 53] and the surface flaw size distribution. As in the Griffith–Inglis–Orowan theory of fracture [39, 42, 66], the largest such flaw in the solid electrolyte will have the lowest critical overpotential and tend to propagate first.

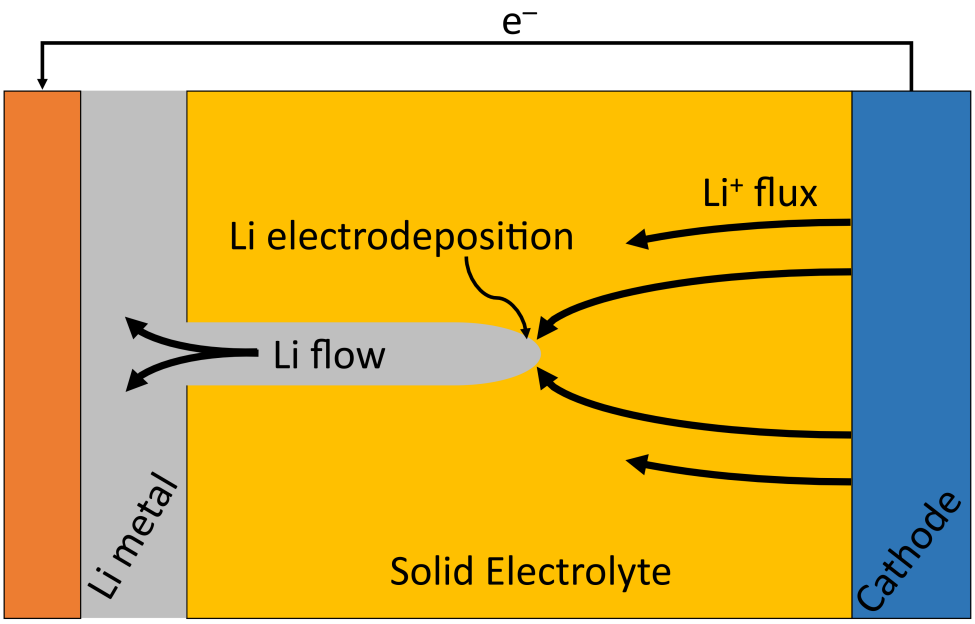

Figure 3-1: Li flux through a solid electrolyte results in electrodeposition at the tip of metal-filled flaws, which readily exceed the critical overpotential [3] for fracture.

However, material transport away from regions of high stress such as the metal filament tip, can relieve the electrodeposition stresses; this is fundamentally the origin of the CCD. As the current density is equivalent to the atomic electrodeposition rate (assuming a 100% Coulombic efficiency), at low enough deposition rates a ductile electrodeposited metal may flow away from electrodeposition sites rapidly enough to allow the crack-tip stresses to remain subcritical. The CCD therefore corresponds

to an electrodeposition rate that exceeds the metal flow rate necessary to maintain a subcritical stress. Prior work with liquid Na electrodes in high-temperature Na–S batteries considered analogous mechanical models, using Poiseuille flow of the liquid metal to relate the stress at the Na-filled crack to the rate of metal extrusion out of the crack set by the applied current density [48, 50]. For solid metals, 'extrusion' from the metal-filled crack requires creep and plastic deformation. At high homologous temperatures, creep imparts an effective viscosity and so the solid metals may behave as an 'incompressible work fluid'. For Li metal, the bulk deformation behaviour was recently characterized in detail [67, 68], although size effects may also come into play at the submicron length scales that are relevant in typical solid electrolytes [54, 67].

The focus of this chapter is to investigate the importance of stress relief at the flaw tip via metal extrusion on determining the onset of metal penetration in solid electolytes. In this vein, the pure alkali metals Li, Na and K were electrodeposited through the solid electrolytes LLZTO, Na-β"-Al_2O_3 (NBA) and K-β"-Al_2O_3 (KBA), respectively. We further conducted microhardness testing experiments on Li, Na and K metals to directly measure the metal's resistance to flow. The three metals in their solid state differ markedly in their mechanical properties, decreasing by over a factor of three in shear modulus (at 300 K) and yield stress (at 80 K) in the order Li →Na →K (refs. [69, 70], Table 3.1). Their liquid-state viscosities when melted also increase in this order [71, 72].

We expect a softer metal to exhibit a higher CCD under equivalent conditions (for example, stack pressure). Na metal possesses a substantially lower yield stress and increased susceptibility to creep than does Li metal at bulk and on small scales [67, 74]. Indeed, recent experiments with Na metal electrodes showed higher (relative to Li metal) room-temperature deposition CCDs of 3.0 mA cm^{-2} at an areal capacity of ~0.5 mA cm^{-2} (with a relatively high applied pressure of 4–12 MPa) (ref. [75]) and as high as 12 mA cm^{-2} at an areal capacity of 0.25 mA cm^{-2} (applied pressure of 3.4 MPa) (ref. [76]). In contrast, Li metal exhibits room-temperature deposition CCDs on the order of 0.1–1 mA cm^{-2} [3, 11, 12, 36–38]. In this chapter we independently reproduce the above trend, and perform analogous measurements on the K system.

Material	Specific capacity (Ah kg^{-1})	Volumetric capacity (Ah L^{-1})	Melting temperature (°C)	Shear modulus at 300°K (GPa) [69]	Yield strength at 300°K (GPa) [70]	Activation energy, power-law creep (kJ mol^{-3}) [73]
Li	3860	2061	180	3.03	27	56.1
Na	1165	1126	98	1.53	7.4	42.2
K	685	582	64	0.661	5.8	40.8

Table 3.1: Electrochemical and mechanical properties of lithium, sodium, and potassium metal.

3.2 Methods

3.2.1 Characterization of solid electrolytes

Polycrystalline LLZTO was obtained from Toshima Manufacturing Inc. and NBA and KBA samples were obtained from Ionotec. All the electrolytes had dimensions of 12.7 mm diameter and ~1 mm thickness. The crystal structure, single crystallinity and phase purity of the electrolytes were determined via X-ray diffraction using a PANalytical X'Pert Pro diffractometer (Malvern Panalytical Ltd).

The ground electrolyte discs (1 mm thickness) received from the vendor were polished using an EcoMe 250 Pro Grinder Polisher (Buehler). To obtain finely polished faces, the samples were then sequentially polished using aqueous diamond suspensions of 9 and 1 µm particle sizes for 25 and 10 min, respectively. The samples were then ultrasonically cleaned in deionized water to remove polishing debris. Stylus profilometry was conducted using a Bruker DXT Stylus Profilometer (Bruker) to quantify the roughness of the polished samples.

Electrochemical impedance spectroscopy was performed on the solid electrolytes using sputtered Au electrodes (blocking Li, Na and K ions) on either side of the solid electrolyte disc using a Bio-Logic VMP-3 cell test system. The Au thin film (~100 nm), which acts as the electrical contact between the ceramic electrolyte disc and the test system, was deposited onto the electrolyte via magnetron sputtering (Cressington). Values for ionic conductivity (and dielectric capacitance) were extrapolated from circuit fitting of the resulting impedance spectra.

A Vickers micro-indenter (LECO LM248AT Microindentation Hardness Testing System) was used to place several indents under enough applied load to produce cracks that emanate from the corners. These cracks have a semicircular crack front that extends normal to the surface into the crystal. By varying the applied load, a range of crack lengths is produced. Indentation loads of 19.6, 9.81 and 4.91 N were used to determine the fracture toughness in this study. The crack lengths were measured via optical microscopy.

Two independent methods (Anstis et al. [4] and Evans and Charles [5]) to obtain

the fracture toughness from indentation data were used. The Anstis method requires a value for Young's modulus of the indented material [4], whereas the Evans method is modulus independent [5].

Thermal etching of the polished solid electrolytes (1 h at 50, 1,000 and 1,000 °C for LLZTO, NBA and KBA, respectively) revealed the grain size to range from 5 to 10 µm for all three solid electrolytes. Scanning electron microscopy imaging of the samples was conducted using a JEOL 6610 LV SEM (JEOL USA Inc.) operated at a 15 kV accelerating potential and 215 pA current. All the samples were prepared in an argon-filled glove box (oxygen and water levels below 0.1 ppm).

3.2.2 Characterization of alkali metals

Li metal rods (Millipore Sigma, item 265969), Na metal bars (Alfa Aesar, item L13285), and K metal lumps (Alfa Aesar, item 13267) were sectioned using a razor blade into pieces approximately 25.4 mm diameter by 19.05 mm thick within an argon-filled glove box. The bottom surface of each sample was rigidly fixed to a 12.7 mm stainless-steel plate using cyanoacrylate adhesive. This assembly was then placed between two well-oiled borosilicate glass plates (6.35 mm thick, lubricated with white mineral oil) inside a hydraulic crimper. Subsequently, the pieces were pressed until flat and covered with a thick (˜3 mm) layer of petroleum jelly. The resulting samples were removed from the glove box and microhardness tests were conducted through the petroleum jelly using a Phase II+ 900-390A microhardness tester. The loading to maximum force (0.245 N) occurred over 15 s. Hardness measurements were calculated as the applied load (0.245 N) divided by the projected contact area.

The Li metal was prepared for the cell assembly by cold rolling to the desired thickness between polyethylene sheets and punching a disc of the desired diameter. The Na and K metal electrodes were melted in a glove box and applied as a liquid to the surfaces of the solid electrolyte discs held at room temperature, whereupon the liquid metals quickly froze.

3.2.3 Electrochemical cell assembly and testing

Prior to assembly, the polished solid electrolyte discs were heat treated in an argon-filled glove box at oxygen and water contents below 0.1 and 0.1 ppm, respectively, which has been shown to remove surface impurity layers on the electrolyte and reduce the interfacial impedance [13]. Polished LLZTO discs were heat treated in the glove box at 500°C for 3h to remove $LiCO_3$ and LiOH (ref. [13]). The NBA and KBA pellets were subjected to heat treatment at 1,000°C for 1 h in the glove box to remove possible chemisorbed moisture.

Li metal symmetric cells were assembled by placing a disc of flat lithium foil (9.53 mm diameter, 0.25 mm thickness, 50 mAh cm^{-2} and ~20 µl Li) between the LLZTO solid electrolyte with a stainless-steel cylinder acting as the current collector on either side. Before the electrochemical cycling, the Li cells were heated to 170°C for 3 h at an applied stack pressure of 1.5 MPa (calibrated independently with a compression force gauge), which reduced the interfacial impedance of the cell. The area-specific interfacial impedance of the cells was measured to be on the order of 25–35 Ω cm^2. For cells cycled under even lower pressure (~75 kPa), the springs in the fixture were compressed to a few percent strain based on visual inspection.

Na and K metal cells were assembled by pipetting a 10 µl drop of molten Na or K onto their respective solid electrolytes and flattening the droplet with the steel current collector (7.14 mm diameter) under an applied stack pressure of 1.5 MPa. No precycling heat treatment was necessary to produce a low impedance cell for testing.

Galvanostatic experiments were conducted on the cells at 22°C using a Bio-Logic VMP-3 cell test system. Li/LLZTO/Li cells were subjected to galvanostatic cycling at nominal current densities (that is, based on the initial electrode areas) from 0.125 to 1.5 mA cm^{-2} using 0.125 mA cm^{-2} increments at nominal areal capacities of 1.5 mA cm^{-2} per cycle (7.5 µm Li plating thickness). Na/NBA/Na and K/KBA/K cells were subjected to galvanostatic cycling at nominal current densities from 0.5 to 8 mA cm^{-2} using 0.5 mA cm^{-2} increments at nominal areal capacities of 3.0 mAh cm^{-2} per cycle (27.4 and 51.5 µm thickness for Na and K, respectively).

Impedance spectra were collected at the start of testing and at set intervals thereafter (after each galvanostatic cycle for Li/LLZTO/Li and after every four cycles for Na/NBA/Na and K/KBA/K cells). Throughout the electrochemical testing, cells remained in an argon-filled glove box with the oxygen and water content below 0.1 and 0.1 ppm, respectively. On completion of the electrochemical cycling, *ex-situ* microscopy was conducted on disassembled cells using a Leica DMS300 (Leica Camera) digital microscope.

3.3 Results and discussion

3.3.1 Mechanical and electrical properties of solid electrolytes

The properties of the solid electrolytes as well as the alkali metal that is electrodeposited affect the CCD. We sought a set of solid electrolytes that allow a direct comparison of behaviour between the three pure metal electrodes across all three working ions (Li^+, Na^+ and K^+). The three solid electrolytes used, LLZTO, NBA and KBA, were each obtained as densely sintered polycrystalline discs and determined by X-ray diffraction to be predominantly composed of the desired ion-conducting crystalline phase (not shown). As described in the *Methods*, these solid electrolytes were processed to a similar smooth surface finish (Figure 3-2 and 3-3). Representative data from the stylus profilometry measurements are shown in Figure 3-4.

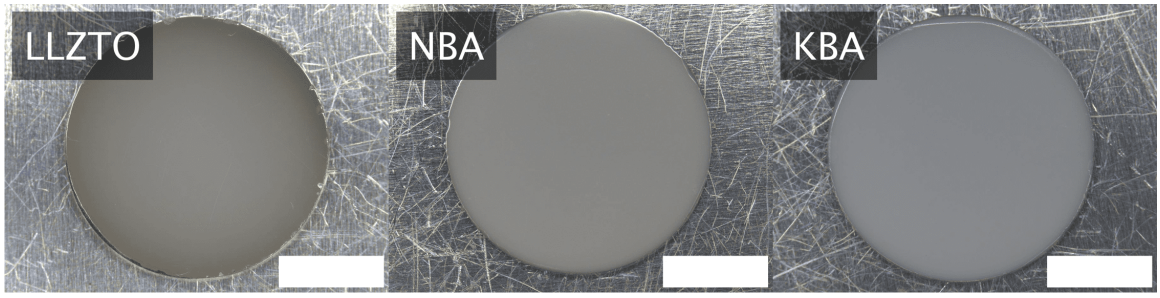

Figure 3-2: Optical microscopy images of polycrystalline solid electrolyte plates polished to 1 µm grit. Left to right: Li^+-, Na^+-, and K^+-conducting solid electrolytes. Scale bars denote 5 µm.

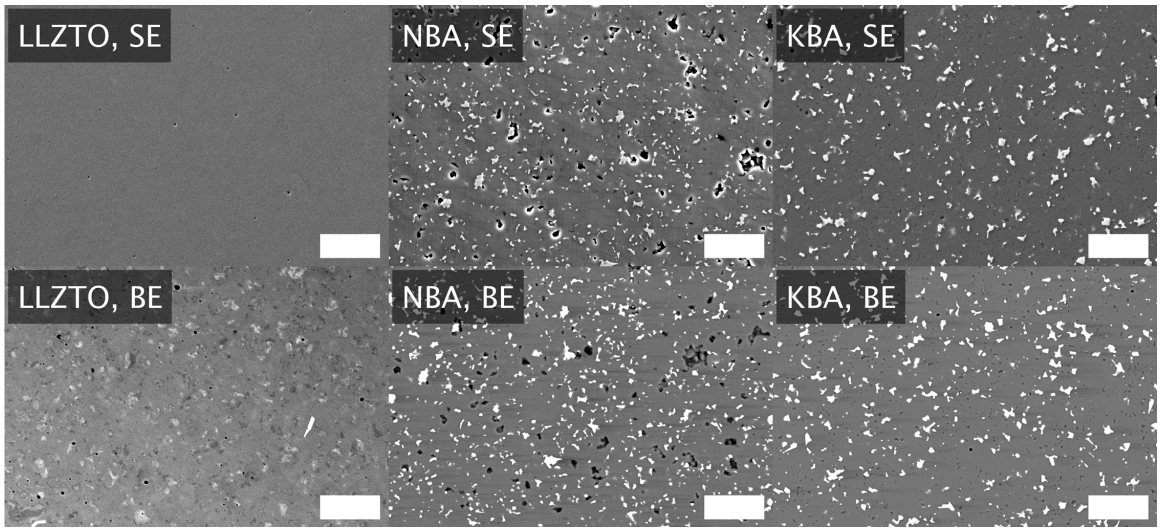

Figure 3-3: Secondary electron images of polycrystalline solid electrolyte plates polished to 1 µm grit. Left to right: Li^+-, Na^+-, and K^+-conducting solid electrolytes. The SEM images are nearly featureless for the polished LLZTO, whereas for the NBA and KBA micrographs we observe a distribution of zirconia (ZrO_2) particles (which appear as white particles in the SEM images) added by the vendor to increase the fracture toughness. SE denotes secondary electron micrographs whilst BE denotes backscattered electron micrographs. Scale bars denote 20 µm.

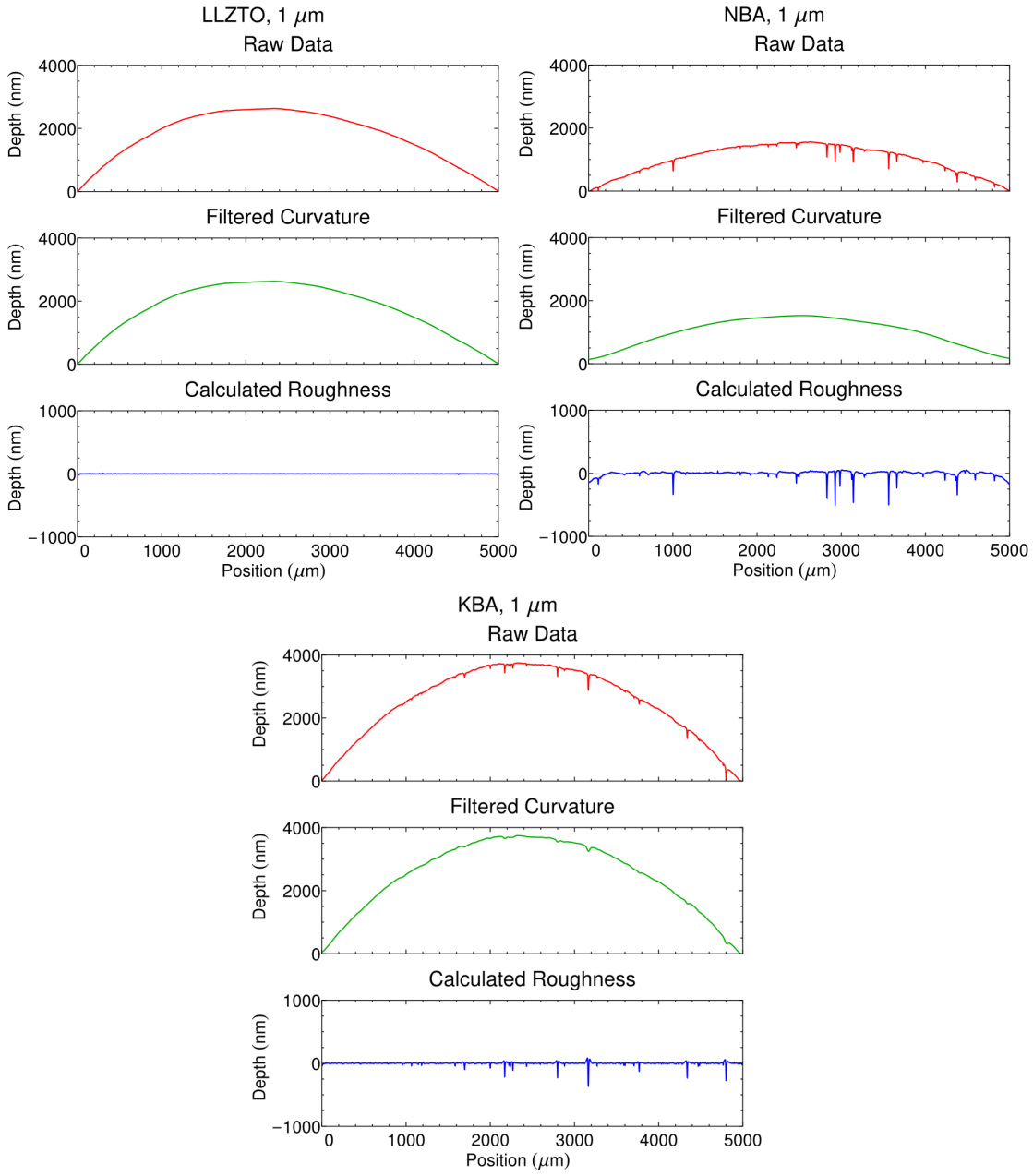

Figure 3-4: Stylus profilometry measurements of polycrystalline solid electrolyte plates polished to 1 µm grit. Although the entire disc was polished (0.5" diameter), the instrument measured over a scan length of 5 mm. The polishing procedure described in the main text results in surfaces that are flat to within 5 µm over 5 mm with sub-micron scale surface flaws resulting from features inherent to the respective microstructures. Over a scan length of 5 mm, we observe that the polished surfaces consistently possess sub-micron surface flaws for all three solid electrolyte samples (N = 3 per electrolyte).

A scanning electron microscopy image of an indent showing the characteristic corner cracks from Vickers microindentation, as well as the corresponding hardness (determined from the square-pyramid indent size) is shown in Figure 3-5 and 3-6. The corresponding fracture toughness (determined from the crack length) of the solid electrolytes are summarized in Figure 3-7. Each of the three solid electrolytes were determined to possess similar fracture toughness values (2–3 MPa $m^{0.5}$). These values are higher than Wolfenstine et al.'s results for 97% dense polycrystalline $Li_{6.28}La_3Zr_2Al_{0.24}O_{12}$ (LLZAO) garnet, 1.14 MPa $m^{0.5}$ [6].

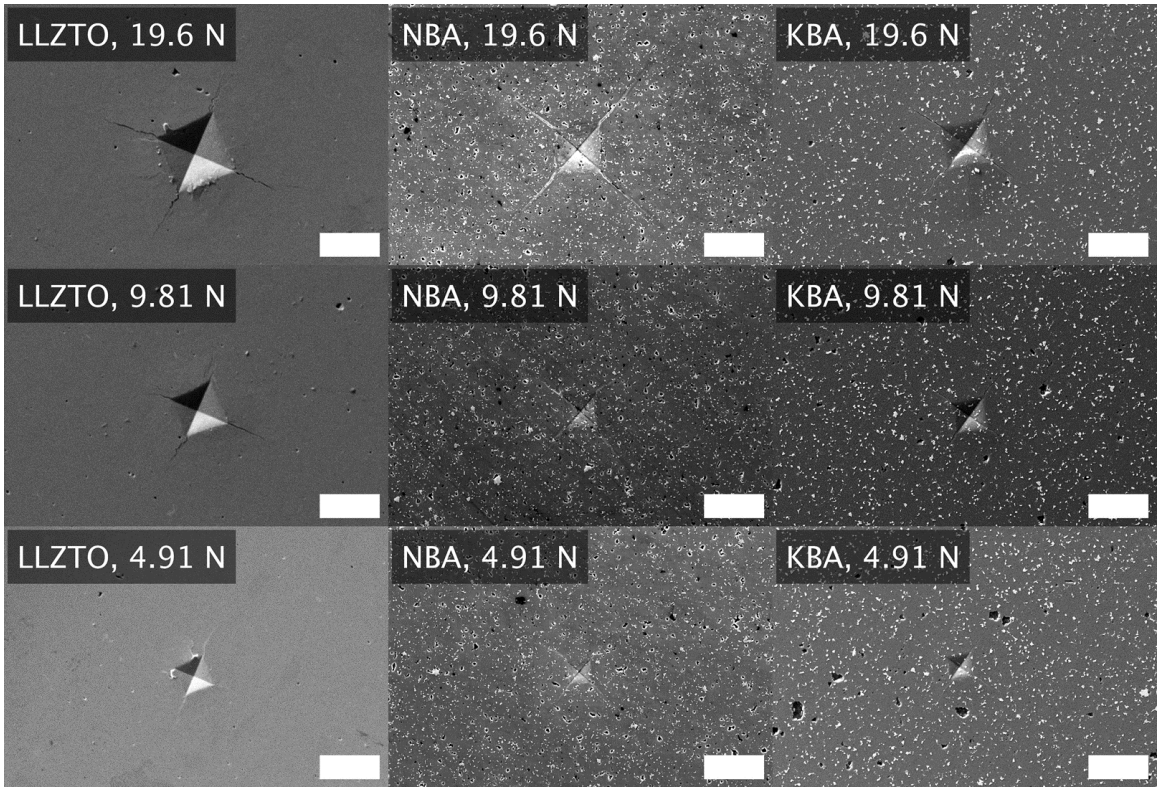

Figure 3-5: SEM images of indented polycrystalline solid electrolyte plates polished to 1 µm grit. Each indent leaves behind a clear diamond impression with sharp edge cracks, allowing the Anstis/Evans methodologies to be applied towards calculating a fracture toughness from crack length measurements (3 indents on 3 independent samples per electrolyte class). Anstis and Evans refer to two commonly accepted methods for evaluating the fracture toughness via Vickers microindentation [4, 5].

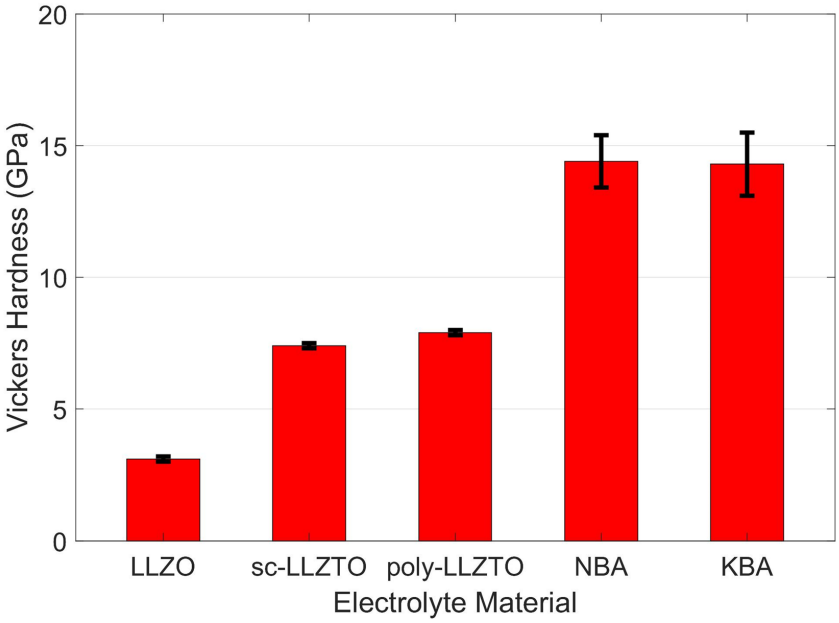

Figure 3-6: Summary of hardness measurements on model solid electrolytes.

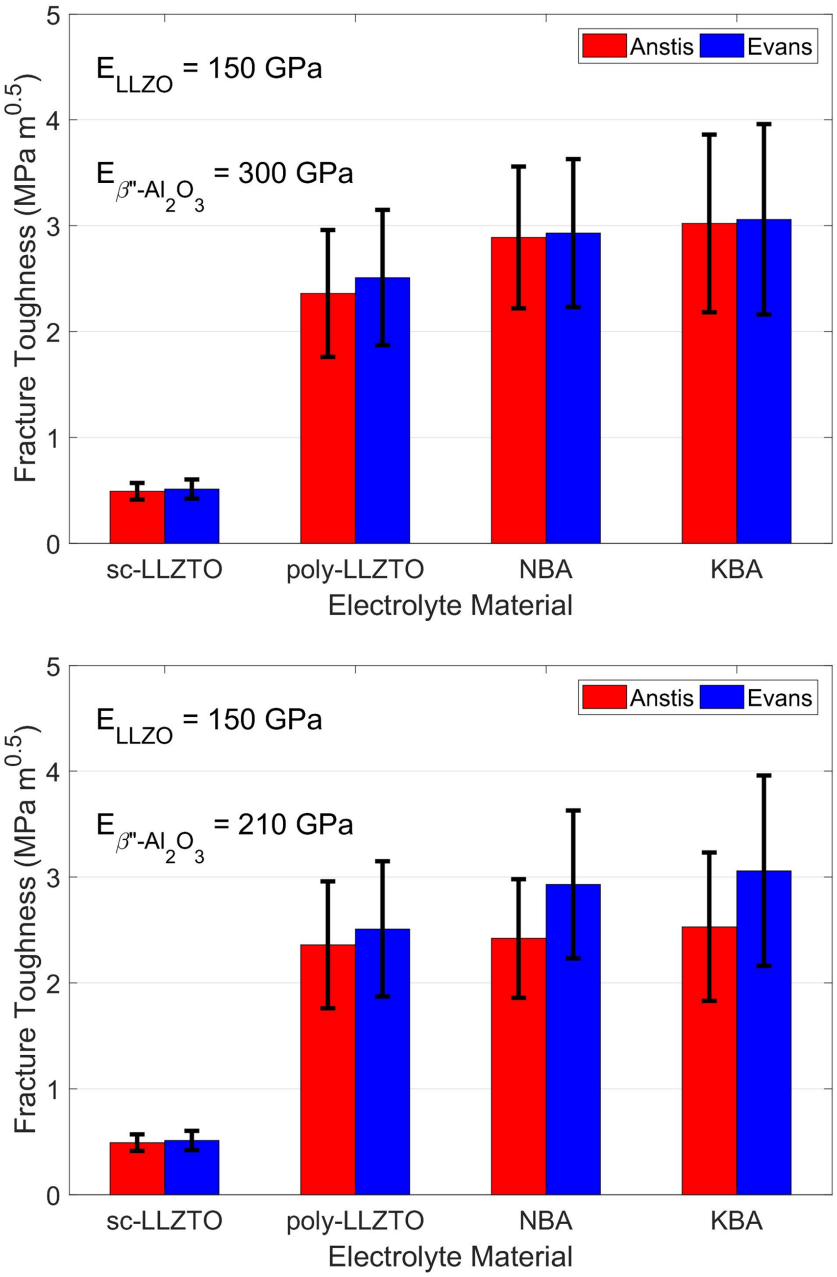

Figure 3-7: Summary of fracture toughness measurements on solid electrolytes based on Vickers microindentation. The fracture toughness of LLZTO, NBA, and KBA were measured to be 2.51±0.64 MPa $m^{0.5}$, 2.9±0.70 MPa $m^{0.5}$, and 3.06±0.90 MPa $m^{0.5}$. The Young's modulus for LLZTO is taken to be 150 GPa as measured previously [6], while that for NBA and KBA is given a lower and upper bound of 210 GPa and 300 GPa based on previous measurements on undoped β"-Al_2O_3 [7, 8]. (top) depicts calculated fracture toughnesses based on a lower bound for the elastic modulus of β"-Al_2O_3, whilst (bottom) depicts values for a corresponding upper bound. These bounding values do affect the calculated fracture toughness within the Anstis method.

Electrochemical impedance spectroscopy measurements performed on the solid electrolytes to determine the ionic conducitivty are shown in Figure 3-8. All three solid electrolytes exhibited similar ionic conductivities on the order of 1–2 mS cm^{-1}. Equivalent circuit parameters used to fit the data are shown in Table 3.2.

3.3.2 Mechanical deformation resistance of alkali metals

The hardness, determined from the square-pyramid indent size, of the alkali metals investigated in this study are summarized in Figure 3-9. The equivalent yield stress, which is taken as one-third the hardness for ductile metals [9], decreased in the order Li (1.74 MPa) to Na (0.41 MPa) to K (0.24 MPa).

3.3.3 Critical current density measurements

For each combination of metal electrode and solid electrolyte, the CCD was measured in a symmetric cell of the configuration in Figure 3-10 by reversibly plating the metal in both directions at stepwise increasing galvanostatic currents until the current and potential drop across the cell indicated the onset of a short circuit (Figure 3-11). Impedance spectroscopy was used to further confirm the short circuit (Figure 3-11).

Figure 3-12 summarizes all of the critical current density measurements over the relevant areal capacities (1.5-3 mAh cm^{-2}) performed in this study as listed in Table 3.3. Each datum in Figure 3-12 represents one critical current density measurement derived from a single cell. The room-temperature CCDs for Na metal and K metal are clearly higher than that for Li metal, as both reach maximum values of ~3 mA cm^{-2} versus < 1 mA cm^{-2} for Li. The vertical lines at 1 mAh cm^{-2} and 3 mAh cm^{-2} in Figure 3-12 represent, respectively, a minimum areal capacity for practical application, and a typical areal capacity for current Li-ion technology. The horizontal lines at 1 mA cm^{-2} and 3 mA cm^{-2} in Figure 3-12 represent CCD values that correspond to a 1C rate capability at those areal capacities. We focused on areal capacities in the range 1–3 mAh cm^{-2} because results at a lower areal capacity may not be relevant to high energy density batteries. For example, a high cycling stability has been observed

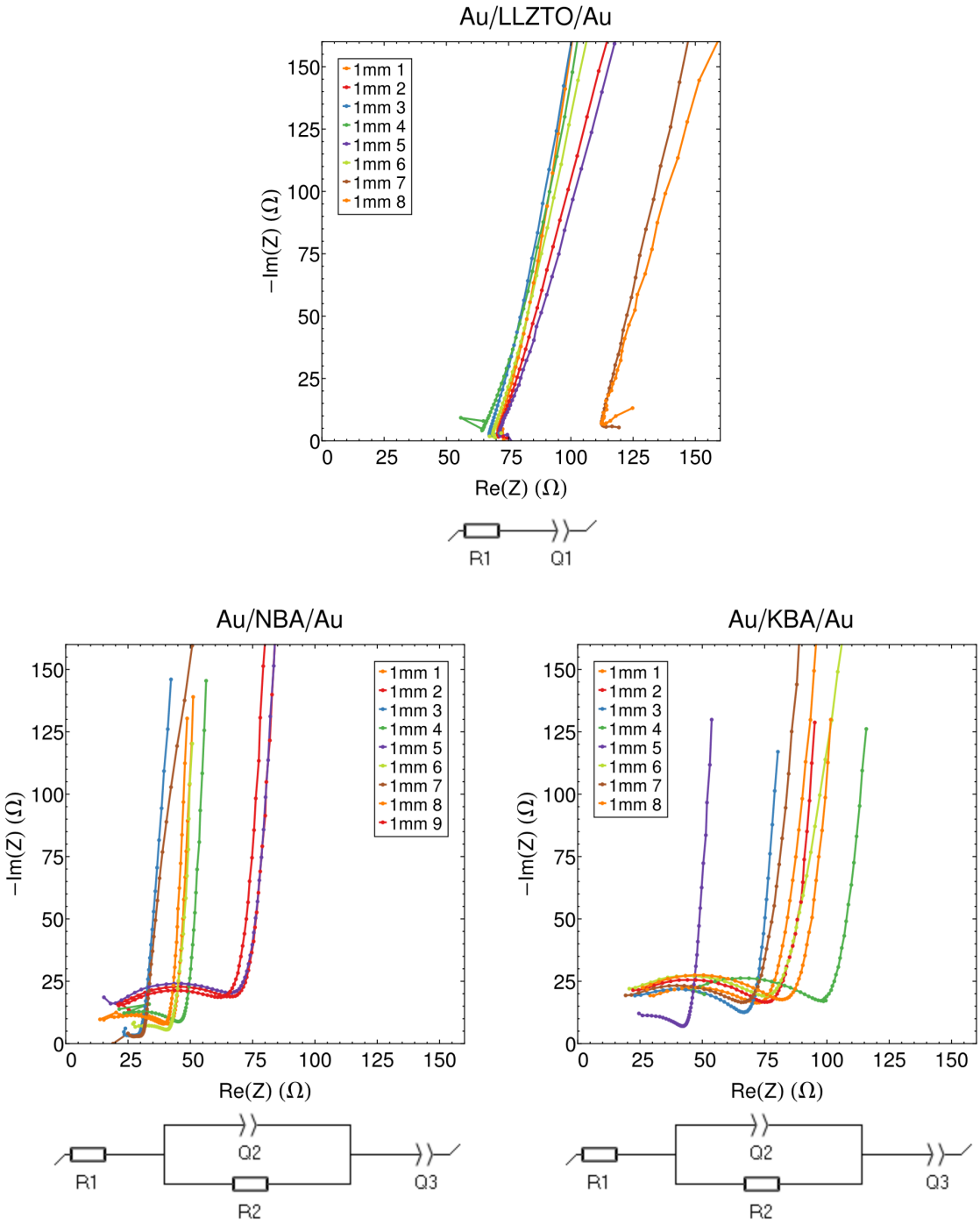

Figure 3-8: Electrochemical impedance spectra results for SSEs used in this study: LLZTO, NBA, and KBA. The bottom insets are schematics of the equivalent circuit used to fit the data. Each SSE used in this study exhibits similar DC ionic conductivities on the order of 1 mS cm^{-1}. The ionic conductivity of $Li_{6.75}La_3Zr_{1.75}Ta_{0.25}O_{12}$, Na-β"-$Al_2O_3$, and K-β"-$Al_2O_3$ were measured to be 1.03±0.2 mS cm^{-1}, 1.72±0.56 mS cm^{-1} and 1.07±0.3 mS cm^{-1}

LLZTO		NBA		KBA	
R1 (Ω)	79.7 $\pm$19	R1 (Ω)	14.6 $\pm$5.6	R1 (Ω)	10.4 $\pm$7.3
Q1 (10^{-7} Fs^{a-1})	7 $\pm$4	R2 (Ω)	35.8 $\pm$2 0.1	R2 (Ω)	66.6 $\pm$15
		Q2 (10^{-7} Fs^{a-1})	6.8 $\pm$1.2	Q2 (10^{-7} Fs^{a-1})	2.3 $\pm$0.4
		Q3 (10^{-7} Fs^{a-1})	15 $\pm$4.9	Q3 (10^{-7} Fs^{a-1})	23.5 $\pm$3.4
		C_{Na} (10^{-9} F)	17 $\pm$14	C_K (10^{-9} F)	7.4 $\pm$3.7
σ_{Li} (mS cm^{-1})	1.03$\pm$0.2	σ_{Na} (mS cm^{-1})	1.72$\pm$0.56	σ_K (mS cm^{-1})	1.07$\pm$0.3

Table 3.2: Equivalent circuit parameters of solid state electrolytes considered in this study.

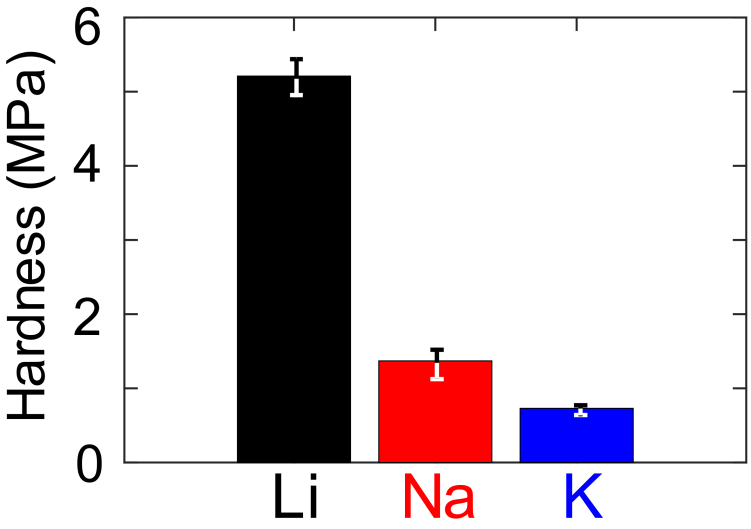

Figure 3-9: Hardness values for bulk Li, Na, and K metal. Each bar represents the average of 10 tests, with the error bar representing the standard deviation.

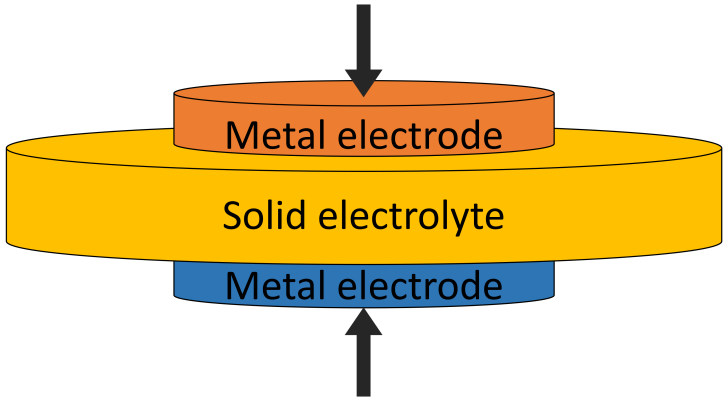

Figure 3-10: Schematic of symmetric cell configuration for CCD measurements.

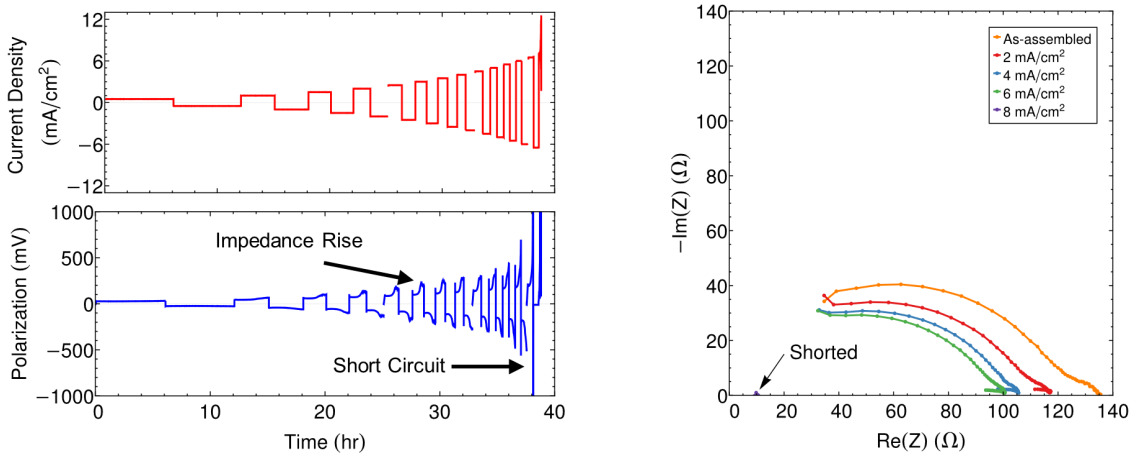

Figure 3-11: Typical current density versus time sequence (top left) and corresponding potential profile (bottom left), here for a K/KBA/K symmetric cell reversibly plating 3 mAh cm^{-2} of K metal. The onset of cell failure, which serves as the measurement of the CCD, is indicated by the arrow. The onset of an electrical short circuit is detected as a voltage drop across the cell. (right) Nyquist plot for the same cell. The curves that connect the individual data points act as guides for the eye. The curves correspond to the impedance spectra taken after cycling the cell at the particular current density shown in the key. The presence of the capacitive arcs indicates the absence of a short circuit. A short circuit is confirmed by the collapse of the spectrum to a point, as indicated by the arrow.

in solid-state thin-film batteries [77], in which areal capacities are over a factor of five lower than those in bulk batteries. Recent studies for Na metal in contact with NBA reported higher CCDs than we measured here, but at lower areal capacities: 3 mA cm^{-2} at 0.5 mAh cm^{-2} (ref. [75]) and 12 mA cm^{-2} at 0.25 mAh cm^{-2} areal capacities [76]. We are not aware of prior results for K metal. The areal capacities employed here are also several times higher than those in prior work using bulk Li metal foil electrodes [10–17].

Note that results in Figure 3-12 show a variation in areal capacity even between nominally identical experiments. This is because both the CCD and areal capacity shown are true values based on the final measured area of the metal electrodes in the disassembled cell, which exhibits some variability, rather than on the areas of the current collectors or starting electrodes. The ratio of the original and final size of the Li disc is on the order of 1, which indicates a negligible change in the size of the Li disc during cycling. We attribute this minimal expansion of the Li disc to a combination of the higher hardness of the Li metal compared to Na and K, and frictional forces between the Li disc and SSE interface. The aspect ratio of the discs is high, which results in frictional forces that reduce the actual deviatoric stress imposed on the metal discs. This explains why the Li metal electrode did not expand significantly despite an applied stress that is nominally greater than the yield stress (~0.5 MPa). In contrast, the Na and K discs exhibited much greater area increases during cycling. We speculate that the frictional forces between the Na (or K) disc and SSE interface were insufficient to inhibit yielding under the applied stack pressure due to the lower hardness of Na and K. We also expect a distribution of CCDs to be observed in these experiments, in large part because the short-circuit event is correlated with the failure of a brittle solid. It is widely accepted that brittle materials exhibit a wide distribution of measured strengths (which is normally treated with Weibull statistics) due to the existence of the distribution of defect types and sizes. Fracture is inherently stochastic as it is the largest flaw in the distribution to cause failure. Similarly, it is not surprising that measured CCD values should exhibit a range of values if failure propagates from defects and inhomogeneities at the metal–solid electrolyte interface,

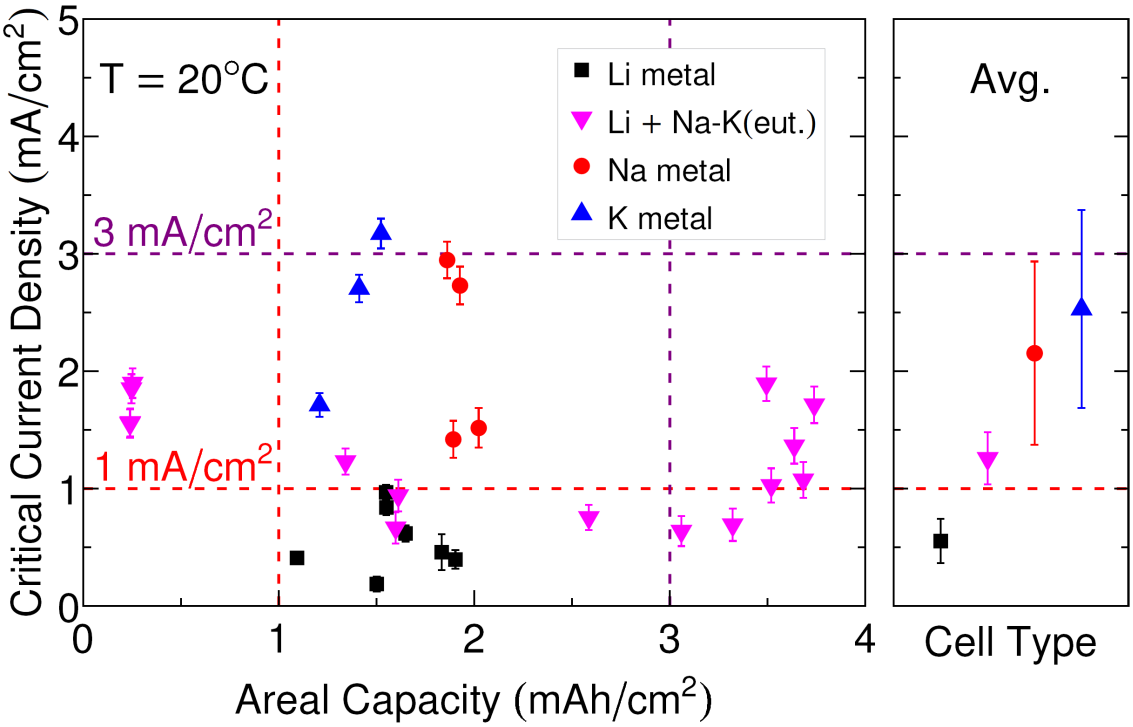

Figure 3-12: (left) CCDs for single-phase solid Li, Na and K metal in symmetric cells using the solid electrolytes LLZTO, NBA and KBA, and a 0.68K–0.32Na (by mole) eutectic liquid (eut) at the interface between Li metal foil and LLZTO. The magenta data points (incorporating the 0.68K–0.32Na eutectic liquid) are discussed in the next chapter of this thesis. All the experiments were conducted at 20°C under a nominal stack pressure of ~1.5 MPa, except for circled points, which are from experiments conducted at ~75 kPa. Each datum represents an independent cell measurement. The total span of the vertical error bars in the leftmost plot represents the variation in CCD for a single increment by which the current density was stepped in the galvanostatic protocol. (right) Average CCD value for each metal or alloy, which includes results across all areal capacities tested. The vertical error bars on the rightmost plot represent 95% confidence intervals for the CCD according to the sample set.

Symmetric cell type	No. of samples, applied stack pressure	Mean CCD (mA cm^{-2})	σ CCD (mA cm^{-2})	Mean ACF	σ ACF
Li/LLZTO/Li	7 at 1.5MPa	0.502	0.295	1.11	0.22
Na/NBA/Na	4 at 1.5MPa	2.15	0.800	1.56	0.0622
K/KBA/K	3 at 1.5MPa	2.53	0.743	2.19	0.236

Table 3.3: Symmetric cells studied in this work. The abbreviations CCD and ACF denote "Critical Current Density" and "Area Correction Factor", respectively, whilst σ denotes the sample standard deviation. The ACF is the measured ratio between the initially assumed electrode area and the true contact area between the electrode and solid electrolyte as determined by post mortem image analysis.

or even below the surface. Note that the electrode area (~1 cm^2) is many orders of magnitude larger than the scale of the microstructure (tens of square micrometres; Figure 3-3), which ensures that a range of flaws will be tested. We nonetheless observed a higher average CCD as well as a higher peak CCD for the Na and K metals compared to the Li metal.

Figure 3-3 and Figure 3-4 show that the LLZTO and KBA solid electrolytes have less residual porosity than the NBA electrolyte. The NBA and KBA electrolytes, which come from the same supplier, both contain a small amount of ZrO_2 precipitates acting as a toughening additive. Solid precipitates do not provide any obvious sites for metal deposition. In the case of the NBA electrolyte, while more pores are visible, these pores are largely spherical in shape rather than being of sharp-crack or dendritic morphology and are also unlikely to be critical flaws that grow to failure. The flaws that propagate as metal filaments probably originate elsewhere, as Swamy et al. [53] found to be the case for polished single crystals of LLZTO.

After cycling to failure, each cell was disassembled for examination. A representative example of data (polarization curves and post-mortem microscopy) for each of the Li, Na, and K electrodes appear in Figures 3-13, 3-14 and 3-15, respectively. As mentioned, we observed that the alkali metal electrode increases in area during cell assembly due to spreading upon compression of the cell stack, and potentially also during electrochemical cycling, especially in the cases of the Na and K symmetric cells. These optical images (Figures 3-13, 3-14, and 3-15) show the condition after cycling of the metal electrodes on the surfaces of the current collector (left panels) and the solid electrolyte (right panels) at both the positive and negative terminals of the symmetric cells. The alkali metals and the electrolytes are labelled. These images show that the true contact area between the metal electrode and the solid electrolyte (panels labelled "Electrolyte Surface") is greater than the area of the initial Li electrode, or the raised portion of the current collector that initially compresses the Na and K electrodes. The current density and areal capacity during each experiment was calculated on the basis of the final electrode area, measured directly from the disassembled cells after cycling to failure. This methodology gives accurate current

densities and areal capacities at the point of short-circuit failure but may underestimate the values at earlier cycles of testing where the electrode area is smaller.

In some instances (Figure 3-14), dark cracks were observed in the solid electrolyte that appear to be metal filled, likely indicating a location of crack propagation. Due to field concentration effects at electrode edges elucidated in prior work, [53] crack initiation near electrode edges may be favored. In most experiments, exemplified by Figure 3-15 for K metal electrodes, the site of short-circuit failure was not visible and is assumed to lie under the electrodes. For the K metal cells, a fringe of darkened regions is seen at the edges of the metal electrode contact area (Figure 3-15, right panels). These were found through successive polishing of the KBA to extend below the surface. This darkening appears to result from chemical reduction of the KBA when in contact with K metal, rather than indicating the presence of metal dendrites, since contact of K metal with the KBA in the absence of cycling was also observed to result in darkening. Where Li metal was used, a faint gold discoloration was seen after exposure. This is attributed to trace amounts of water and oxygen present in the inert Ar glovebox atmosphere, confirmed by XPS measurements showing the presence of elemental oxygen on the metal surface (data not shown).

Figures 3-13, 3-14 and 3-15 show that the polarization curves remain relatively flat (constant interfacial impedance) for most cells during a given half-cycle at intermediate current rates, indicating a relatively stable stripping/plating process in which the interface resistance does not change significantly over time. An exception to this behavior is seen for the K metal electrodes, see Figure 3-11 and 3-15, where an increase in polarization during a constant current step is visible. This difference in behavior suggests an increase in interfacial resistance for the K metal cells, which we speculate may be related to the larger molar volume of K metal compared to Li and Na. At an areal capacity of 1.5 mAh cm^{-2}, the thickness of reversibly plated metal is 7.5µm for lithium, 15µm for sodium, and 25µm for potassium. The larger volume change for potassium metal may lead to greater void formation or delamination of the metal electrode from the solid electrolyte, causing impedance growth, as suggested by Kasemchainan et al. [78]

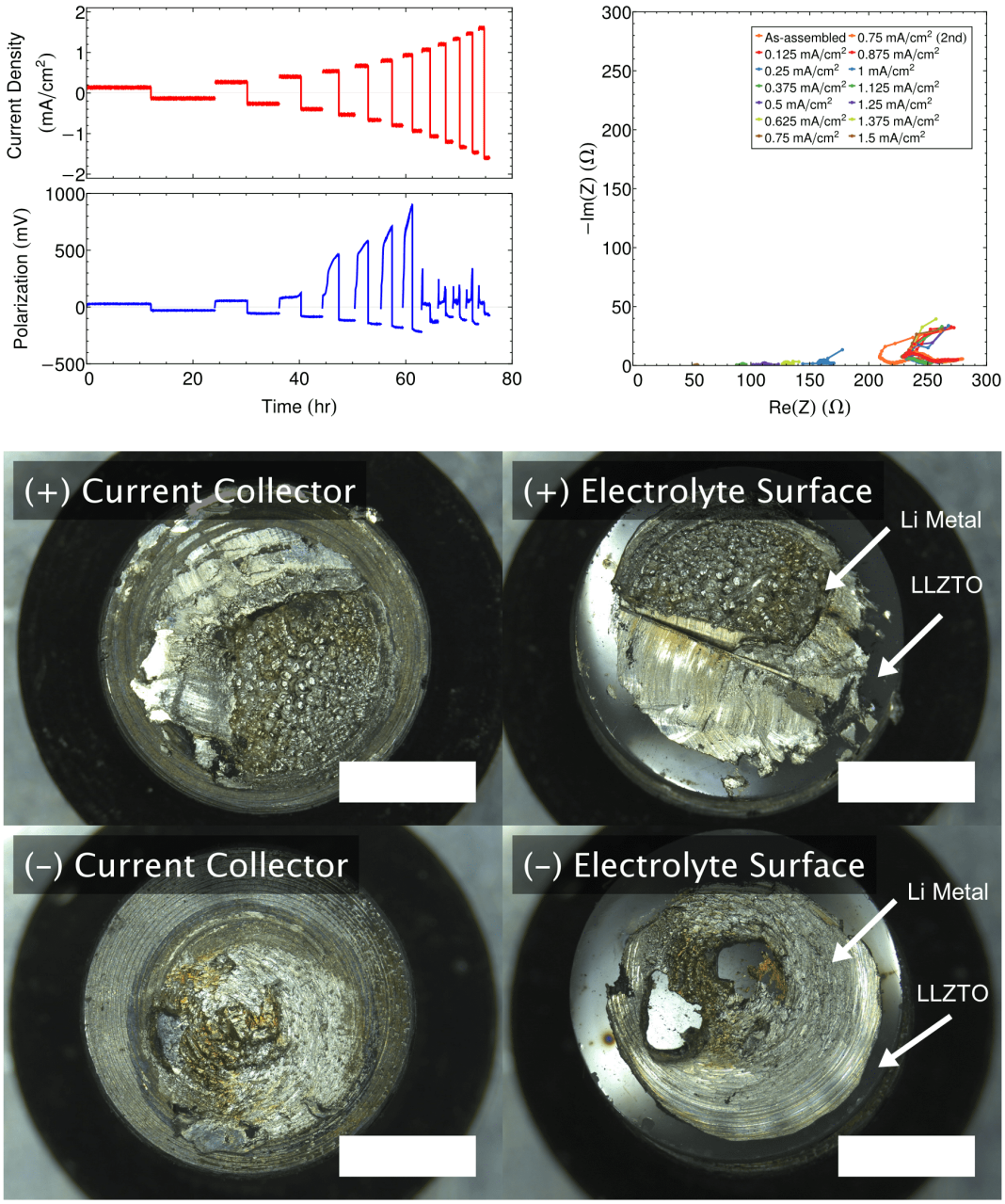

Figure 3-13: Galvanostatic cycling results for a symmetric Li/LLZTO/Li cell at room temperature. (top left) The current density is increased stepwise while plating a constant 1.5 mAh cm^{-2} (based on the initial assumed area) capacity in both polarities. The corresponding cell polarization shows a sudden drop at 0.875–1.0 mA cm^{-2} corresponding to the formation of a short circuit (corresponding to a true critical current density of 0.968±0.06 mA cm^{-2}). (top right) IS spectra taken after each cycle show a disappearance of the arc, corresponding to interfacial capacitance, once the short circuit forms. (bottom) Optical digital microscopy images of the current collector and electrolyte interface of the Li/LLZTO/Li cell post failure and disassembly. Scale bars denote 5 mm.

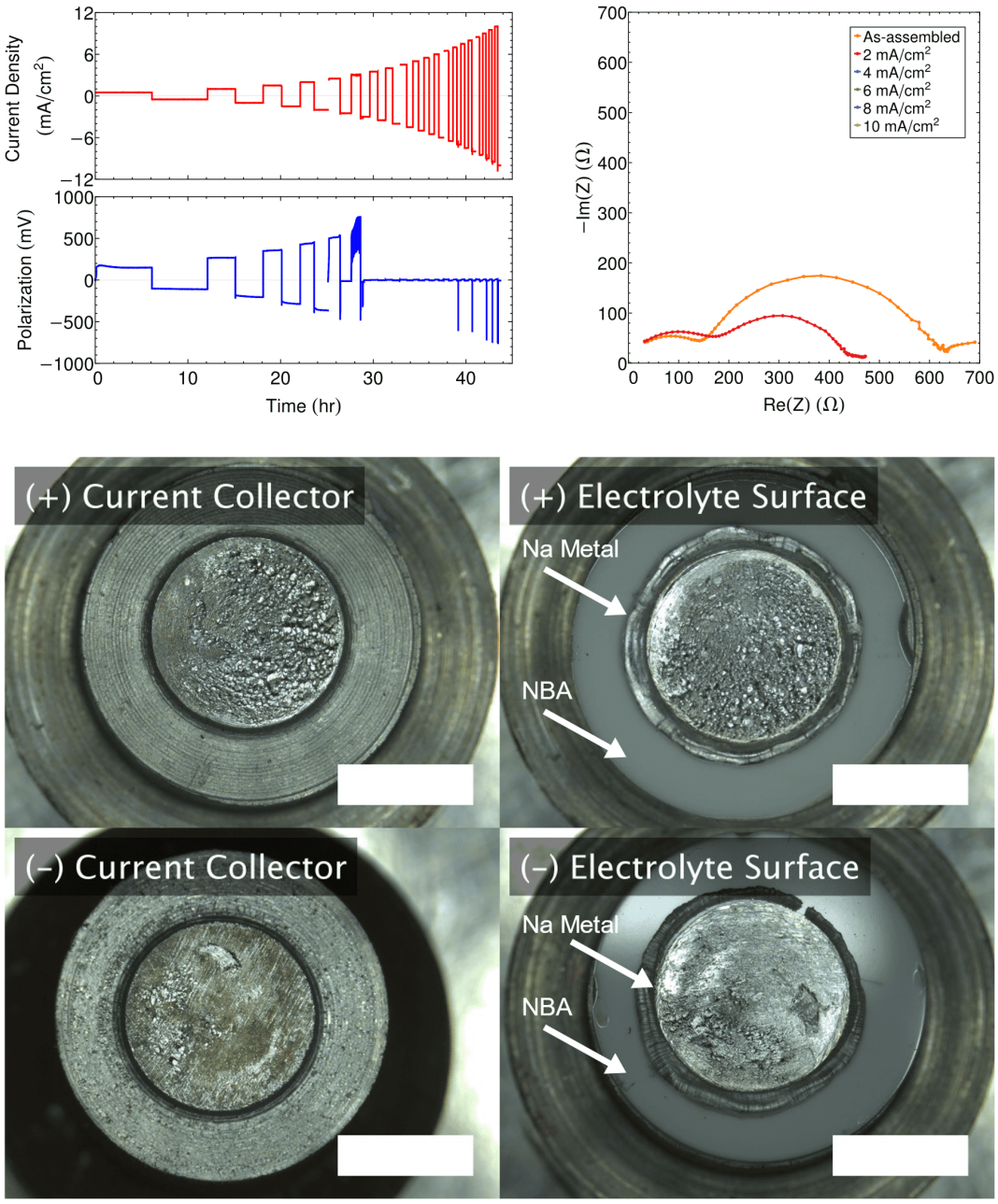

Figure 3-14: Galvanostatic cycling results for a symmetric Na/NBA/Na cell at room temperature. (top left) The current density is increased stepwise while plating a constant 3 mAh cm^{-2} (based on the initial assumed area) capacity in both polarities. The corresponding cell polarization shows a sudden drop at 2–2.5 mA cm^{-2} corresponding to the formation of a short circuit (corresponding to a true critical current density of 1.45±0.16 mA cm^{-2}). (top right) IS spectra taken after each cycle show a disappearance of the arc, corresponding to interfacial capacitance, once the short circuit forms. (bottom) Optical digital microscopy images of the current collector and electrolyte interface of the Na/NBA/Na cell post failure and disassembly. Scale bars denote 5 mm.

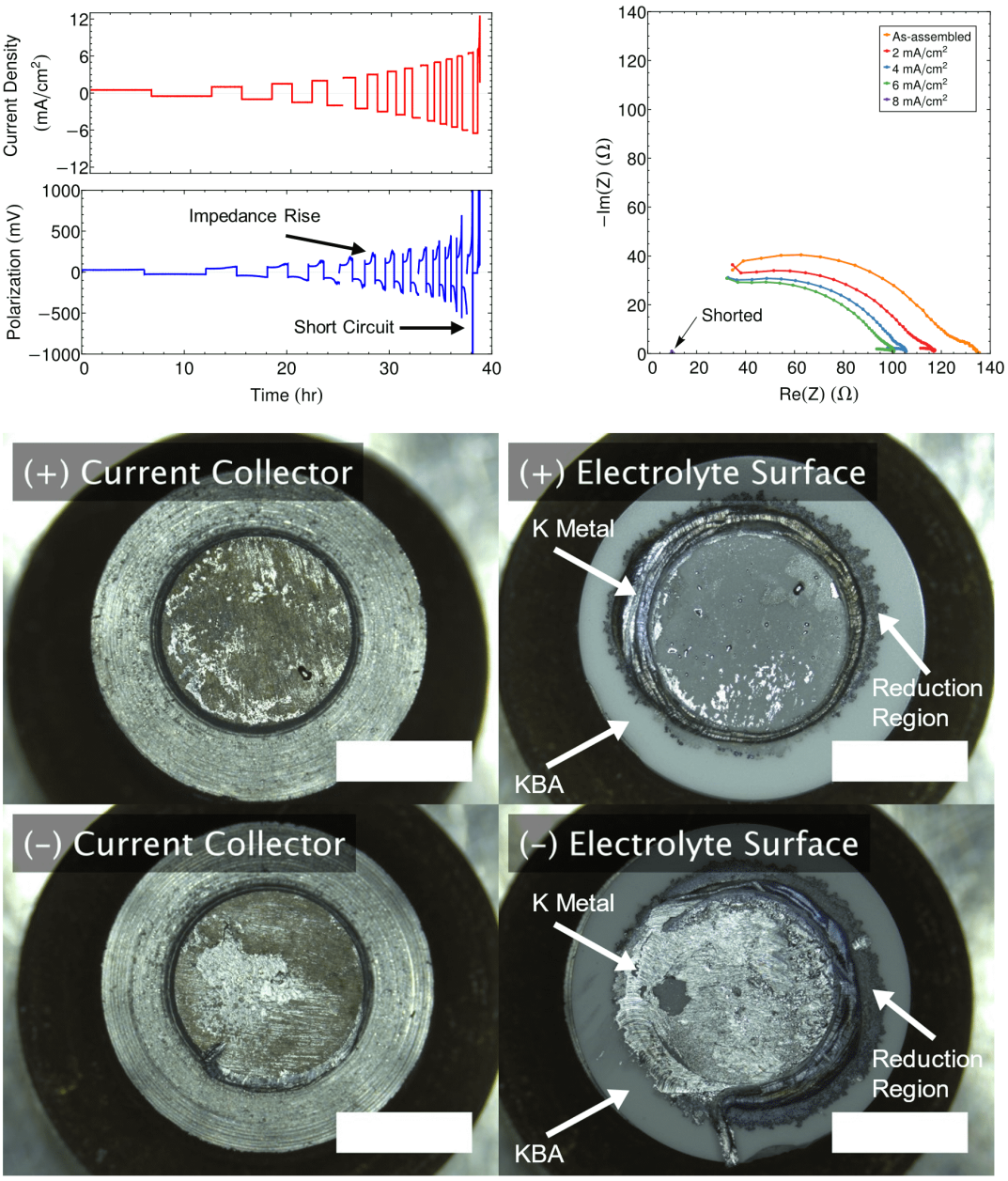

Figure 3-15: Galvanostatic cycling results for a symmetric K/KBA/K cell at room temperature. (top left) The current density is increased stepwise while plating a constant 3 mAh cm^{-2} (based on the initial assumed area) capacity in both polarities. The corresponding cell polarization shows a sudden drop at 6–6.5 mA cm^{-2} corresponding to the formation of a short circuit (corresponding to a true critical current density of 3.02±0.12 mA cm^{-2}). (top right) IS spectra taken after each cycle show a disappearance of the arc, corresponding to interfacial capacitance, once the short circuit forms. (bottom) Optical digital microscopy images of the current collector and electrolyte interface of the K/KBA/K cell post failure and disassembly. Scale bars denote 5 mm.

3.4 Conclusions

Having measured the CCD as well as the equivalent yield stress of each metal, we are able to show that there is an approximately linear relationship between the two (Figure 3-16). This trend is observed across solid electrolytes of nearly identical ionic conductivity (~1 mS cm^{-1}) and fracture toughness (~2–3 MPa $m^{0.5}$), and in experiments at a similar plated areal capacity (1.5–3 mAh cm^{-2}). This result is consistent with the flow-based model discussed previously, in which the CCD is limited by the Poiseuille flow of the metal out of stress-concentrating flaws. These results for the three solid metals also establish a baseline behaviour for comparison with the results for semi-solid electrodes, reported in the following chapter.

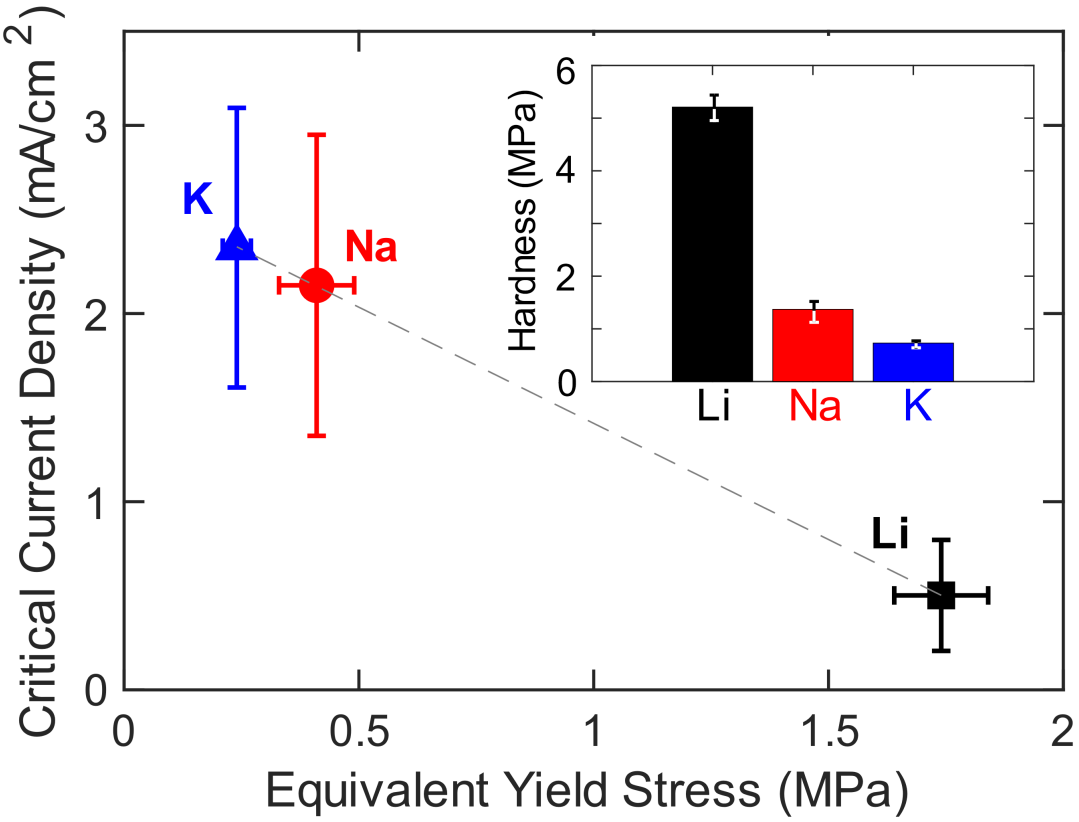

Figure 3-16: CCD versus equivalent yield stress (defined as hardness/3 (ref. [9]) for solid Li, Na and K metal. The grey line serves as a guide for the eye. Inset: hardness for bulk Li, Na and K metal. Each bar represents the average of ten tests, and the error bar represents the standard deviation. These results indicate that the equivalent yield stress decreases in the order Li (1.74±0.1 MPa) to Na (0.41±0.08 MPa) to K (0.24±0.03 MPa). The vertical error bars represent 95% confidence intervals for the CCD according to the sample set. The horizontal error bars represent the standard deviation of the measured values.

Chapter 4

Semi-solid electrodes enabling high critical current densities

In this chapter, we demonstrate two electrode architectures in which the presence of a liquid phase enables high current densities while it preserves the shape retention and packaging advantages of solid electrodes. First, biphasic Na–K alloys show K^+ critical current densities (with the K–β"–Al_2O_3 electrolyte) that exceed 15 mA cm^{-2}. Second, introducing a wetting interfacial film of Na–K liquid between Li metal and $Li_{6.75}La_3Zr_{1.75}Ta_{0.25}O_{12}$ solid electrolyte doubles the critical current density and permits cycling at areal capacities that exceed 3.5 mA cm^{-2}. These design approaches hold promise for overcoming electrochemomechanical stability issues that have heretofore limited the performance of solid-state metal batteries.

The contents of this chapter were first published in Ref. [65]. Chris Eschler measured the alkali metal wetting angles. Andres Badel performed the image analysis of disassembled cells. Pinwen Guan calculated the Li–Na–K ternary phase diagram.

4.1 Introduction

Several recent studies focused on use of room-temperature liquid metal electrodes, obtained from deep eutectics in Na–K (ref. [79]), Na–Cs (ref. [80]) and Ga–In (ref. [81]). A limitation of fully liquid electrodes is that the corresponding electrochemical cells

must be designed around containment of the low-viscosity liquid metal, as in the case of high–temperature sodium–sulfur batteries, in which closed-ended ceramic electrolyte tubes are typically used. Such designs may be costly or impractical, especially for compact high-energy battery packs in which a large number of series-connected cells are needed to reach the design voltage. Our approach, instead, aims to use semi-solid mixtures which, include a liquid phase in which the working alkali metal is soluble. The liquid phase provides a fast transport path for the working ion as well as flow at the microscale, which enables a high CCD, whereas the solid phase provides structural rigidity and is a source of the working ion.

In the following examples, the semi-solid electrodes have the consistency of a paste and can be assembled into a free-standing cell without specialized liquid-electrode containment. We demonstrate that biphasic Na–K alloys, paired with a K-β"-Al_2O_3 (KBA) solid electrolyte, can be cycled between liquid-rich and solid-rich end states at CCDs several times higher than those achievable with the solid-state alkali metals. Furthermore, the high areal capacities at which such behaviour is realized suggests 'self-healing' of electrodeposition-induced defects at the metal–solid electrolyte interface. Na–K alloys permit cycling at a CCD that exceeds 15 mA cm^{-2}, the highest room-temperature value reported to date for a metal electrode on a solid electrolyte, and sufficient to enable 3C cycling at a typical Li-ion electrode area capacity (that is, 3 mAh cm^{-2}).

Given that Li-ion technology is more well-developed than Na-ion or K-ion technologies, we also considered semi-solid anode design possibilities in which Li is the working ion. In the Li–Na and Li–K binary systems, the equilibrium liquid fields do not extend all the way to room temperature (see phase diagrams in Figures 4-1 and 4-2, method of calculation given in *Methods*), so room-temperature semi-solid electrodes are not available. In contrast, the Na–K eutectic at 260.5 °K (Figure 4-3) indicates at least a limiting composition (0.32Na–0.68K, by mole) in which a room-temperature liquid can be accessed. Thus, an electrode design in which a thin Na–K liquid film is used in conjunction with a solid Li metal electrode was conceived.

By introducing a small amount of Na–K liquid at the interface between a Li metal

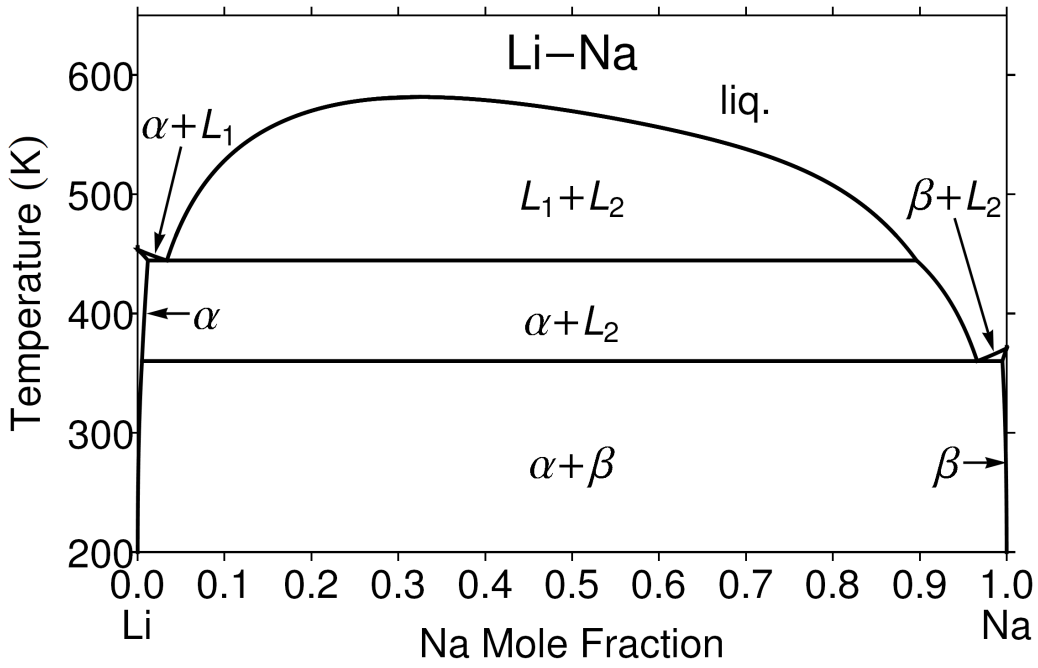

Figure 4-1: Calculated Li-Na phase diagram.

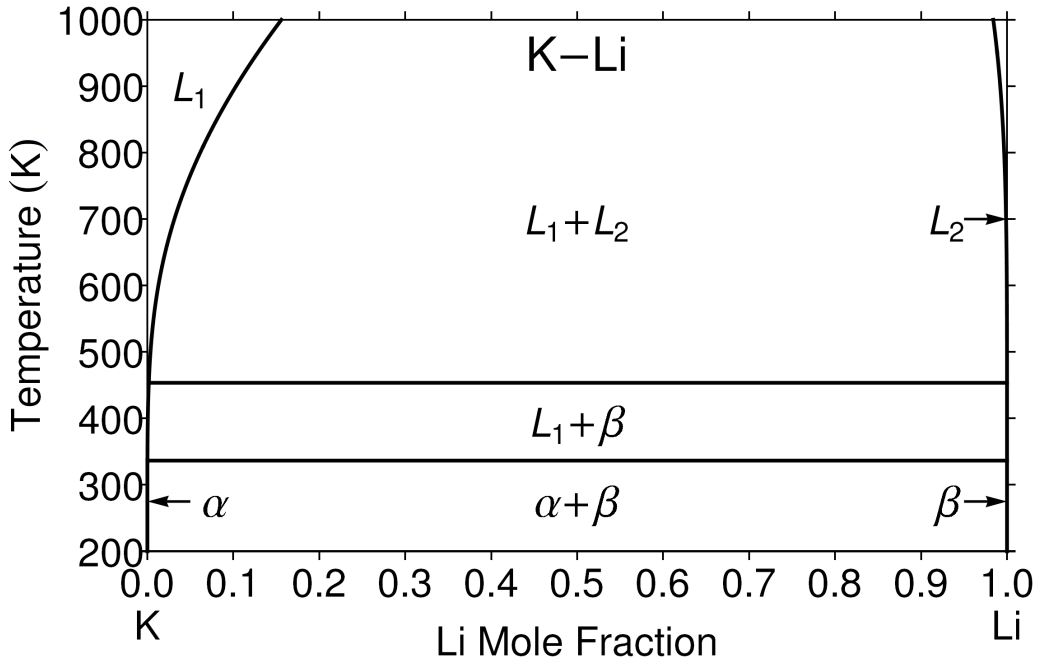

Figure 4-2: Calculated K-Li phase diagram.

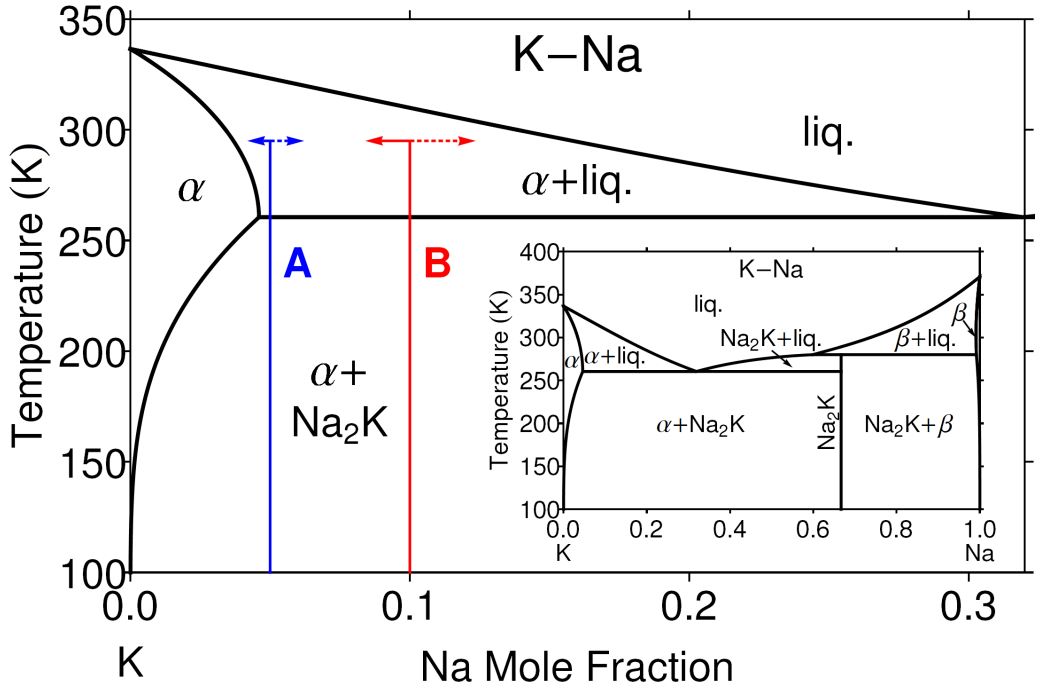

Figure 4-3: K-rich end of the computed Na–K binary phase diagram. Inset: full phase diagram. Compositions A (0.95K-0.05Na) and B (0.90K-0.10Na) are shown by the vertical blue and red lines, respectively. The horizontal arrows that point to the left and right show the composition change in each electrode of this symmetric cell design on cycling to a 3 mAh cm^{-2} areal capacity. For composition A, the calculated initial and terminal liquid phase percentages in the two electrodes of the symmetric cell are 3.8 mol% and 20 mol%, respectively, whereas for composition B they are 38 mol% and 70 mol%, respectively.

electrode and $Li_{6.75}La_3Zr_{1.75}Ta_{0.25}O_{12}$ (LLZTO) solid electrolyte, we show that the CCD more than doubles with cycling at practical areal capacities $>$ 3 mAh cm^{-2}, which suggests that degradation by void formation in solid metal electrodes [78] can be mitigated with a thin metallic liquid film.

In this chapter, symmetric electrochemical cells of the configuration in Figure 3-10 were used to measure the CCD at room temperature of various distinct combinations of metal electrodes and solid electrolytes. Including results from the previous chapter, the cells fall within three categories, as depicted in Figure 4-4: first, solid Li, Na and K electrodes paired with their respective ion-conducting solid electrolytes, second, semi-solid Na–K electrodes paired with a K ion conducting solid electrolyte and, third, a Li metal solid electrolyte with a thin interfacial film of Na–K liquid, paired with the LLZTO solid electrolyte.

4.2 Methods

4.2.1 Electrochemical cell assembly and cycling

Na–K alloys were prepared by melting the pure Na and K, pipetting by volume into a glass vial in the desired ratio of metals, homogenizing by heating into a single-phase liquid regime and cooling. Prior to assembly, the solid electrolyte discs were polished and heat treated in the manner described in Section 3.2.

Na-K alloy cells were assembled by pipetting a 10 µl drop of premixed liquid Na–K alloy onto the K–β"–Al_2O_3 electrolyte and flattening the droplet with the steel current collector (7.14 mm diameter) under an applied stack pressure of 1.5 MPa. No precycling heat treatment was necessary to produce a low impedance cell for testing. The capacity of the electrode and its composition change during cycling was computed on the basis of the starting electrode volume and the areal capacity reached during cycling, assuming a linear rule of mixtures for the densities of the Na–K alloys.

Li metal cells that incorporate the eutectic Na–K alloy layer were assembled in a similar manner to those of the plain Li cells described in Section 3.2 by adding ~5 µl

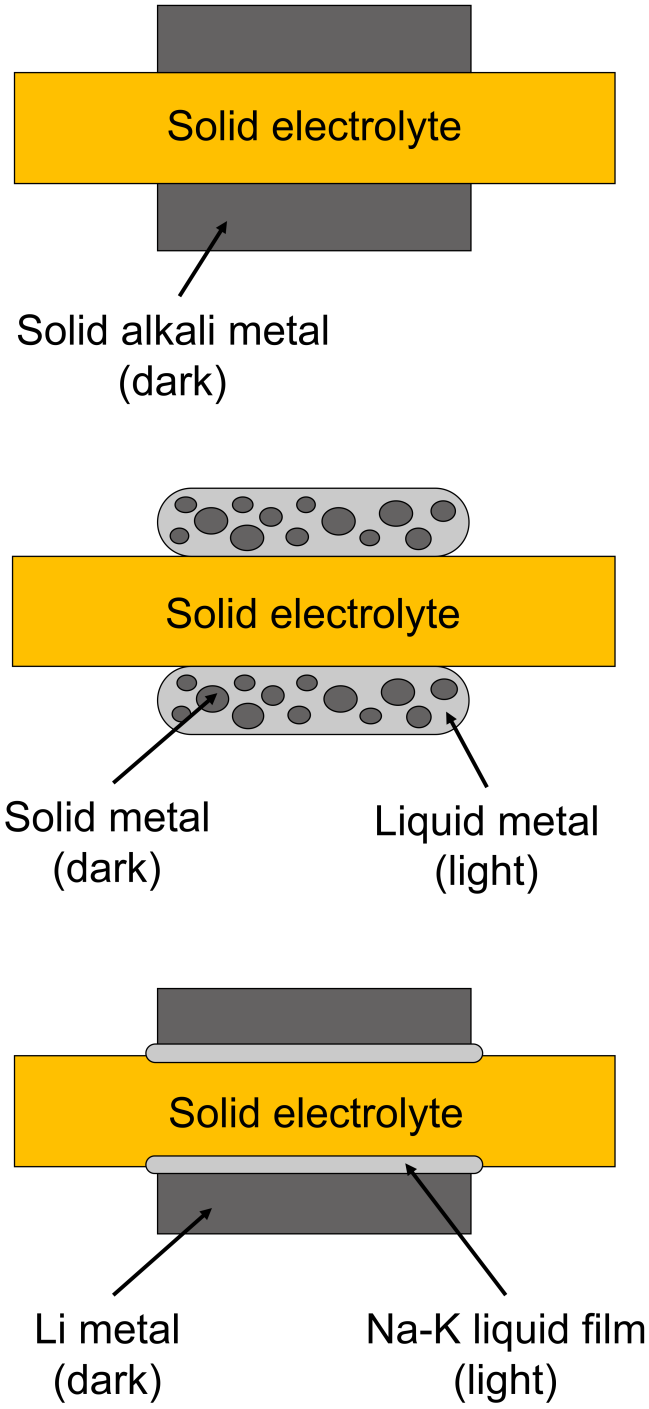

Figure 4-4: Graphical schematic summarizing the three families: (top) all-solid, (center) semi-solid, and (bottom) solid with an interfacial liquid of electrode materials investigated in Chapters 3 and 4 of this thesis.

of eutectic Na–K alloy (68 mol% K) to one face of the punched Li disc. The side of the Li disc with the added Na–K alloy was placed in contact with the LLZTO solid electrolyte disc. For some of the cells in which a Li metal electrode was used with an interfacial layer of Na–K eutectic liquid, the stack pressure was reduced to a low value of ~75 kPa.

Galvanostatic experiments were conducted on the cells at 22°C using a Bio-Logic VMP-3 cell test system. 0.95K–0.05Na/KBA/0.95K–0.05Na and 0.90K–0.10Na/KBA /0.90K–0.10Na cells were subjected to galvanostatic cycling at nominal current densities (that is, based on the initial electrode areas) from 0.5 to 40 mA cm^{-2} using 0.5 mA cm^{-2} increments at nominal areal capacities of 3.0 mAh cm^{-2} per cycle (51.5 µm thickness of K, respectively). NaK(eut.)-Li/LLZTO/NaK(eut.)-Li cells were subjected to galvanostatic cycling at nominal current densities from 0.25 to 3.0 mA cm^{-2} using 0.25 mA cm^{-2} increments at nominal areal capacities of 0.25, 1.5 or 3 mAh cm^{-2} per cycle (1.25, 7.5 or 15 µm Li plating thickness, respectively). This was done to investigate the areal capacity dependence of CCD and to compare present results with literature. The notation 0.95K-0.05Na and 0.90K-0.10Na denote binary alloy electrodes of 95 and 90 mol% K respectively, whilst Li-NaK(eut.) denotes a Li electrode with a thin coating (~5 µL) of Na-K alloy at the eutectic composition (68 mol% K, 32 mol% Na).

Impedance spectra were collected at the start of testing and at set intervals thereafter (after each galvanostatic cycle for NaK(eut.)–Li/LLZTO/NaK(eut.)–Li cells, and after every four cycles for 0.95K–0.05Na/KBA/0.95K–0.05Na and 0.90K–0.10Na/ KBA/0.90K–0.10Na cells). Throughout testing, cells remained in an argon-filled glove box with the oxygen and water content below 0.1 and 0.1 ppm, respectively. On completion of electrochemical cycling, *ex-situ* microscopy was conducted on disassembled cells using a Leica DMS300 (Leica Camera) digital microscope.

We also attempted electrochemical cycling of Na^+ from Na–K through NBA. However, we observed that NBA disintegrated immediately in the presence of K and Na–K. This finding is consistent with the work of Baclig et al. [79], who demonstrated that NBA is chemically unstable to K metal.

4.2.2 Calculation of phase diagrams and microstructures

The binary phase diagrams for the Li–Na, Li–K and Na–K systems and the ternary isothermal section of Li–Na–K were calculated using Thermo-Calc software based on the thermodynamic model constructed by the CALPHAD (calculation of phase diagram) modelling approach, in which thermochemical data and phase equilibrium information are used to evaluate the optimal set of parameters that describe the Gibbs energy of each individual phase in a thermodynamic system [82]. The gas phase is described by an ideal substitutional model, with the Gibbs energies of all the constituents taken from the Scientific Group Thermodata Europe database [83]. The molar Gibbs energies of the liquid phase and the three solid-solution phases (face-centred cubic, BCC and hexagonal close packed) that consists of n components are described by:

$$G_{\mathrm{m}}^{\varphi} = \sum_{i=1}^{n} x_{A_i}^{\varphi} G_{A_i}^{\varphi} + RT \sum_{i=1}^{n} x_{A_i}^{\varphi} ln x_{A_i}^{\varphi} + \Delta G^{\varphi} \tag{4.1}$$

here φ represents a solution phase that includes elements $\{A_i | 1 \leq i \leq n, i \in \mathbb{N}\}$, $x_{A_i}^{\varphi}$ the molar fraction of A_i in φ, $G_{A_i}^{\varphi}$ the molar Gibbs energy of pure A_i in the structure of φ, R the gas constant, T the temperature and the excess Gibbs energy, which is expanded as (up to ternary interactions):

$$\Delta G^{\varphi} = \sum\nolimits_{i<j} x_{A_i}^{\varphi} x_{A_j}^{\varphi} I_{A_i,A_j} + \sum_{i<j<k} x_{A_i}^{\varphi} x_{A_j}^{\varphi} x_{A_k}^{\varphi} I_{A_i,A_j,A_k} \tag{4.2}$$

where the binary interaction I_{A_i,A_j} can be expressed in the Redlich–Kister polynomial [84]:

$$I_{A_i,A_j} = \sum\nolimits_{k=0} {}^{k}L_{A_i,A_j} \left(x_{A_i}^{\varphi} - x_{A_j}^{\varphi} \right)^k \tag{4.3}$$

where the coefficient ${}^{k}L_{A_i,A_j} = {}^{k}X_{A_i,A_j} + {}^{k}Y_{A_i,A_j} T$ describes the non-ideal interaction between A_i and A_j, with ${}^{k}X_{A_i,A_j}$ and ${}^{k}Y_{A_i,A_j}$ as the model parameters. The ternary interaction I_{A_i,A_j,A_k} can be written as [85]:

$$I_{A_i,A_j,A_k} = \nu_{A_i}\,{}^{A_i}L_{A_i,A_j,A_k} + \nu_{A_j}\,{}^{A_j}L_{A_i,A_j,A_k} + \nu_{A_k}\,{}^{A_k}L_{A_i,A_j,A_k} \tag{4.4}$$

where ${}^{A_i}L_{A_i,A_j,A_k}$, ${}^{A_j}L_{A_i,A_j,A_k}$ and ${}^{A_k}L_{A_i,A_j,A_k}$ are model parameters, and the following definitions are used:

$$\nu_{A_i} = x^{\varphi}_{A_i} + \frac{1 - x^{\varphi}_{A_i} - x^{\varphi}_{A_j} - x^{\varphi}_{A_k}}{3} \tag{4.5}$$

$$\nu_{A_j} = x^{\varphi}_{A_j} + \frac{1 - x^{\varphi}_{A_i} - x^{\varphi}_{A_j} - x^{\varphi}_{A_k}}{3} \tag{4.6}$$

$$\nu_{A_k} = x^{\varphi}_{A_k} + \frac{1 - x^{\varphi}_{A_i} - x^{\varphi}_{A_j} - x^{\varphi}_{A_k}}{3} \tag{4.7}$$

In this work, the Gibbs energies of pure elements are taken from the Scientific Group Thermodata Europe database [83], and the interaction parameters of the solution phases, as well as the Gibbs energy of the only stable intermetallic compound Na2K, is adopted from the work of Zhang [86].

The microstructure insets in Figure 6a were computed with a time-cone method algorithm [31]. All the nuclei were placed at time = 0 with locations obtained from a uniform random distribution, but with a minimum separation between each nucleus. Each nucleus was given a growth speed chosen from a random distribution from 0.6 to 1.5. The areal density of the nuclei and the time slice of the cones determined the final phase fractions, which were established by pixel counting. The time slices for the phase fractions 0.51 and 0.10 were obtained by a secant-search algorithm.

4.2.3 Sessile drop measurements for alkali metals

Sessile drop measurements were performed to determine the wetting properties of each anode composition on LLZTO, NBA, and KBA. Inside an argon-filled glovebox, a disk of the substrate of interest (prepared by polishing as discussed in *Methods*) and a glass vial containing the metal to be tested were heated on a hotplate. The temperature was adjusted to be a multiple of 20°C slightly above the melting point

of the metal alloy to be tested (Li: 180°C, Na: 120°C, Na-K(eut.): 40°C, K: 80°C). A 10-µL sample of the molten alloy was drawn from a pipette and immediately deposited onto the center of the substrate disk. The system was allowed to equilibrate at temperature for 5 minutes while a Leica DMS300 digital microscope (Leica Camera, Wetzlar, Germany) was positioned horizontally in-plane, facing the droplet and vertically aligned to the top face of the substrate disk. The substrate and drop were covered by a small dome of magnesia ceramic to isolate the testing area from air currents. The local temperature of the drop was measured with a thermocouple and, once it had stabilized, a photograph was taken of the drop's profile. After each photograph, the hotplate temperature was increased by an increment of 20°C, the droplet's temperature was allowed to stabilize for 4 minutes after the hotplate indicated that it had reached the desired temperature, and an image was captured. This procedure was repeated for a total of eight data points for each sample.

4.3 Results and discussion

4.3.1 Critical current density measurements

We present results from 38 symmetric electrochemical cells of the configuration in Figure 3-10 that were used to measure the CCD at room temperature of six distinct combinations of metal electrodes and solid electrolytes (including results from the previous chapter). The cells fall within three categories, as depicted in Figure 4-4: first, solid Li, Na and K electrodes paired with their respective ion-conducting solid electrolytes, second, semi-solid Na–K electrodes paired with a K ion conducting solid electrolyte and, third, a Li metal solid electrolyte with a thin interfacial film of Na–K liquid, paired with the LLZTO solid electrolyte.

Figures 4-5 and 4-6 summarizes all of the critical current density measurements over the relevant areal capacities (1.5-3 mAh cm^{-2}) performed in this study as listed in Table 4.1. Each datum in Figure 4-5 represents one critical current density measurement derived from a single cell. These cells are tabulated in Table 4.1. All reported

final areal capacities and critical current densities were corrected for the change in electrode area during cycling as in the previoous chapter. The room-temperature CCDs for the biphasic Na-K alloys and the Li-NaK composite electrode are clearly higher than that for Li metal, as both reach maximum values of ~15 mA cm^{-2} (composition of 90K-10Na) and ~2 mA cm^{-2} respectively versus < 1 mA cm^{-2} for Li. These results are discussed in detail in the following sections.

4.3.2 Biphasic semi-solid electrode design

In Figure 4-3, composition A has a starting composition of 0.95K–0.05Na (by mole) and becomes enriched in K on charging in a K-ion cell design in which the cathode supplies the working K^+ and is assembled in the discharged state. Cycling to an areal capacity of 3 mAh cm^{-2} (which corresponds to an electrode thickness change of ~51.5 µm) causes a composition swing in the Na–K electrode, as indicated by the left-pointing blue arrow in Figure 4-3. At the end of the half-cycle, the Na–K electrode composition terminates as a mixture that is mostly the K-rich solid phase α, mixed with a small amount of liquid (3.8 mol%). (This is for the starting electrode of ~10 µl total volume and ~150 µm thickness (*Methods*).) Composition B has a higher Na starting composition of 0.90K–0.10Na (by mole) and behaves similarly, except that it has a higher liquid fraction throughout, which terminates the half-cycle (left-pointing red arrow) with the same two phases, but ten times as much Na–K liquid (38 mol%). During cycling, the electrode is depleted or enriched in the working metal depending on the direction of current flow. Our experimental design for the Na-K electrodes uses two different starting Na/K ratios, and a pre-determined change in electrode composition during cycling, that causes the metal electrode composition to remain within the solid-liquid two-phase fields in the Na-K binary phase diagram, see Figure 4-3. As the overall composition of the electrode changes during cycling, the compositions of the liquid and solid phases in the semi-solid electrode do not since two-phase coexistence is maintained. Only the relative amounts of each phase changes during cycling (i.e., the binary lever rule applies). Therefore, the compositions of the solid and liquid phase in contact at the electrode-electrolyte interface each remain

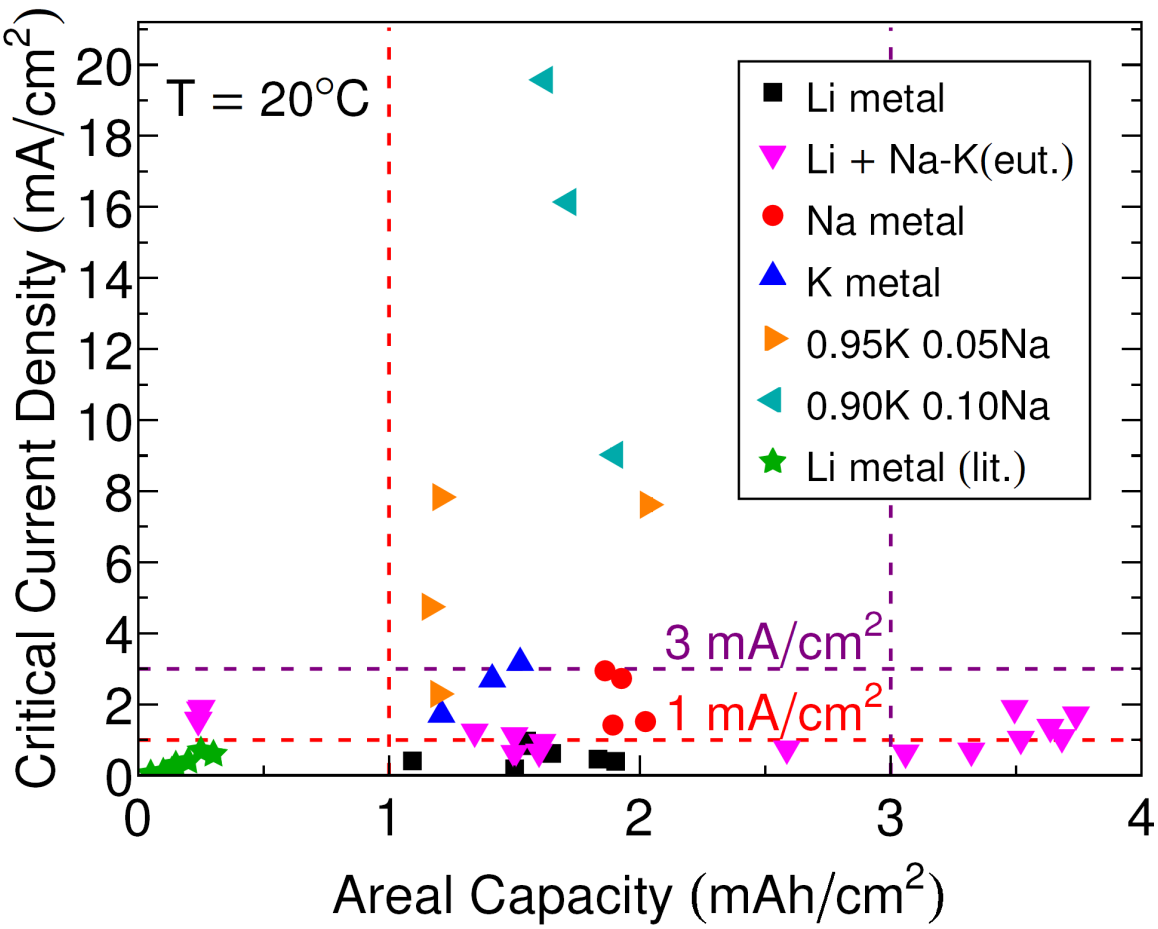

Figure 4-5: CCDs for all the metal electrodes measured, which include 0.95K-0.05Na (by mole) and 0.90K-0.10Na (by mole) semi-solid alloys, as well as CCDs for single-phase solid Li, Na and K metal in symmetric cells using the solid electrolytes LLZTO, NBA and KBA, and a 0.68K–0.32Na (by mole) eutectic liquid (eut) at the interface between Li metal foil and LLZTO. All the experiments were conducted at 20°C under a nominal stack pressure of ~1.5 MPa, except for circled points, which are from experiments conducted at ~75 kPa. Each datum represents an independent cell measurement. The vertical error bars for each data point are not visible as the marker size exceeds the span of the bars in the given axis scale. "lit" refers to comparable data points for Li metal in the literature [10–17].

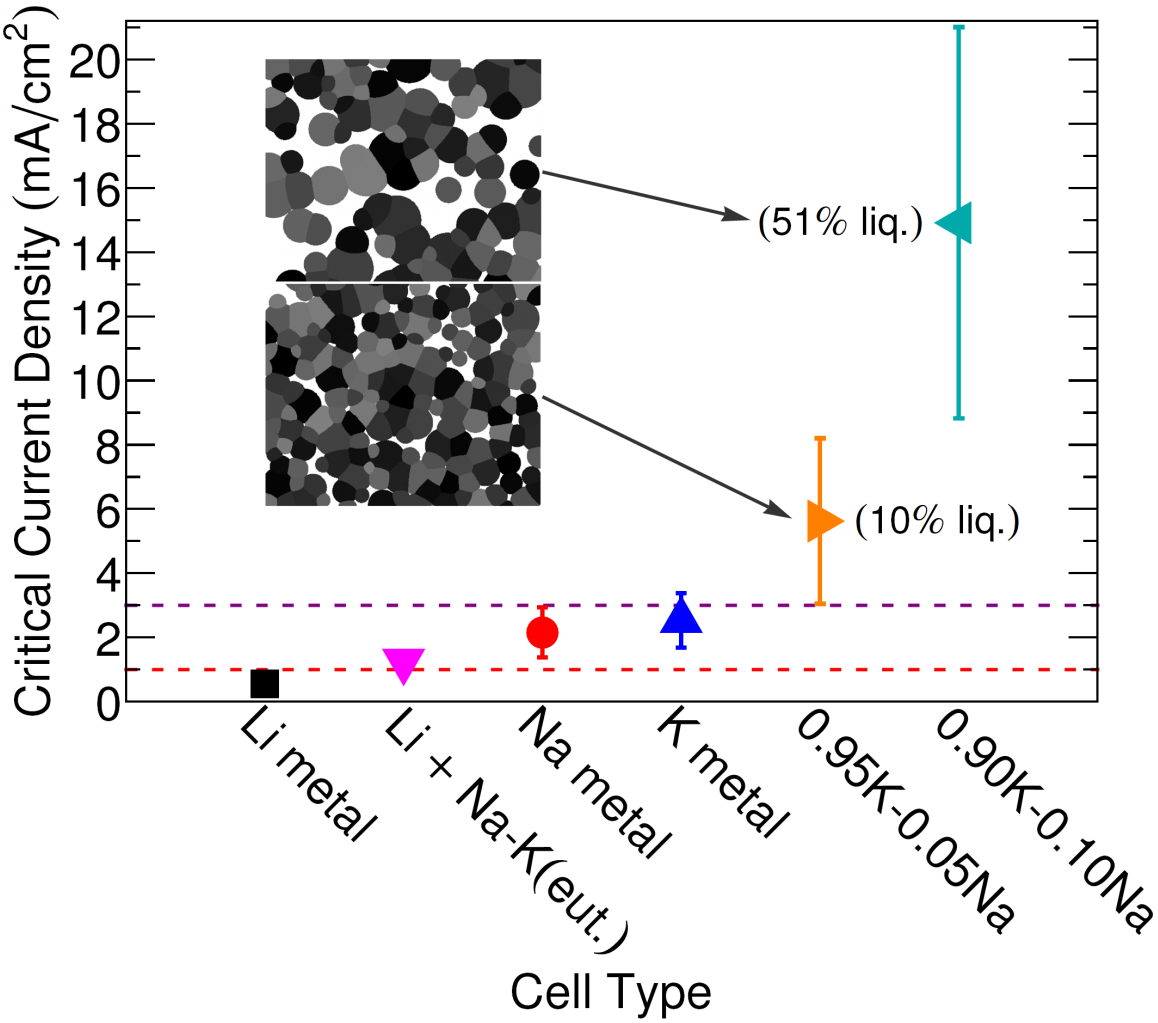

Figure 4-6: Average CCD value for each metal or alloy, which includes results across all areal capacities tested. Inset: a simulation of the expected electrode microstructures for the semi-solid experiments, in which the liquid phase appears as white and the solid crystalline phase particles as shades of grey.

Symmetric cell type	No. of samples, applied stack pressure	Mean CCD (mA cm^{-2})	σ CCD (mA cm^{-2})	Mean ACF	σ ACF
Li/LLZTO/Li	7 at 1.5MPa	0.502	0.295	1.11	0.22
Na/NBA/Na	4 at 1.5MPa	2.15	0.800	1.56	0.06
K/KBA/K	3 at 1.5MPa	2.53	0.743	2.19	0.236
0.95K-0.05Na/KBA/0.95K-0.05Na	4 at 1.5MPa	5.62	2.63	2.26	0.504
0.90K-0.10Na/KBA/0.90K-0.10Na	3 at 1.5MPa	14.9	5.39	1.73	0.149
Li-NaK(eut)/LLZTO/Li-NaK(eut)	3 at 1.5MPa	1.21	0.463	1.09	0.133

Table 4.1: Symmetric cells studied in this work. The notation 0.95K-0.05Na and 0.90K-0.10Na denote binary alloy electrodes of 95 and 90 mol% K respectively, whilst Li-NaK(eut.) denotes a Li electrode with a thin coating (~5 µL) of Na-K alloy at the eutectic composition (68 mol% K, 32 mol% Na). The abbreviations CCD and ACF denote "Critical Current Density" and "Area Correction Factor", respectively, whilst σ denotes the sample standard deviation as per the previous chapter.

the same throughout the cycling experiment for the "high liquid" composition of 90% K (~50% liquid) and the "low liquid" composition of 95% K (~10% liquid). The two Na/K ratios in this experimental design were thus selected to change the liquid fraction in the semi-solid electrode, which according to our model should raise the CCD as the liquid fraction increases.

Cells that used compositions A and B reached maximum CCDs as high as 8 mA cm^{-2} and 20 mA cm^{-2}, respectively. The average CCD values (based on N=4 and N=3 cells, respectively) are ~4 times and ~6 times higher than that achieved with K metal alone (Figures 4-5 and 4-6). The CCDs reached with composition B (mean value of 14 mA cm^{-2} at areal capacities of 1.5–2 mAh cm^{-2}) also exceeded the highest reported room-temperature value for solid Na metal cells (12 mA cm^{-2}, measured at a much lower areal capacity of 0.25 mAh cm^{-2}) (ref. [76]). The results demonstrate that even a small percentage of co-existing liquid is effective in increasing the CCD of an alkali metal electrode. Examination of Figures 4-7 and 4-8, respectively, indicates that the area specific resistance of the 0.95K–0.05Na/KBA/0.95K–0.05Na cell and the 0.90K–0.10Na/KBA/0.90K–0.10Na cell are both on the order of ~30 Ω cm^2; the difference in CCD is not correlated with any meaningful difference in interfacial area specific resistance.

4.3.3 Interfacial liquid film electrode design

Given that Li-ion technology is more well-developed than Na-ion or K-ion technologies, we also considered semi-solid anode design possibilities in which Li is the working ion. Using Li metal is further attractive as it possesses the highest capacity of any metal anode (3869 mAh g^{-1}, 2066 Ah L^{-1}). In the Li–Na and Li–K binary systems, the equilibrium liquid fields do not extend all the way to room temperature (see phase diagrams in Figures 4-1 and 4-2), so room-temperature semi-solid electrodes are not available. In contrast, the Na–K eutectic at 260.5°K (Figure 4-3) indicates at least a limiting composition (0.32Na–0.68K, by mole) in which a room-temperature liquid can be accessed. Thus, an electrode design in which a thin Na–K liquid film is used in conjunction with a solid Li metal electrode was conceived (Figure 4-4, right panel).

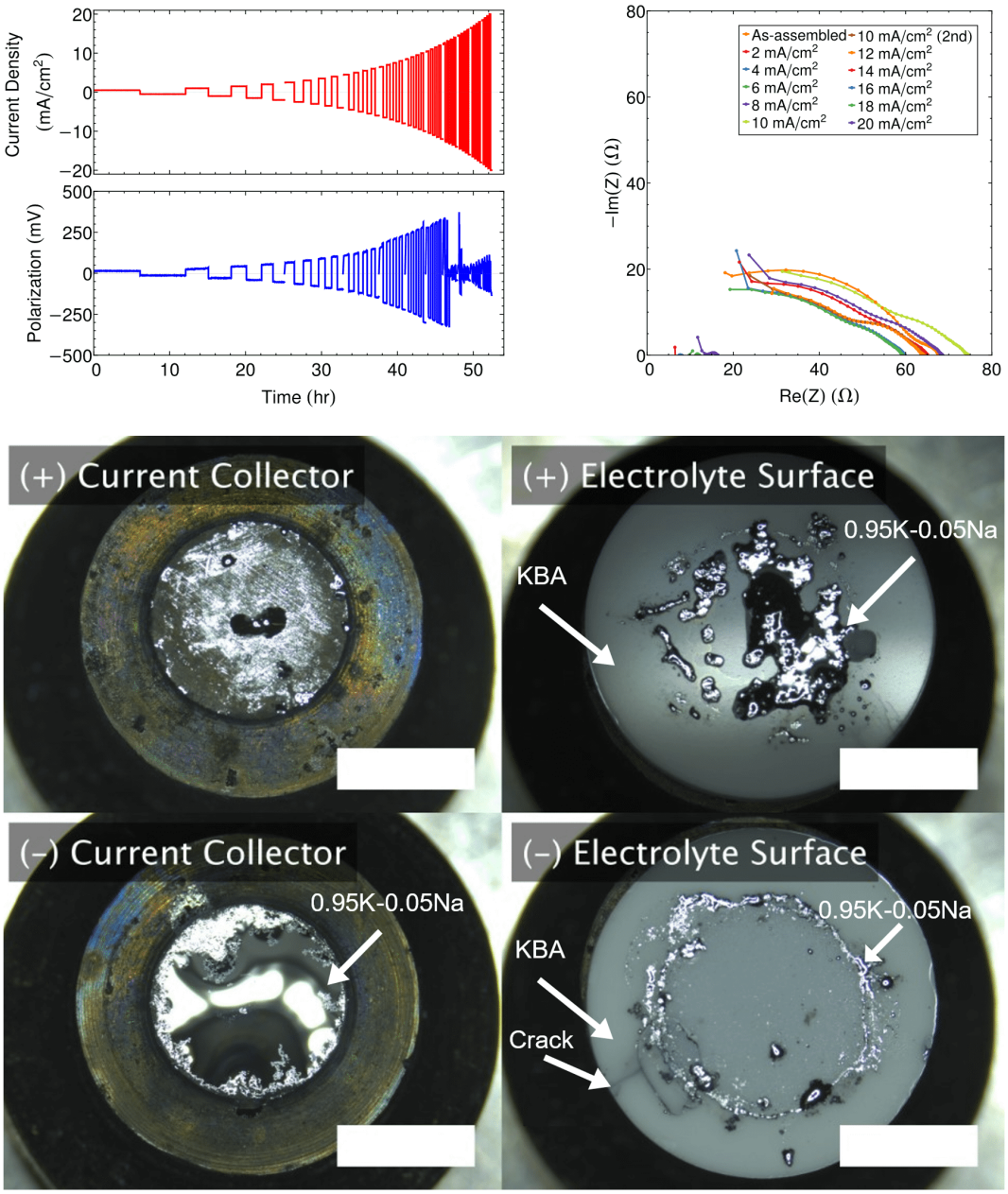

Figure 4-7: Galvanostatic cycling results for a symmetric 0.95K-0.05Na /KBA/ 0.95K-0.05Na cell at room temperature. (top left) The current density is increased stepwise while plating a constant 3 mAh cm^{-2} (based on the initial assumed area) capacity in both polarities. The corresponding cell polarization shows a sudden drop at 12–12.5 mA cm^{-2} corresponding to the formation of a short circuit (corresponding to a true critical current density of 4.52±0.09 mA cm^{-2}). (top right) IS spectra taken after each cycle show a disappearance of the arc, corresponding to interfacial capacitance, once the short circuit forms. (bottom) Optical digital microscopy images of the current collector and electrolyte interface of the 0.95K-0.05Na /KBA/ 0.95K-0.05Na cell post failure and disassembly. Scale bars denote 5 mm.

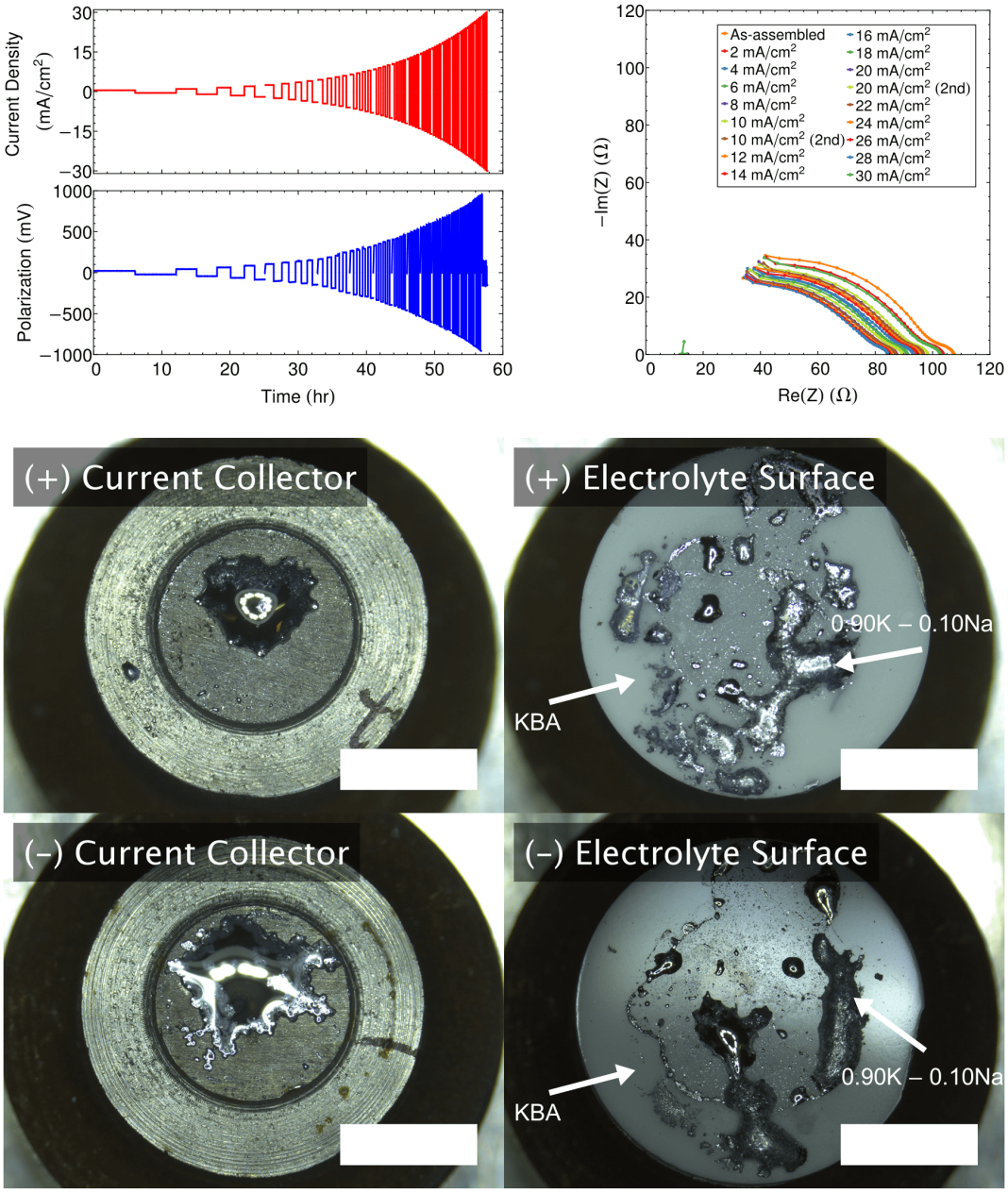

Figure 4-8: Galvanostatic cycling results for a symmetric 0.90K-0.10Na /KBA/ 0.90K-0.10Na cell at room temperature. (top left) The current density is increased stepwise while plating a constant 3 mAh cm^{-2} (based on the initial assumed area) capacity in both polarities. The corresponding cell polarization shows a sudden drop at 28–28.5 mA cm^{-2} corresponding to the formation of a short circuit (corresponding to a true critical current density of 15.4±0.14 mA cm^{-2}). (top right) IS spectra taken after each cycle show a disappearance of the arc, corresponding to interfacial capacitance, once the short circuit forms. (bottom) Optical digital microscopy images of the current collector and electrolyte interface of the 0.90K-0.10Na /KBA/ 0.90K-0.10Na cell post failure and disassembly. Scale bars denote 5 mm.

The Li–Na–K ternary phase diagram (Figure 4-9) was calculated to determine the co-existing phases and compositions present in such an electrode. The isothermal section of this ternary diagram at 300°K shows a wide two-phase field (the triangle with blue lines) within which solid Li (the body-centred cubic (BCC) phase) co-exists with the Na–K liquid in a simple two-phase equilibrium. The blue lines are tie lines that join the co-existing solid and liquid compositions and show that the solid Li metal phase co-exists with liquid alloy that can take on a wide range of Na/K ratios. The Na–K liquid dissolves a small amount of Li, a solubility that cannot be resolved in Figure 4-9. The solubility was also calculated and is shown in Figure fig:park7c. The solubility of Li is highest in Na-rich liquids and decreases by about a factor of 20 from the Na-rich to K-rich liquids that can co-exist with Li metal, but the Li solubility in the liquid is less than 1% throughout. There are no ternary phases.

Based on this understanding, we constructed cells in which a thin layer of the Na–K eutectic liquid was placed at the interface between LLZTO and a Li metal foil electrode. This interfacial film may serve one or both of two functions. The first is to transport Li from the solid Li metal electrode to the solid electrolyte while maintaining a conformal liquid layer of negligible yield stress, and thereby raise the CCD. The second is to act as an electronically conductive 'liquid current collector' that can flow to fill any voids that would otherwise form in the solid Li electrode during stripping and plating. In this role, the liquid metal film may homogenize the plating current density, which reduces the risk for short circuits and enables higher areal capacities. One or both functions provide 'self-healing' characteristics to the electrode as they mitigate the formation of interfacial defects exacerbated on cycling.

We performed sessile-drop wetting experiments, which showed that the Na–K eutectic alloy has a lower contact angle on LLZTO than that of any of the pure alkali metals (Results are shown in Figure 4-11, plotted as contact angle vs temperature for each metal.) at temperatures at which all are liquid, and lower than that of the contact angle of solid Li on LLZTO [13]. This indicates that in our cell design, the Na–K eutectic liquid will wet the LLZTO in preference to the solid Li metal, and thereby remain as an interfacial film in between the LLZTO and Li metal.

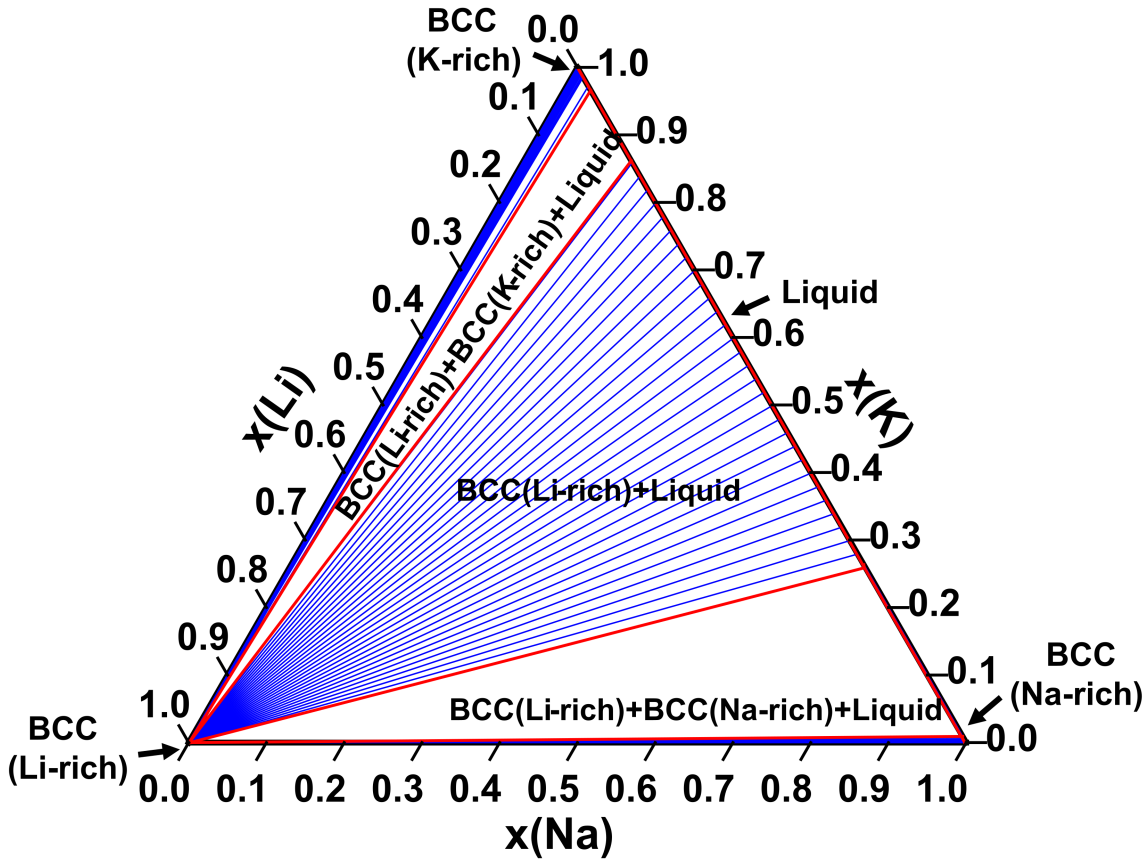

Figure 4-9: Isothermal section of Li–Na–K at 300 K. The high mixing enthalpy between BCC Li and Na/K liquid leads to a low solubility of each in the other. A wide two-phase field exists within which nearly pure BCC Li co-exists with the Na–K liquid (tie lines shown in blue).

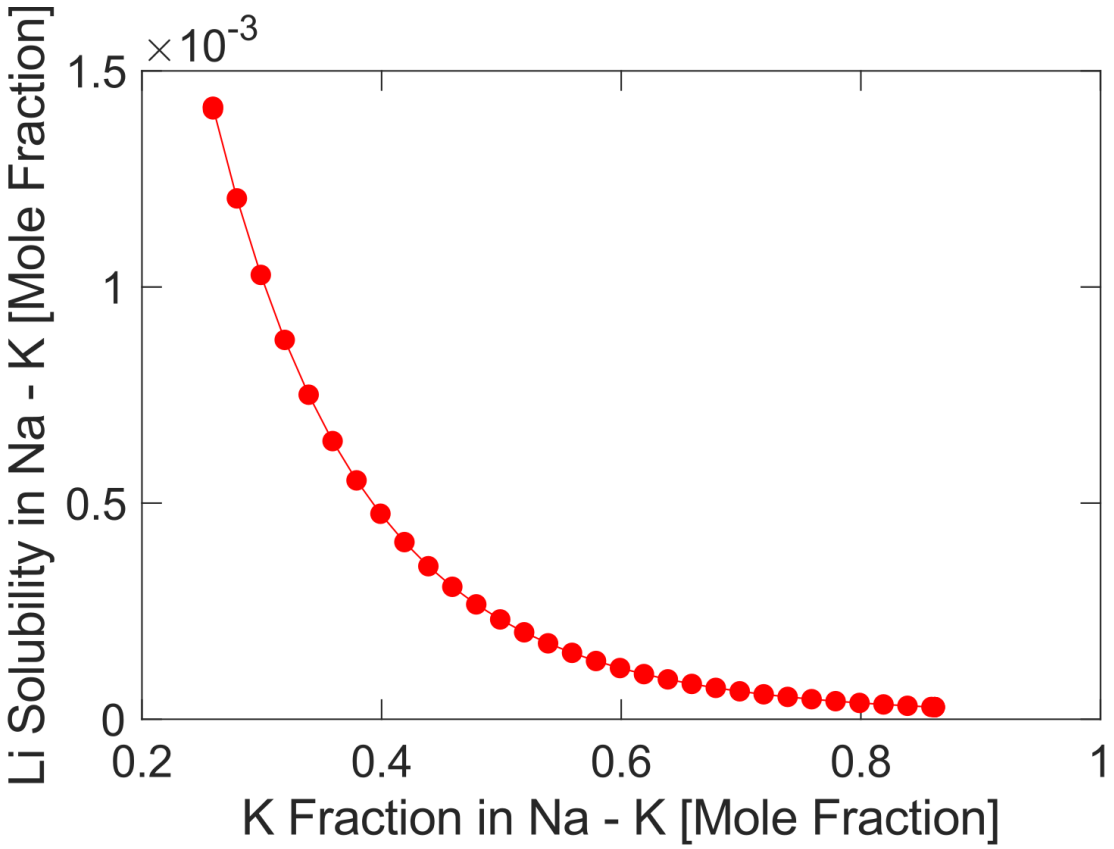

Figure 4-10: The solubility of Li in the Na–K liquid decreases sharply with an increasing K concentration of the liquid. The solid red curve serves as a guide for the eye.

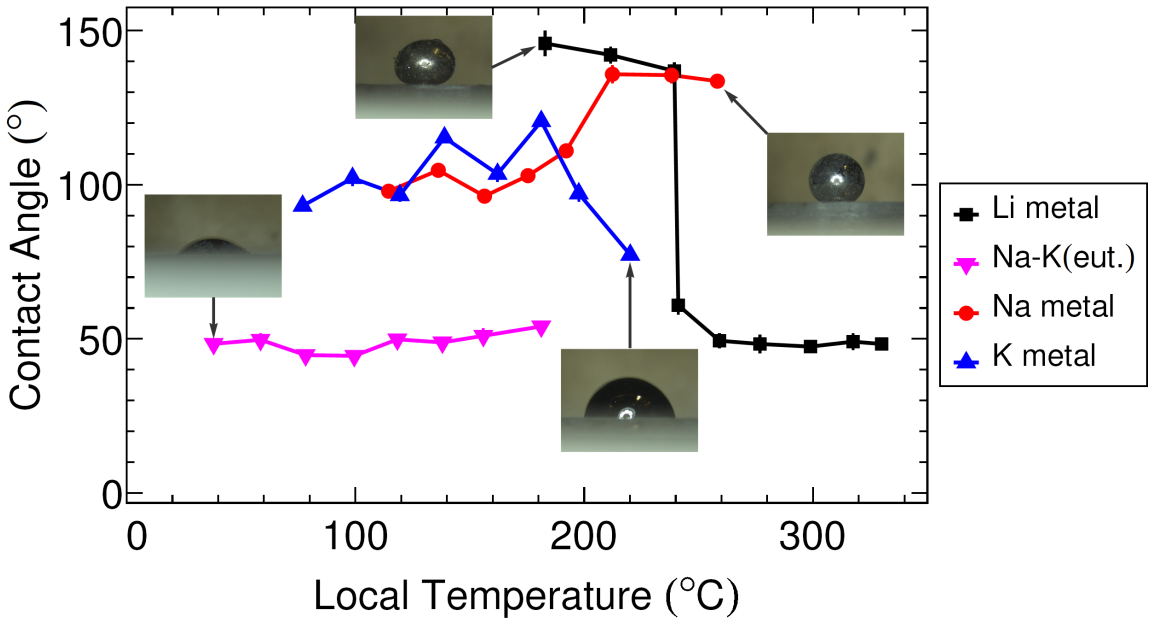

Figure 4-11: Alkali metal wetting of LLZTO measured using a sessile drop method. Experiments are conducted at temperatures where each metal is liquid. Contact angles measured for lithium, 0.68K-0.32Na (by mole), sodium, and potassium metal on polycrystalline LLZTO, as a function of temperature at 20°C increments. Examples of side view images are shown, with arrows pointing to the data points they represent.

Cycling tests were conducted over a wide range of areal capacities from 0.25 to 3.7 mAh cm^{-2} (Figure 4-5). Compared with the control cells using Li metal alone, both the average and the maximum CCD values are higher by about a factor of two. The average CCD increased from 0.50 mA cm^{-2} (Li) to 1.21 mA cm^{-2} (Li–NaK), and for the latter several cells approached 2 mA cm^{-2} (Figure 3-12). Equally important, however, the higher CCDs with the alloy approach could be accessed at areal capacities as high as 3.8 mAh cm^{-2}, which is nearly an order of magnitude higher than the highest values in previous literature studies for Li metal, in which areal capacities are $<$ 0.40 mAh cm^{-2} (Figures 3-12 and 4-5). The low and stable impedance of the cells using the Na–K liquid between the Li metal and LLZTO throughout the cycling experiments suggests a low chemical reactivity between the Na–K liquid and LLZTO. In our wetting experiments, there also was no evidence of reactivity between the Na–K liquid and polished LLZTO surfaces.

From these results we infer, first, that Li is transported through the Na–K liquid layer and, second, that a thin continuous film of the Na–K liquid is retained at the LLZTO–Li metal interface. When the Li metal is removed from the solid electrolyte surface, the Na–K liquid, which is distinguishable from the Li metal by its high reflectivity, remains on both the LLZTO surface and the Li metal disc. The amount of Na-K alloy used in the experiment (5 µL) corresponds to ~70 µm of liquid at the electrode area used (~0.7 cm_2) if uniformly distributed. However, the actual liquid layer thickness is greatly reduced upon the application of stack pressure (~1.5 MPa and ~75 kPa), with the excess liquid accumulating at the edges of the electrode. The final layer thickness should be determined by the surface roughness of the solid electrolyte and the lithium metal foil. Since the polished solid electrolyte has sub-micrometer roughness, while the lithium metal foil likely has tens of micrometers initial surface roughness (which may smooth under pressure), we estimate that the thickness of the Na-K liquid metal layer is ~10 µm. A thin Na-K layer is desirable to minimize the transport length for Li to the solid electrolyte; conversely, a comparatively thick Na-K film would possess a larger transport length for Li to the solid electrolyte and add to cell impedance.

In addition, features were observed in the electrochemical tests that support the interpretation that voids formed during Li stripping, are indeed 'healed' in the presence of interfacial Na–K liquid. For the cells with purely Li metal electrodes, attempts to cycle them to current densities greater than ~1 mA cm^{-2} were unsuccessful due to an 'open-circuit' failure mode characterized by a large impedance rise after several galvanostatic cycles. An example of such an impedance rise is seen in Figure 3-13, and starts at the fourth cycle of the Li/LLZTO/Li symmetric cell cycling at a 0.5 mA cm^{-2} current density with a 1.5 mAh cm^{-2} areal capacity (~7.5 µm Li metal deposited per half-cycle) and continues in subsequent cycles. This rise in impedance is consistent with interfacial void formation, and eventual delamination [75, 78].

This failure mode was not observed in any of the 14 cells tested in which the interfacial Na–K liquid was introduced between the Li metal foil and the solid electrolyte. The example in Figure 4-12 shows the polarization remaining below 300 mV in the sixth cycle of a cell cycling at areal capacity of 3.0 mAh cm^{-2} (~15 µm Li thickness per half-cycle) at 1.5 mA cm^{-2}, corresponding to a cumulative deposited Li thickness of ~180 µm. We attribute the greater stability at higher per-cycle and cumulative areal capacities to the *in-situ* healing of interfacial defects formed during Li metal stripping [78]. Kasemchainan et al. [78] found that the effects of void formation can be reduced by the application of substantial stack pressures (for example, 7 MPa). In our experiments, this failure mode appears to be mitigated even at a very low stack pressure (~75 kPa; Figure 3-12) on introduction of the interfacial liquid film.

4.4 Conclusions

The CCD at which metal penetration occurs through solid electrolytes and leads to an electrical short circuit was explored for metal electrodes that represent two distinct strategies towards a higher performance: using semi-solid electrodes that consist of co-existing solid and liquid alkali metal phases, and introducing a wetting interfacial liquid film between the electroactive metal and solid electrolyte. It is possible to increase the CCD to nearly 15 mA cm^{-2} by using a biphasic or semi-solid Na–K

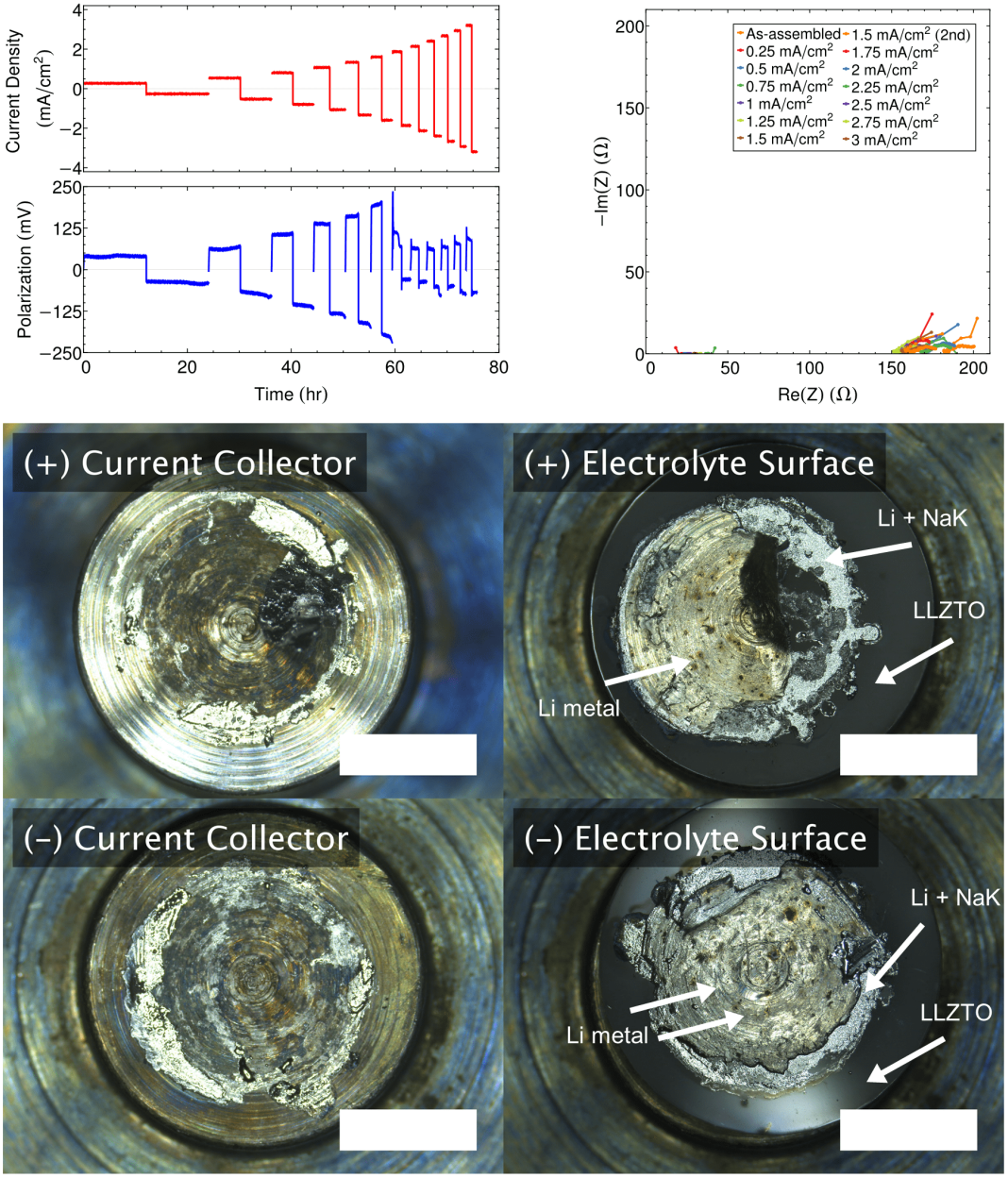

Figure 4-12: Galvanostatic cycling results for a symmetric Li–NaK(eut.) /LLZTO/ Li–NaK(eut.) cell at room temperature. (top left) The current density is increased stepwise while plating a constant 3 mAh cm^{-2} (based on the initial assumed area) capacity in both polarities. The corresponding cell polarization shows a sudden drop at 1.75-2 mA cm^{-2} corresponding to the formation of a short circuit (corresponding to a true critical current density of 1.65±0.13 mA cm^{-2}). (top right) IS spectra taken after each cycle show a disappearance of the arc, corresponding to interfacial capacitance, once the short circuit forms. (bottom) Optical digital microscopy images of the current collector and electrolyte interface of the Li–NaK(eut.) /LLZTO/ Li–NaK(eut.) cell post failure and disassembly. Scale bars denote 5 mm.

electrode. This approach, which yields the high CCD of a liquid metal electrode without sacrificing the packaging advantages of a solid electrode, enables the highest CCD reported to date for any alkali metal electrode at room temperature. When a thin film of interfacial Na–K liquid is introduced between the Li metal and solid electrolyte, a factor of two increase in the CCD is accompanied by the ability to cycle to areal capacities greater than 3.5 mAh cm^{-2} at stack pressures as low as 75 kPa. For both the semi-solid electrode approach and the interfacial liquid-film approach, the ability to cycle at high areal capacities without an impedance rise indicates that failure modes, such as interfacial void formation, can be averted. These design approaches can be extended to other alloy systems. Further development of these strategies may be fruitful in the pursuit of high-energy density all-solid-state batteries.

THIS PAGE INTENTIONALLY LEFT BLANK

Chapter 5

Interfacial liquids enabling ultra-high stripping areal capacities

In this chapter, we demonstrate that a wetting interfacial film of Na–K liquid between Li metal and $Li_{6.75}La_3Zr_{1.75}Ta_{0.25}O_{12}$ solid electrolyte permits reversible stripping and plating of up to 150µm of Li (30 mAh cm^{-2}), approximately ten times the areal capacity of today's lithium-ion batteries, at current densities above 0.5 mA cm^{-2} and stack pressures below 75 kPa, all with minimal changes in cell impedance. We further show that this increase in the accessible areal capacity at high stripping current densities is due to the presence of Na-K liquid at the Li stripping interface; this performance improvement is not enabled in the absence of the Na-K liquid. This design approach holds promise for overcoming interfacial stability issues that have heretofore limited performance of solid-state metal batteries.

At the time of writing this thesis, the contents of this chapter have not yet been published. Andres Badel performed the image analysis of disassembled cells.

5.1 Introduction

The previous chapters of this thesis establish that the interface between Li metal and an inorganic solid electrolyte suffers from two significant challenges. The first is a susceptibility to short circuits due to penetration by metal filaments (often referred to as

"dendrites") upon deposition at current densities exceeding a critical value (hereafter referred to as the "critical current density, CCD") in the range 0.1–1 mA cm^{-2} (at room temperature), which is too low for many practical applications [3, 10, 11, 36–38, 53]. The second problem is that of impedance rise due to the formation of voids at the solid electrolyte/anode interface during electrostripping [75, 78, 87]. This issue is particularly exacerbated at stripping current densities over 0.5 mA cm^{-2} and has the effect of limiting the accessible areal capacity to 1.5 mAh cm^{-2} within typical voltage windows ($<$ 1V stripping overpotential) [65]. Furthermore, void formation at the electrolyte-electrode interface increases the likelihood for cell failure via the metal penetration mechanism upon subsequent plating. This is due to the increase in local plating current density since the reduction in interfacial contact area occurs non-uniformly upon void formation and creates current constriction "hot spots" between electrode and electrolyte [78]. It has been shown that the accumulation of these electrostripping-induced voids depends on both the magnitude of the stripping current density and the rate of replenishment of Li at the interface by Li metal creep [87]. This second process is a function of the applied stack pressure, where increasing pressure increases the maximum sustainable current density for avoiding voids (0.2 mA cm^{-2} at 3 MPa, 1.0 mA cm^{-2} at 7 MPa for the Li/Li_6PS_5Cl/Li system). Similar trends and behavior have further been observed in an analogous system incorporating solid Na metal electrodes and Na–β"–Al_2O_3 solid electrolyte. [75] This requirement of large stack pressures for preventing void formation during cell cycling represents a substantial engineering challenge that may hinder the development of robust batteries at the cell, module, and pack level.

In this chapter we show that a recently developed semi-solid (i.e., multiphase liquid-solid) electrode approach [65] can mitigate the formation of voids during Li metal stripping at room temperature, and at stack pressures as low as 75 kPa (11 psi). This electrode design uses a thin film of Na-K liquid between the Li metal electrode and Li conducting solid electrolyte as a self-healing layer. Using the model solid electrolyte $Li_{6.75}La_3Zr_{1.75}Ta_{0.25}O_{12}$ (LLZTO), we first show that ultra-high stripping/plating areal capacities up to the order of 30 mAh cm^{-2} can be reached in

Li/NaK/LLZTO/ NaK/Li symmetric cells (where the notation "NaK" denotes the liquid sodium - potassium alloy of compositions discussed later) with low and stable area-specific-resistance (ASR, 15 Ω cm^2 per interface) at current densities above 0.5 mA cm^{-2}. Such cell performance is achievable at minimal stack pressures and without "pre-forming" the Li metal/solid electrolyte interface at elevated stack pressures (>1.5MPa) and temperatures (~170°C), as is commonly done in the literature to form a low impedance ($<$ 500 Ω cm^2 [11], $<$ 35 Ω cm^2 [10, 65] per interface) Li/LLZTO interface. We further show that this dramatic increase in the accessible areal capacity at high stripping current densities is due to the presence of the Na-K liquid at the interface from which the lithium is being stripped. This performance improvement is not observed in the absence of the Na-K liquid. These results demonstrate the efficacy of a design approach that takes advantage of the low contact impedance and high accessible areal capacity of a liquid metal electrode, while having the shape retention and cell packaging advantages of solid metal electrodes, all without requiring high stack pressure.

5.2 Methods

5.2.1 Electrochemical cell assembly

Prior to assembly, the solid electrolyte discs were polished and heat treated in the manner described in Section 3.2. The Li/LLZTO/Li electrochemical cells were assembled in the manner described in Section 3.2 by placing a disc of flat lithium foil (0.375" diameter, 0.25 mm thickness, 50 mAh cm^{-2}, ~20 µL lithium) on the LLZTO solid electrolyte with a stainless-steel cylinder acting as the current collector. Before electrochemical cycling, the cells were heated to 170°C for 3h at an applied stack pressure of 1.5 MPa (calibrated independently with a compression force gauge), which reduced the interfacial impedance of the cell. The area-specific interfacial impedance of the cells was measured to be on the order of 25–35 Ω cm^2 (sum of both interfaces).

Lithium metal cells incorporating the eutectic Na-K alloy layer were assembled in

the manner described in Section 4.2. This method is similar to the process used to assemble the plain lithium cells except that 5 µL of eutectic Na-K alloy (68 mol% K) was spread on one face of the punched lithium disc. The side of the lithium disc with the added Na-K alloy was placed in contact with the LLZTO solid electrolyte disc. Before electrochemical cycling, certain cells incorporating the Na-K alloy were subject to the same heat treatment as the plain lithium cells, whilst the remainder were not subject to any heat treatment. During electrochemical cycling, some cells had an applied stack pressure of 1.5 MPa (calibrated independently with a compression force gauge). For the cells cycled under low pressure (~75 kPa), the springs in the fixture were compressed to a few percent strain based on visual inspection.

The amount of Na-K alloy used in the experiment (5 µL) corresponds to ~70 µm of liquid at the electrode area used (~0.7 cm^2) if uniformly distributed. However, the actual liquid layer thickness is greatly reduced upon the application of stack pressure (~1.5 MPa and ~75 kPa), with the excess liquid accumulating at the edges of the electrode. The final layer thickness should be determined by the surface roughness of the solid electrolyte and the lithium metal foil. Since the polished solid electrolyte has sub-micrometer roughness, while the lithium metal foil likely has tens of micrometers initial surface roughness (which may smooth under pressure), we estimate that the thickness of the Na-K liquid metal layer is ~10 µm.

5.2.2 Electrochemical cell cycling

Galvanostatic experiments were conducted on the cells at 22°C using a Bio-Logic VMP-3 cell test system. Several Li/NaK/LLZTO/NaK/Li cells were subjected to galvanostatic cycling at nominal current densities (i.e., based on initial electrode areas) from 0.25 to 3 mA cm^{-2} using 0.25 mA cm^{-2} increments at a nominal areal capacity of 6 mAh cm^{-2} per half-cycle (30 µm lithium plating thickness). Other cells, cycled under nominal areal capacities of 15 and 30 mAh cm^{-2} per half cycle (75 and 150 µm lithium plating thickness respectively), were subjected to galvanostatic cycling at nominal current densities from 0.5 to 3 mA cm^{-2} using 0.5 mA cm^{-2} increments. Li/LLZTO/NaK/Li asymmetric cells and their respective Li/LLZTO/Li controls were

subjected to 1 galvanostatic cycle at nominal current densities of 0.25 or 0.5 mA cm^{-2} at a nominal areal capacity of 6 mAh cm^{-2}. As discussed in the *Results*, actual current densities were determined by measurement of electrode areas in the disassembled cells. Impedance spectra were collected at the start of testing and after each galvanostatic cycle for the Li/NaK/LLZTO/NaK/Li cells. Throughout electrochemical testing, cells remained in an argon-filled glove box with oxygen and water content below 0.1 ppm and 0.1 ppm, respectively. Upon completion of electrochemical cycling, ex-situ microscopy was conducted on disassembled cells using a Leica DMS300 (Leica Camera, Wetzlar, Germany) digital microscope.

5.3 Results and discussion

5.3.1 Critical current density measurements

The Li/NaK/LLZTO/NaK/Li electrochemical cells were constructed as described in *Methods*. Details of the LLZTO sample preparation and the subsequent surface, mechanical, and electrical property characterization are available in Chapter 3. The critical current density (CCD) was measured by reversibly plating Li metal in both directions at stepwise increasing galvanostatic currents until a discontinuous change in current and polarization across the cell signaled the onset of a short circuit (Figure 5-1 (top left)). We use the example of the Li–NaK/LLZTO/Li–NaK symmetric cell in Figure 5-1 to illustrate how the short circuits were identified. Here, the short circuit occurred at the beginning of the 12th cycle after a cumulative plated lithium thickness of ~700 µm (60 µm per cycle, 30 µm per half-cycle corresponding to 6.0 mAh cm^{-2} in each direction). The elapsed time of the experiment was about 150 hours. Figure 5-1 (top left) shows the voltage-time trace for this experiment, where the sudden drop to zero voltage in the 12th cycle corresponds to the growth of a metal filled crack completely through the electrolyte disc.

Impedance spectroscopy was performed between stepwise increases in the galvanostatic current to further confirm whether a short circuit was present (Figure 5-1, (top

right)). Upon assembly, all electrochemical symmetric cells exhibited an impedance spectroscopy (IS) spectrum (Nyquist plot) that exhibited intercepts at high frequency on the real axis corresponding to the expected total resistance (~150 Ω) of the solid electrolyte disc (thickness ~1 mm) with ionic conductivity of 1–2 mS cm^{-1} [65]. IS spectra measurements (Figure 5-1, (top right)) after the sudden drop in polarization showed a disappearance of the arcs in the IS spectra, replaced by a single resistive point (<10 Ω) consistent with the formation of a short circuit.

Following the electrical detection of the short circuit, the cells were disassembled and imaged under an optical microscope to examine the surfaces of the positive and negative current collector as well as both surfaces of the solid electrolyte (Figure 5-1 (bottom)). In all cases the metal electrode remained confined within the boundary of the solid electrolyte disc, ruling out the possibility of an external electronic short circuit around the edges of the electrolyte disc. This supports the inference from the IS measurements that the sudden drop in cell impedance is due to metal penetration through the solid electrolyte. It was observed that the Li electrode increases somewhat in area during cell assembly due to spreading of the metal. The electrode area may further grow during cycling. Therefore, we calculated the final current density and areal capacity for the experiments based on the measured post-mortem electrode areas from disassembled cells after cycling to failure. This methodology yields the most accurate current densities and areal capacities at the point of short circuit. In some instances, opaque, semi-circular regions at the edge of the alkali metal electrode were observed in the solid electrolyte that appear to be metal filled, as indicated in Figure 5-1 (bottom). These regions likely indicate a location of crack propagation. Due to field concentration effects elucidated in prior work on single crystal solid electrolytes [53], crack and dendrite initiation near such electrode edges may be favored.

Figure 5-2 exhibits all of the critical current density measurements over the relevant areal capacities (3 –30 mAh cm^{-2}) performed in this study. Numerical data are listed in Table 5.1. Each datum in Figure 5-2 represents one critical current density measurement derived from a single cell. The room-temperature CCDs for the Li/NaK/LLZTO/NaK/Li symmetric cells are higher on average than that for plain

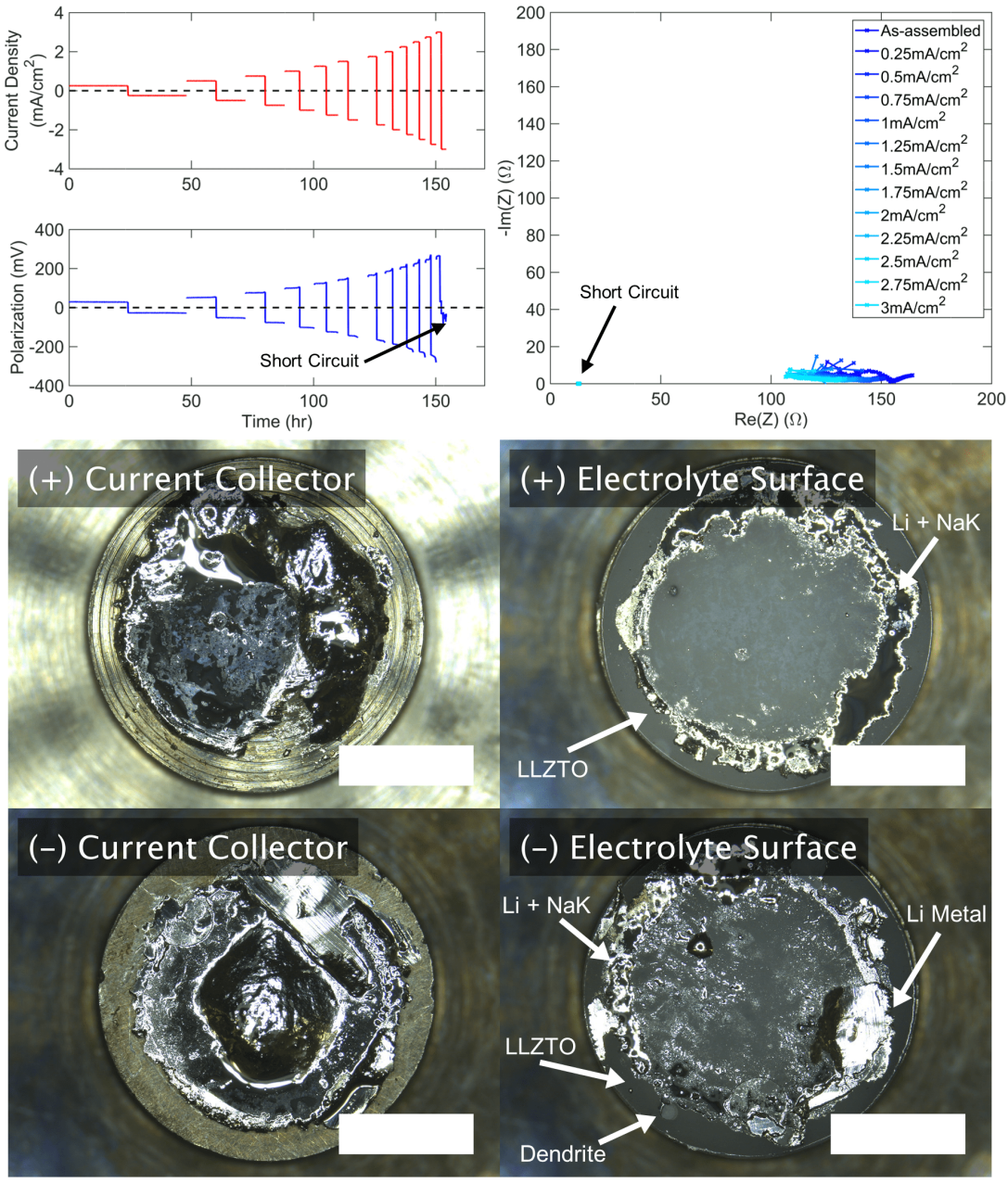

Figure 5-1: Galvanostatic cycling results for a Li–NaK/LLZTO/Li–NaK cell at room temperature. The composition of the NaK alloy is the eutectic (0.68% K by mole) (top left) The current density is increased stepwise while plating a constant 6 mAh cm^{-2} (based on the initial assumed area) capacity in both polarities. The corresponding cell polarization shows a sudden drop at 2.75-3 mA cm^{-2} indicating a short circuit (corresponding to a true critical current density of 2.17±0.09 mA cm^{-2} and areal capacity of 4.53 mAh cm^{-2}). (top right) IS spectra taken after each cycle show a disappearance of the capacitive arc once the short circuit forms. (bottom) Optical digital microscopy images of the current collector and electrolyte interface of the cell post failure and disassembly. Scale bars denote 5 mm.

Li metal ($<$ 1 mA cm^{-2}, [65]), reaching a maximum value around 2 mA cm^{-2}, consistent with results from Chapter 4. Note that results in Figure 5-2 show a variation in CCD even between nominally identical experiments. We expect a distribution of CCDs to be observed in these experiments, as a short circuit event is correlated with the fracture of the brittle inorganic ceramic electrolyte. Such fracture is inherently stochastic as it is the largest surface flaw on the solid electrolyte that is most likely to be responsible for failure, and the size of such a flaw will follow a statistical distribution [39, 42, 66]. It is therefore unsurprising that the measured CCD values exhibit some variability.

5.3.2 Accessible areal capacity measurements

The areal capacities used in our experiments (3 –30 mAh cm^{-2}, Figure 5-2) are up to nearly a hundred times higher than those at the high end of the range used in previous studies (0.25 mAh cm^{-2}) [3, 10, 11, 36–38, 53], except for measurements from Chapters 3 and 4 of this thesis in which areal capacities of ~3 mAh cm^{-2} were used [65].

We observe that the Li/NaK/LLZTO/NaK/Li cells still exhibit an elevated CCD (~1 mA cm^{-2}) relative to those for plain Li metal (~0.5 mA cm^{-2}) over this wider areal capacity range ranging from 3 to 30 mAh cm^{-2} (Figure 5-2). In contrast, the Li/LLZTO/Li symmetric cells exhibit critical current densities $<$ 1 mA cm^{-2} with accessible areal capacities being limited to values below 1.5 mAh cm^{-2}. This limitation in capacity is due to the rapid increase in cell impedance that is observed beyond 1.5 mAh cm^{-2} of plated capacity, when stripping and plating at a current density of 0.5 mA cm^{-2} or higher (Figures 5-4 - 5-6) [65]. Note that results in Figure 5-2 show a variation in areal capacity even between nominally identical experiments. This is because both the areal capacity shown are true values based on the final measured area of the metal electrodes in the disassembled cell, which exhibits some variability, as explained previously.

The Li/NaK/LLZTO/NaK/Li cells consistently exhibit CCDs $>$ 0.5 mA cm^{-2} within the areal capacity limits (3 –30 mAh cm^{-2}) regardless of whether the applied stack pressure is 1.5 MPa or $<$ 75kPa, or whether the Li metal was first pressed to the

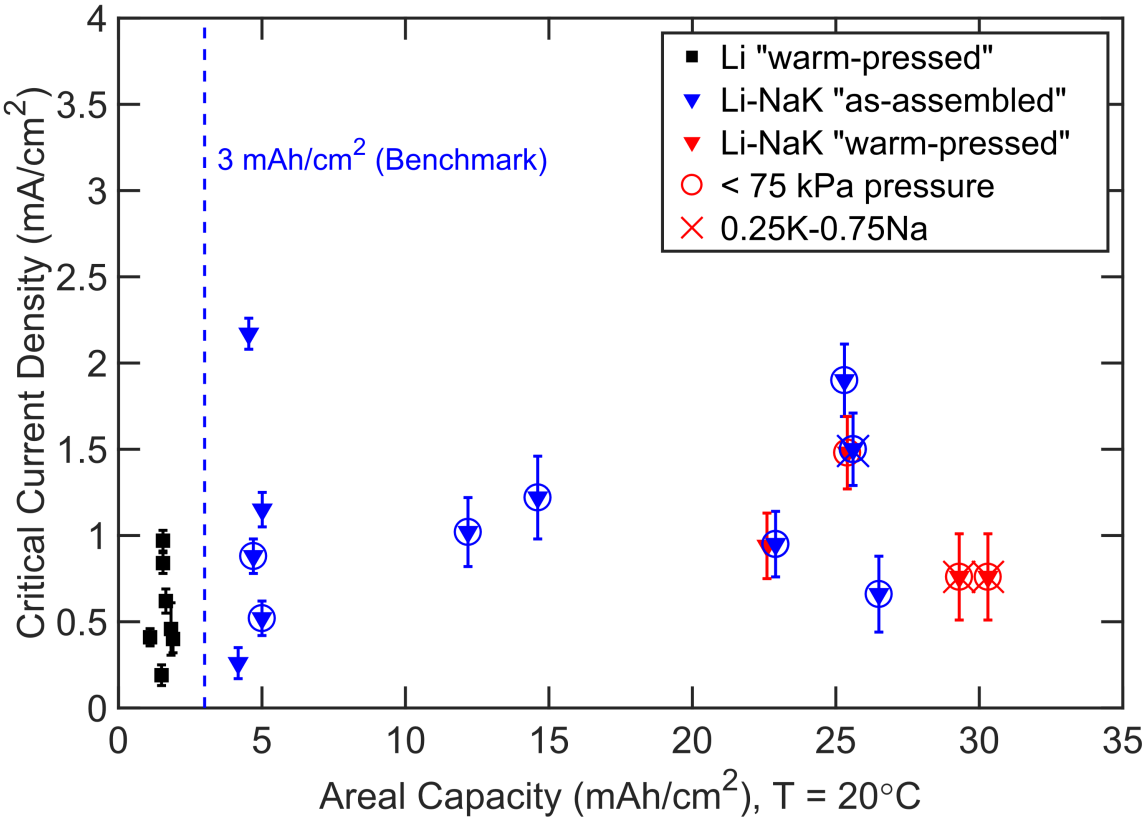

Figure 5-2: Critical current density for Li metal penetration in LLZTO at ultra-high areal capacities. CCDs for single-phase solid Li, and Li-NaK composite symmetric cells using LLZTO as the solid electrolyte. The composition of the NaK alloy is the eutectic (0.68K–0.32Na, by mole) in all cases except for two data points marked with a cross overlay (where the composition is 0.25K - 0.75Na, this alternative composition was used to test whether the CCD depended on the NaK composition). The liquid alloy is present at the interface between Li metal foil and LLZTO. All the experiments were conducted at 20°C under a nominal stack pressure of ~1.5 MPa, except for circled points, which are from experiments conducted at < 75 kPa. The term "warm-pressed" means that the cell was heated at 170°C for 3 hours under 1.5MPa stack pressure post-assembly, after which the cell was cooled to room temperature and the stack pressure removed if specified (see *Methods*). The term "as-assembled" means that no such pretreatment was performed, and that cycling was carried out immediately after assembly. Each datum represents an independent cell measurement. The total span of the error bars represents the variation in CCD for a single increment by which the current density was stepped in the galvanostatic protocol.

Symmetric cell type	No. of samples	Pre-forming	Mean CCD (mA cm^{-2})	σ CCD (mA cm^{-2})	Mean ACF	σ ACF
Li/LLZTO/Li	7	Yes	0.502	0.295	1.11	0.22
Li-NaK/LLZTO/Li-NaK	4	Yes	0.985	0.343	1.12	0.16
Li-NaK/LLZTO/Li-NaK	11	Yes	1.111	0.57	1.22	0.15

Table 5.1: Symmetric cells studied in this work. The notation Li-NaK denotes a Li electrode with a thin coating (~5 µL) of Na-K alloy at either the eutectic composition (68 mol% K, 32 mol% Na) or 75 mol% Na (see discussion). "Pre-forming" refers to whether the cell stack was heated after assembly at 170°C at 1.5MPa before being cooled back to ambient temperature. The abbreviations CCD and ACF denote "Critical Current Density" and "Area Correction Factor", respectively, whilst σ denotes the sample standard deviation as per the previous two chapters.

LLZTO at elevated temperature. The stable cycling of the Li/NaK/LLZTO/NaK/Li cells at these extreme areal capacity values with minimal cell polarization show that when the Na-K liquid is present, neither of these preprocessing steps is necessary. We interpret that the Na-K alloy serves simultaneously as an electrochemically inert liquid current collector that fills any Li voids that may form, homogenizing both the stripping and plating current, and as a Li transport medium that facilitates intimate ionic transport between the solid Li metal and LLZTO electrolyte. Together, these effects overcome the contact impedance problem for ionic transport that is common at solid metal - solid electrolyte interfaces. Despite the solubility for Li in the Na-K system being rather low, (on the order ~1×10^{-4} mole fraction [65]), the Na-K alloy is clearly capable of appreciable Li transport at the relevant length scale, since the first half-cycle of the cells, during which the Na-K liquid is wetting between the Li metal and solid electrolyte, exhibits low polarization. We observed similar CCD values (Figure 5-2) for two Na-K liquid compositions, 0.25K-0.75Na and 0.68K-0.32Na (by mole), even though the Li solubility in the liquid is a factor of four higher for the latter liquid composition.

5.3.3 Analysis of Li and Li/Na-K stripping interfaces

In the symmetric cells tested above, the same type of interface is being stripped of lithium and is depositing lithium at the same time, and does not allow the impact of the Na-K liquid on the two processes to be separated. We therefore constructed asymmetric Li/NaK/LLZTO/Li cells, in which the direction of current allows stripping to be performed at the Li or Li-NaK interface, while plating occurs at the opposing electrode (Figure 5-3). The behavior of the asymmetric cells was furthermore compared to that of symmetric Li/LLZTO/Li cells. The cells were subjected to a single cycle at fixed current densities of 0.25 or 0.5 mA cm^{-2}, to a fixed areal capacity of 6 mAh cm^{-2}. All cells had an applied stack pressure of 1.5 MPa with the Li metal pre-formed to the LLZTO electrolyte at 170°C under the same pressure. Comparing polarization curves with the Li/LLZTO/Li cell under the same testing conditions isolates the exact conditions that enable "ultra-high" accessible areal capacity, as the hallmark of

such behavior is extended stripping/plating with minimal increases in cell impedance ($< 50\ \Omega\ cm^2$). Such behavior indicates the absence of increasing cell impedance over time, which has been associated with stripping-induced voids.

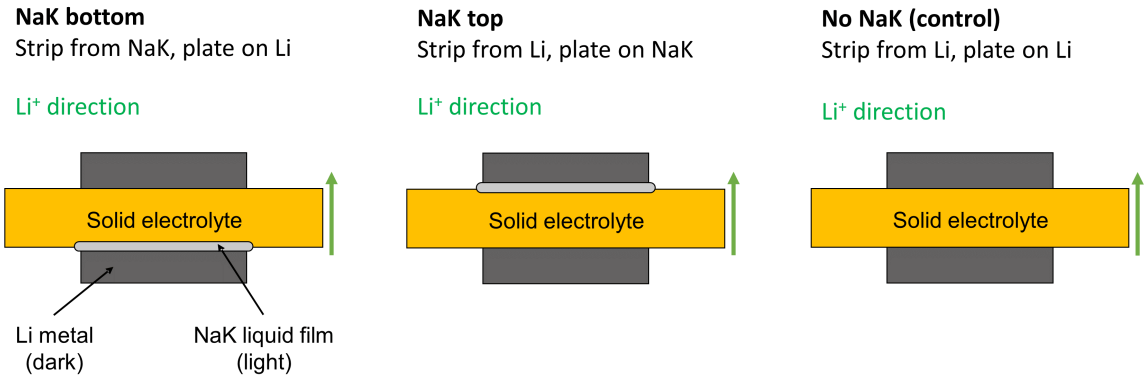

Figure 5-3: Design of asymmetric cell study. (left), (center) Li/LLZTO/NaK/Li asymmetric cells enable the simultaneous stripping from a Li-NaK electrode and plating onto a plain Li electrode (or vice versa depending on the direction of current). (right) Li/LLZTO/Li symmetric cells simultaneously strip and plate from a plain Li electrode. Comparison of these three cells allows determination of the stripping interface at which impedance rise due to void formation occurs and those at which it is averted.

Results are shown in Figures 5-4 to 5-6, each panel showing the current vs time profile in the top figure and the observed polarization in the bottom figure, as well as the ASR of the two interfaces combined, obtained after subtracting the resistance of the solid electrolyte. In all cases, stripping from the plain Li interface (Figure 5-3, center and right panels) resulted in a sharp rise in polarization and ASR. The rise in impedance was exacerbated at the higher stripping current density of 0.5 mA cm^{-2} (Figures 5-4 to 5-6 (right panels)), yielding cell ASR values of 1000-2000 $\Omega\ cm^2$, while tests at 0.25 mA cm^{-2} stripping current (Figures 5-4 to 5-6, left panels) yielded cell ASR values of 150-300 $\Omega\ cm^2$. In contrast, stripping from the NaK-Li electrode resulted in a lower ASR of 50-100 $\Omega\ cm^2$ for both stripping currents of 0.25 and 0.5 mA cm^{-2} (Figures 5-4 and 5-5), and stable polarization over the entire plated capacity of 6 mAh cm^{-2}. For the Li/LLZTO/Li symmetric cells (Figure 5-6), a sharp rise in impedance is observed regardless of the direction of current. The impedance of these cells is comparable in magnitude to that seen in the Li-NaK/LLZTO/Li asymmetric

cells when stripping occurs at the plain Li electrode.

These results conclusively show it is the presence of the layer of Na-K liquid that mitigates impedance growth at the interface from which Li is being stripped. In the Li/NaK/LLZTO/NaK/Li cells, stripping of lithium from this interface can be carried out to ultra-high areal capacities (30 mAh cm^{-2}) with minimal impedance growth. We interpret this behavior to indicate an absence of void formation in the Li metal, due to flow of the Na-K metal, which also acts as a mixed transport medium for electrons and Li atoms. In contrast, the sharp impedance rise and high overall impedance observed when Li is stripped from the solid Li metal electrode interface is consistent with void formation.

5.4 Conclusions

In summary, previous attempts to plate and strip Li metal mated with inorganic solid electrolytes at current densities above 0.5 mA cm^{-2} at high areal capacities ($>$ 1.5 mAh cm^{-2}) have met with cell failure due to either metal penetration of the solid electrolyte or void formation at the interface being stripped [3, 10, 11, 36–38, 53, 65, 78, 87]. The main strategy for mitigating void formation and increasing the critical current density has involved the application of significant stack pressures (up to 7 MPa) to replenish Li at the interface via metal creep [75, 78, 87]. In contrast, we show in this chapter that by introducing a thin layer of liquid Na-K alloy at the interface between Li metal and LLZTO solid electrolyte it is possible to strip Li metal at current densities above 0.5 mA cm^{-2} with stable impedance up to stripped capacities of 30 mAh cm^{-2}, while using minimal stack pressure. The Na-K alloy further provides an additional benefit of eliminating the need for pretreating the lithium-solid electrolyte assembly to form a low impedance interface. The findings presented herein thus open novel ways to streamline the processing of metal electrode/ceramic electrolyte interfaces and relax design constraints for battery engineering at the pack level. These results may promote the development of alternative Li-metal battery architectures enabling high-energy density all-solid-state batteries.

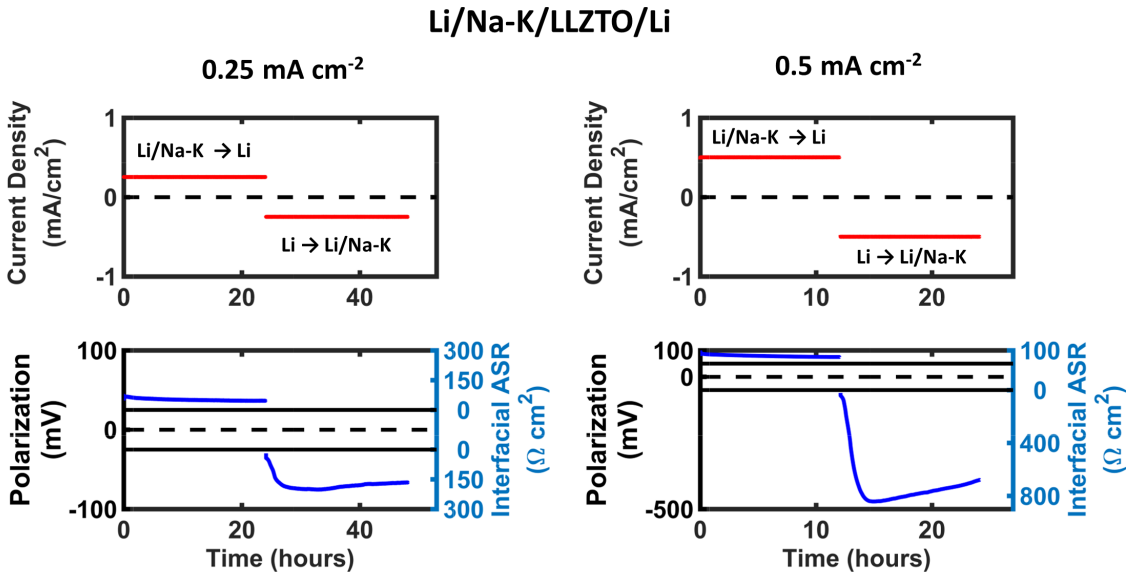

Figure 5-4: Polarization curves from Li/NaK/LLZTO/Li asymmetric cells in which Li is initially stripped from a Li/Na-K interface and plated at a plain Li interface. (left) Current and voltage time-traces for cells undergoing one full cycle (areal capacity of 6mAh cm^{-2}) at a current density of 0.25 mA cm^{-2}. (right) Analogous time-traces for an independant cell undergoing one full cycle (areal capacity of 6mAh cm^{-2}) at a current density of 0.5 mA cm^{-2}. In both cases positive current corresponds to stripping from the NaK-Li composite electrode and plating on the plain Li electrode. The stripping and plating electrodes are reversed upon the reversal of current. Note that the vertical axis scale is different in each subfigure. In each subplot, the interfacial ASR values provided are the total contribution from both interfaces within the cell. This value is obtained by subtracting the ASR due to the bulk electrolyte (100 Ω cm^2) from the total measured ASR. The cell polarization that corresponds to zero interfacial ASR in each current direction is indicated by the solid black bands. Rapid impedance rises are associated with stripping from a plain Li electrode.

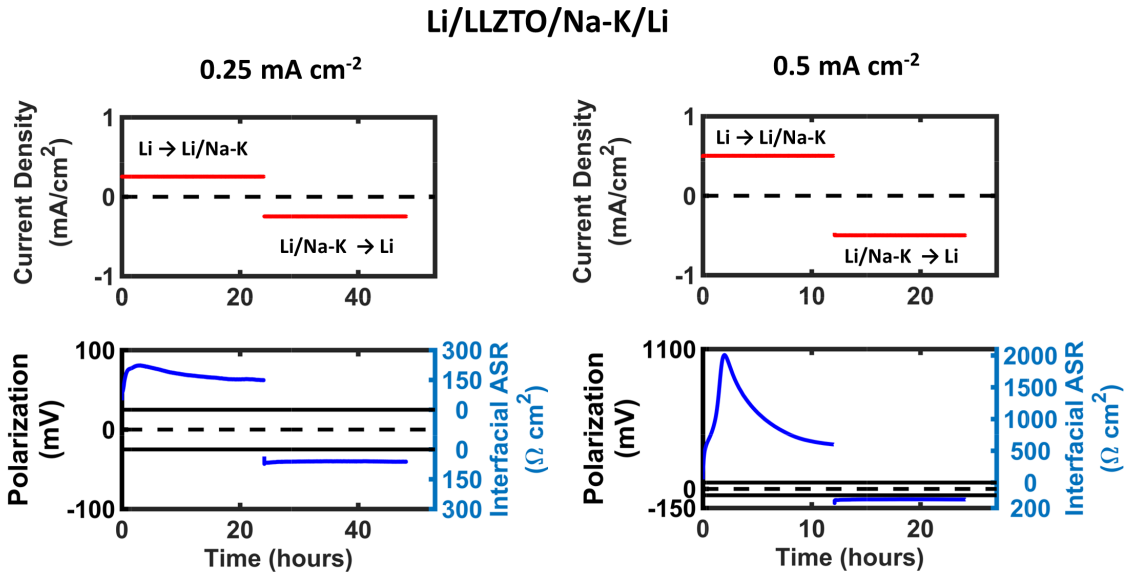

Figure 5-5: Polarization curves from Li/LLZTO/NaK/Li asymmetric cells in which Li is initially stripped from a plain Li interface and plated at a Li/Na-K interface. (left) Current and voltage time-traces for cells undergoing one full cycle (areal capacity of 6mAh cm^{-2}) at a current density of 0.25 mA cm^{-2}. (right) Analogous time-traces for an independant cell undergoing one full cycle (areal capacity of 6mAh cm^{-2}) at a current density of 0.5 mA cm^{-2}. In both cases positive current corresponds to stripping from the plain Li electrode and plating on the NaK-Li composite electrode. The stripping and plating electrodes are reversed upon the reversal of current. Note that the vertical axis scale is different in each subfigure. In each subplot, the interfacial ASR values provided are the total contribution from both interfaces within the cell. This value is obtained by subtracting the ASR due to the bulk electrolyte (100 Ω cm^2) from the total measured ASR. The cell polarization that corresponds to zero interfacial ASR in each current direction is indicated by the solid black bands. Rapid impedance rises are associated with stripping from a plain Li electrode.

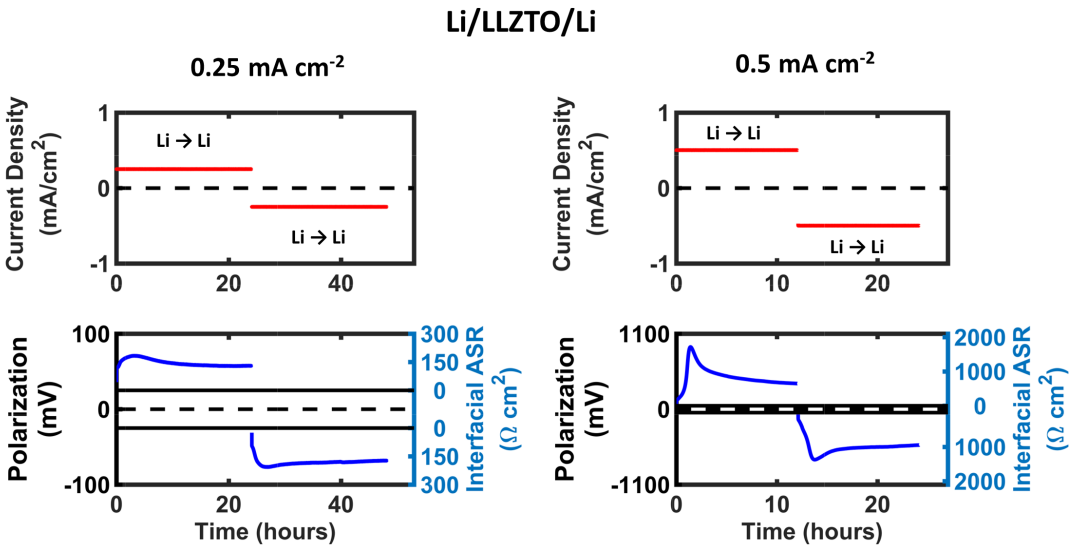

Figure 5-6: Polarization curves from Li/LLZTO/Li symmetric cells in which Li is stripped from a plain Li interface and plated at a Li interface. (left) Current and voltage time-traces for cells undergoing one full cycle (areal capacity of 6mAh cm^{-2}) at a current density of 0.25 mA cm^{-2}. (right) Analogous time-traces for an independant cell undergoing one full cycle (areal capacity of 6mAh cm^{-2}) at a current density of 0.5 mA cm^{-2}. Positive and negative current both correspond to stripping and plating from a plain Li electrode. Note that the vertical axis scale is different in each subfigure. In each subplot, the interfacial ASR values provided are the total contribution from both interfaces within the cell. This value is obtained by subtracting the ASR due to the bulk electrolyte (100 Ω cm^2) from the total measured ASR. The cell polarization that corresponds to zero interfacial ASR in each current direction is indicated by the solid black bands. Rapid impedance rises are associated with stripping from a plain Li electrode.

Chapter 6

Conclusions

The interface between an alkali metal and its respective solid electrolyte is of great interest as it remains a key bottleneck in the development of all-solid-state batteries that incorporate metallic electrodes. Such batteries may offer significant improvements over their Li-ion battery counterparts which adopt liquid electrolytes in terms of safety and energy density, thereby enabling further advances in portable electronics and electric vehicles. However, the mechanical instability of the metal-solid electrolyte interface during high-rate (> 3 mA cm^{-2}) electrodeposition represents a major challenge to the commercial viability of all-solid-state batteries. In the preceding chapters, we used various model solid electrolytes and alkali metal electrodes to study the mechanistic processes that cause this instability. Our findings inform rational design rules for high-performance metal-electrolyte interfaces within all-solid-state batteries.

In Chapter 2, we demonstrated that macroscopic current focusing due to nonuniform electric field profiles between electrodes determine the sites for metal penetration in solid electrolytes. This was shown in a single crystal model electrolyte in which grain boundaries are excluded as a path for metal propagataion. These results expanded upon previous work which showed, provided all else is equal, that metal penetration initiates at the largest surface flaws of the electrodeposited electrolyte. Our results showed that the macroscopic current focusing effect can override the presence of larger surface defects in proximity, illustrating the need for uniform electric field profiles between electrodes. We showed that this can be achieved by oversizing

the electrodeposition electrode relative to the source electrode.

In Chapter 3, we conducted a systematic study on the effects of electrodeposited metal yield stress on the critical current density at the metal electrolyte interface. By carefully choosing model solid electrolytes that exhibited similar ionic conductivities, fracture toughnesses, and surface finishes in the Li-Na-K system, we demonstrated that critical current densities scale inversely to mechanical deformation resistance. This demonstrates that the mechanical properties of the electrode can be engineered to facilitate stress relief at the metal-solid electrolyte interface, increasing the critical current density. These results advance the state-of-art in metal-solid electrolyte interface engineering, in which efforts are primarily devoted to tuning the properties of the electrolyte as opposed to the electrode. We apply this insight towards developing electrode architectures that suppress the onset of metal penetration at high electrodeposition current densities in the subsequent chapter.

In Chapter 4, we developed two novel electrode architectures in which the presence of a liquid phase enabled high current densities while preserving the shape retention and packaging advantage of solid electrodes. We first showed that biphasic liquid-solid alloys exhibit critical current densities an order of magnitude higher than those measured in all-solid electrodes, and that increasing the liquid fraction in the electrodeposition electrode raises the critical current density by increasing the ease at which stress at the interface can be relieved via electrode deformation. We then showed that the introduction of a electrochemically inert, wetting interfacial liquid film between a solid electrolyte and a solid electrode also raises the critical current density relative to solid electrodes via the homogenizing plating current.

In Chapter 5, we further explored the properties of a thin Na-K liquid interlayer at the interface between Li metal and LLZTO SSE. We demonstrated that composite electrodes incorporating an interfacial Na-K film permits cycling at much higher accessible areal capacities compared to solid electrodes. We then showed that the Na-K film enables these higher stripping areal capacities without the traditional need for large applied stack pressures and heat treatments to strip Li metal. These improvements were shown to be due to the interfacial film failicating intimate electrical

contact between the electrode and the SSE, whilst self-healing metal vacancies that form at the metal-solid electrolyte during electrostripping.

Hence, we have gained a number of insights into the process via which metals infiltrate solid electrolytes during electrodeposition. We established that the onset of metal penetration can be substantially mitigated via the tuning of electrodeposition electric field profiles, adjusting the mechanical properties of the electrodeposited metal, or appropriately incorporating a liquid phase into the solid electrode. Our findings consequently establish rational design rules for high-rate capability, high-capacity all solid state batteries incorporating metallic electrodes.

6.1 Future work

Nonuniformities in the electrodeposition current density identified in Chapter 2 prevented a systematic study of the relationship between surface flaw sizes, critical current densities, and critical overpotentials for metal penetration from being carried out. We expect that such relations can be accurately quantified via electrodeposition onto controlled surface defects on an appropriately sized electrode per our recommendations for homogenizing electrodeposition current.

The inverse scaling relation between the critical current density and the mechanical deformation resistance of the electrodeposited metal identified in Chapter 3 is further tenable to experimental evaluation. Analogous experiments using different metal-electrolyte pairs may yield additional insight into the global applicability of this trend. Suggested metal-electrolyte pairs include Ag-$RbAg_4I_5$ or Na-NASICON, provided that the electrolytes can be prepared to possess a similar fracture toughness, surface finish, and ionic conductivity.

The exact mechanism for the improved performance of electrodes incorporating an interfacial liquid film described in Chapter 4 relative to purely solid electrodes remains unclear. An experiment enabling direct *in-situ* observation during cycling of the plating and stripping interfaces with and without such films may be helpful. One possible experimental technique is X-ray tomography. For this technique we

suggest that alternative model solid electrolytes, such as Li^+ conducting argyrodites, are used in place of LLZTO. LLZTO is known to attenuate X-ray beams due to the high atomic number of its constituent elements, and may impede the acquisition of high-resolution data.

References

[1] P. Albertus, S. Babinec, S. Litzelman, and A. Newman. Status and challenges in enabling the lithium metal electrode for high-energy and low-cost rechargeable batteries. *Nat. Energy*, 3:16–21, 2018.

[2] B. McGinty. Stresses at elliptical holes [www.fracturemechanics.org], 2016.

[3] L. Porz et al. Mechanism of lithium metal penetration through inorganic solid electrolytes. *Adv. Energy Mater*, 7:1701003, 2017.

[4] G.R. Anstis, P. Chantikul, B.R. Lawn, and D.B. Marshall. A critical evaluation of indentation techniques for measuring fracture toughness: I, direct crack measurements. *J. Am. Ceram. Soc*, 64:533–538, 1981.

[5] A.G. Evans and E.A. Charles. Fracture toughness determinations by indentation. *J. Am. Ceram. Soc*, 59:371–372, 1976.

[6] J. Wolfenstine et al. A preliminary investigation of fracture toughness of $Li_7La_3Zr_2O_{12}$ and its comparison to other solid Li-ion conductors. *Mater. Lett*, 96:117–120, 2013.

[7] X. Lu, J.P. Lemmon, V. Sprenkle, and Z. Yang. Sodium-beta alumina batteries: Status and challenges. *JOM.*, 62:31–36, 2010.

[8] W.J. McDonough, D.R. Flinn, K.H. Stern, and R.W Rice. Hot pressing and physical properties of na beta alumina. *J. Mater. Sci.*, 13:145–150, 1978.

[9] D. Tabor. *The Hardness of Metals*. Oxford University Press, 2000.

[10] N.J. Taylor et al. Demonstration of high current densities and extended cycling in the garnet $Li_7La_3Zr_2O_{12}$ solid electrolyte. *J. Power Sources*, 396:314–318, 2018.

[11] A. Sharafi et al. Characterizing the Li-$Li_7La_3Zr_2O_{12}$ interface stability and kinetics as a function of temperature and current density. *J. Power Sources*, 302:135–139, 2016.

[12] E.J. Cheng, A. Sharafi, and J. Sakamoto. Intergranular Li metal propagation through polycrystalline $Li_{6.25}Al_{0.25}La_3Zr_2O_{12}$ ceramic electrolyte. *Electrochim. Acta*, 223:85, 2017.

[13] A. Sharafi et al. Surface chemistry mechanism of ultra-low interfacial resistance in the solid-state electrolyte $Li_7La_3Zr_2O_{12}$. *Chem. Mater*, 29:7961–7968, 2017.

[14] A. Sharafi et al. Impact of air exposure and surface chemistry on Li - $Li_7La_3Zr_2O_{12}$ interfacial resistance. *J. Mater. Chem. A*, 5:13475–13487, 2017.

[15] L. Cheng et al. Effect of surface microstructure on electrochemical performance of garnet solid electrolytes. *ACS Appl. Mater. Interfaces*, 7:2073–2081, 2015.

[16] R.H. Basappa, T. T. Ito, and H. Yamada. Contact between garnet-type solid electrolyte and lithium metal anode: influence on charge transfer resistance and short circuit prevention. *J. Electrochem. Soc.*, 164:A666–A671, 2017.

[17] R.H. Basappa et al. Grain boundary modification to suppress lithium penetration through garnet-type solid electrolyte. *J. Power Sources*, 363:145–152, 2017.

[18] D. Howell, B. Cunningham, T. Duong, and P. Faguy. Overview of DOE Vehicle Technologies Office Advanced Battery R&D program, 2016.

[19] J.E. Harlow et al. A wide range of testing results on an excellent lithium-ion cell chemistry to be used as benchmarks for new battery technologies. *J. Electrochem. Soc*, 166:3031–3044, 2019.

[20] R. Elder. Overview and progress of United States Advanced Battery Consortium activity, 2016.

[21] R. Huggins. *Advanced Batteries*. Springer US, 2009.

[22] A. Bard and L. Faulkner. *Electrochemical methods: Fundamentals and Applications*. Wiley, 2001.

[23] V. Etacheri et al. Challenges in the development of advanced Li-ion batteries: a review. *Energy Environ. Sci*, 4:3243, 2011.

[24] D. Aurbach, E. Zinigrad, Y. Cohen, and H. Teller. A short review of failure mechanisms of lithium metal and lithiated graphite anodes in liquid electrolyte solutions. *Solid State Ionics*, 148:405–416, 2002.

[25] Z. Liu et al. Interfacial study on solid electrolyte interphase at Li metal anode: implication for Li dendrite growth. *J. Electrochem. Soc*, 163:592–598, 2016.

[26] A. Manthiram, X. Yu, and S. Wang. Lithium battery chemistries enabled by solid-state electrolytes. *Nat. Rev. Mater*, 2:16103, 2017.

[27] K. Kerman, A. Luntz, V. Viswanathan, Y.-M. Chiang, and Z. Chen. Practical challenges hindering the development of solid state Li-ion batteries. *J. Electrochem. Soc*, 164:1731–1744, 2017.

[28] J. Janek and W.G. Zeier. A solid future for battery development. *Nat. Energy*, 1:16141, 2016.

[29] J. Li et al. Solid electrolyte: the key for high-voltage lithium batteries. *Adv. Energy Mater*, 5:1401408, 2015.

[30] W.D. Richards et al. Interface stability in solid-state batteries. *Chem. Mater*, 28:266, 2016.

[31] R. Balluffi, S.M. Allen, and W.C. Carter. *Kinetics of Materials*. Wiley, 2005.

[32] V. Thangadurai, S. Narayanan, and D. Pinzaru. Garnet-type solid-state fast Li ion conductors for Li batteries: critical review. *Chem. Soc. Rev*, 43:4714–4727, 2014.

[33] D. Liu et al. Recent progress in sulfide-based solid electrolytes for Li-ion batteries. *Mater. Sci. Eng. B*, 213:169–176, 2016.

[34] F. McGrogan et al. Compliant yet brittle mechanical behavior of Li_2S–P_2S_5 lithium-ion-conducting solid electrolyte. *Adv. Energy Mater*, 7:1602011, 2017.

[35] C. Monroe and J. Newman. The impact of elastic deformation on deposition kinetics at lithium/polymer interfaces. *J. Electrochem. Soc*, 152:396–404, 2005.

[36] F. Aguesse et al. Investigating the dendritic growth during full cell cycling of garnet electrolyte in direct contact with Li metal. *ACS Appl. Mater. Interfaces*, 9:3808–3816, 2017.

[37] Y.Y. Ren, Y. Shen, Y.H. Lin, and C.W. Nan. Direct observation of lithium dendrites inside garnet-type lithium-ion solid electrolyte. *Electrochem. Commun*, 57:27–30, 2015.

[38] M. Nagao et al. In situ sem study of a lithium deposition and dissolution mechanism in a bulk-type solid-state cell with a Li_2S–P_2S_5 solid electrolyte. *Phys. Chem. Chem. Phys*, 15:18600–18606, 2013.

[39] A.A. Griffith. The phenomena of rupture and flow in solids. *Soc*, 221A:163–198, 1920.

[40] N. Muskhelishvili. *Some basic problems of the mathematical theory of elasticity*. Noordhoff Ltd, 1953.

[41] E. Kirsch. Die theorie der elastizitat und die bedurfnisse der festigkeitslehre. *Zeitschrift des Vereines Dtsch. Ingenieure*, 42:797, 1898.

[42] C.E. Inglis. Stresses in a plate due to the presence of cracks and sharp notches. *Inst. Naval Architects*, 55:219–241, 1913.

[43] H. Westergaard. Bearing pressures and cracks. *J. Appl. Mech*, 6:49–53, 1939.

[44] G. Irwin. Analysis of stresses and strains near the end of a crack transversing a plate. *J. Appl. Mech*, 24:361, 1957.

[45] R. Armstrong, T. Dickinson, and J. Turner. The breakdown of β–alumina electrolyte. *Electrochim. Acta*, 19:187, 1974.

[46] R.H. Richman and G.J. Tennenhouse. A model for degradation of ceramic electrolytes in Na-S batteries. *J. Am. Ceram. Soc*, 58:63–67, 1975.

[47] M.P.J. Brennan. The failure of β–alumina electrolyte by a dendritic penetration mechanism. *Electrochim. Acta*, 25:621–627, 1980.

[48] A.V. Virkar and L. Viswanathan. Sodium penetration in rapid ion conductors. *J. Am. Ceram. Soc*, 62:528–529, 1979.

[49] A.V. Virkar, L. Viswanathan, and D.R. Biswas. On the deterioration of β"–alumina ceramics under electrolytic conditions. *J. Mater. Sci*, 15:302, 1980.

[50] A.V. Virkar. On some aspects of breakdown of β"–alumina solid electrolyte. *J. Mater. Sci*, 16:1142–1150, 1981.

[51] A.V. Virkar. The role of superimposed stresses on the degradation of solid electrolytes. *J. Mater. Sci*, 21:859, 1986.

[52] E. Rangasamy, J. Wolfenstine, and J. Sakamoto. The role of Al and Li concentration on the formation of cubic garnet solid electrolyte of nominal composition $Li_7La_3Zr_2O_{12}$. *Solid State Ionics*, 206:28–32, 2012.

[53] T. Swamy et al. Lithium metal penetration induced by electrodeposition through solid electrolytes: Example in single-crystal $Li_6La_3Zr_2TaO_{12}$ garnet. *J. Electrochem. Soc*, 165:3648–3655, 2018.

[54] C. Xu, Z. Ahmad, A. Aryanfar, V. Viswanathan, and J.R. Greer. Enhanced strength and temperature dependence of mechanical properties of Li at small scales and its implications for Li metal anodes. *Proc. Natl. Acad. Sci. USA*, 114:57–61, 2017.

[55] A.V. Virkar and R.S. Gordon. Fracture properties of polycrystalline lithia-stabilized β"–alumina. *J. Am. Ceram. Soc*, 60:58, 1977.

[56] A.V. Virkar and L. Viswanathan. A three-dimensional approach to the electrolytic degradation of solid electrolytes. *J. Mater. Sci*, 18:1202, 1983.

[57] A.V. Virkar. A model for internal pressurization in cationic solid electrolytes. *J. Mater. Sci*, 20:552–562, 1985.

[58] K. Simon et al. Low-profile self-sealing sample transfer flexure box. *Rev. Sci. Instrum*, 88:083705, 2017.

[59] K. Yan et al. Selective deposition and stable encapsulation of lithium through heterogeneous seeded growth. *Nat. Energy*, 1:16010, 2016.

[60] Y. Zhu, X. He, and Y. Mo. First principles study on electrochemical and chemical stability of solid electrolyte–electrode interfaces in all-solid-state Li-ion batteries. *J. Mater. Chem. A*, 4:3253, 2016.

[61] B. Stanje et al. Solid electrolytes: Extremely fast charge carriers in garnet-type $Li_6La_3ZrTaO_{12}$ single crystals. *Ann. Phys*, 529:1700140, 2017.

[62] R. Brook. *Concise Encyclopedia of Advanced Ceramic Materials*. Pergamon Press, 1991.

[63] V. Fleury, W.A. Watters, L. Allam, and T. Devers. Rapid electroplating of insulators. *Nature*, 416:716, 2002.

[64] S.W. Kim, Y.J. Ahn, and W.Y. Yoon. The surface morphology of Li metal electrode. *Met. Mater*, 6:345, 2000.

[65] R.J.-Y. Park et al. Semi-solid alkali metal electrodes enabling high critical current densities in solid electrolyte batteries. *Nat. Energy*, 6:314–322, 2021.

[66] E. Orowan. Fracture and strength of solids. *Rep. Prog. Phys*, 12:185–232, 1949.

[67] C.D. Fincher et al. Mechanical properties of metallic lithium: from nano to bulk scales. *Acta Mater*, 186:215–222, 2019.

[68] W.S. LePage et al. Lithium mechanics: roles of strain rate and temperature and implications for lithium metal batteries. *J. Electrochem. Soc*, 166:89–97, 2019.

[69] V.G. Vaks, S.P. Kravchuk, E.V. Zarochentsev, and V.P. Safronov. Temperature dependence of the elastic constants in alkali metals. *J. Phys. F Met. Phys*, 8:725–742, 1978.

[70] D. Hull and H.M. Rosenberg. The deformation of lithium, sodium and potassium at low temperatures: Tensile and resistivity experiments. *Philos. Mag*, 4:303–315, 1959.

[71] E.N. da C. Andrade and E.R. Dobbs. The viscosities of liquid lithium, rubidium and caesium. *Proc. R. Soc. Lond. A*, 211:12–30, 1952.

[72] A.V. Grosse. Viscosities of liquid sodium and potassium, from their melting points to their critical points. *Science*, 147:1438–1411, 1965.

[73] P.M. Sargent and M.F. Ashby. Deformation mechanism maps for alkali metals. *Scr. Metall.*, 18:145–150, 1984.

[74] C.D. Fincher, Y. Zhang, G.M. Pharr, and M. Pharr. Elastic and plastic characteristics of sodium metal. *ACS Appl. Energy Mater*, 3:1759–1767, 2020.

[75] D.S. Jolly et al. Sodium/Na β"- alumina interface: Effect of pressure on voids. *ACS Appl. Mater. Interfaces*, 12:678–685, 2020.

[76] M.-C. Bay et al. Sodium plating from Na-β"-alumina ceramics at room temperature, paving the way for fast-charging all-solid-state batteries. *Adv. Energy Mater*, 10:1902899, 2019.

[77] J.B. Bates et al. Thin-film lithium and lithium-ion batteries. *Solid State Ion*, 135:33–45, 2000.

[78] J. Kasemchainan et al. Critical stripping current leads to dendrite formation on plating in lithium anode solid electrolyte cells. *Nat. Mater*, 18:1105–1111, 2019.

[79] A.C. Baclig et al. High-voltage, room-temperature liquid metal flow battery enabled by Na-K|K- β"-alumina stability. *Joule*, 2:1287–1296, 2018.

[80] C. Liu, J.S. Shamie, L.L. Shaw, and V.L. Sprenkle. An ambient temperature molten sodium–vanadium battery with aqueous flowing catholyte. *ACS Appl. Mater. Interfaces*, 8:1545–1552, 2015.

[81] X. Guo et al. A self-healing room-temperature liquid-metal anode for alkali-ion batteries. *Adv. Funct. Mater*, 28:1804649, 2018.

[82] L. Kaufman. The lattice stability of metals—I. titanium and zirconium. *Acta Metall*, 7:575–587, 1959.

[83] A.T. Dinsdale. SGTE data for pure elements. *Calphad*, 15:317–425, 1991.

[84] O. Redlich and S.T. Kister. Algebraic representation of thermodynamic properties and the classification of solutions. *Ind. Eng. Chem*, 20:345–348, 1948.

[85] H. Lukas, S.G. Fries, and Sundman B. *Computational Thermodynamics: The CALPHAD Method*. Cambridge University Press, 2007.

[86] S.J. Zhang. *Thermodynamic Investigation of the Effect of Alkali Metal Impurities on the Processing of Al and Mg Alloys*. Ph.D thesis, Pennsylvania State University, 2006.

[87] M.J. Wang, R. Choudhury, and J. Sakamoto. Characterizing the li-solid-electrolyte interface dynamics as a function of stack pressure and current density. *Joule*, 3:2165–2178, 2019.